Proceedings, 6th Chaotic Modeling and Simulation International Conference
11 - 14 June 2013 Istanbul, Turkey

Hysteresis modelling of cold-formed steel shear walls with neural networks

Abdollahzadeh G. R., Ghobadi F.

Department of Civil Engineering, Babol University of technology, Babol, Iran
E-mail: Abdollahzadeh@nit.ac.ir
Department of Civil Engineering, Shomal University, Amol, Iran
E-mail: faridghobadi@yahoo.com

Abstract: In this paper is tried to recognize the pattern of hysteresis behavior of cold-formed steel shear walls with using neural networks. Recognizing and investigating of the hysteresis behavior of structural elements is one of the best methods for economical and safe design of structures. In this way, in addition to the observation of the behavior of elements especially in cyclic loading, useful information like: dissipated energy, maximum load and maximum displacement can be obtained. If the hysteresis behavior can be modeled, then the aforementioned information will be obtained from the simulated model and this model can be used for different loading pattern. In this study, with defining proper input variables, defining the number of hidden layers in neural network model and using the experimental results, is tried to make a model that contains the characteristics of the parameters that are important in hysteresis behavior.
Keywords: hysteresis modeling, neural networks, pattern recognition, shear walls.

1. Introduction

Neural networks are appropriate alternative for primitive methods in the case of modeling materials and structures with complex behavior. This alternative method is based on the information that obtained from experimental results. Computational intelligence methods like neural networks make this modeling approach possible. The information that is needed for training network obtain from experimental data and store in neural networks, then the trained neural network can be used for simulating.

For training the neural network in this article, the information obtained from experimental data that was available for a cold-formed steel shear wall is used. The experiment has been conducted in north texas university in 2012**.** The most common seismic lateral force resisting system for light steel framing is wood sheathed, cold-formed steel framed, shear walls. A wide body of testing has been conducted on these walls as embodied in the AISI-S213-07 standard. The shear walls designed for a two-story ledger-framed building that will undergo full-scale shake table test. In order to explore the expected performance-basis of shear walls in the CFS-NEES building tests were conducted to understand the impact of practical details and to provide the necessary information for subsequent hysteretic characterization of the shear walls. The experimental information is used to train the neural network**.** The hysteretic behavior contains a lot of information like: initial stiffness, the amount of strength and stiffness degradation and the amount of energy dissipated in the system. So, modeling this behavior with new methods like neural networks can be valuable. In the proposed neural network model, with defining proper input variables and training the network, the hysteresis curve with considering the effects of degradation in stiffness is predicted.

In mathematical models because of some simplified assumptions, the real hysteresis curve is different from the simulated one. In this paper with defining the hysteresis parameters is tried to train the neural network, then with using trial and error method and with changing the internal parameters of network the hysteresis curve can be drawn. At last the outputs of network will be compared with experimental data and the importance of each variable will be determined.

2. outline of test

cyclic tests were performed on a 4ft wide and 9ft high adaptable structural steel testing frame. Figure 1 depicts the test frame. Shear walls were bolted to a steel base beam.

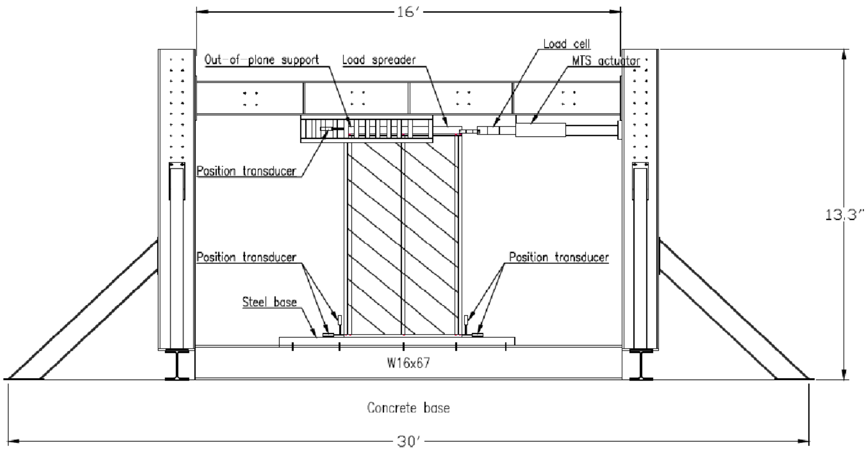

(a)

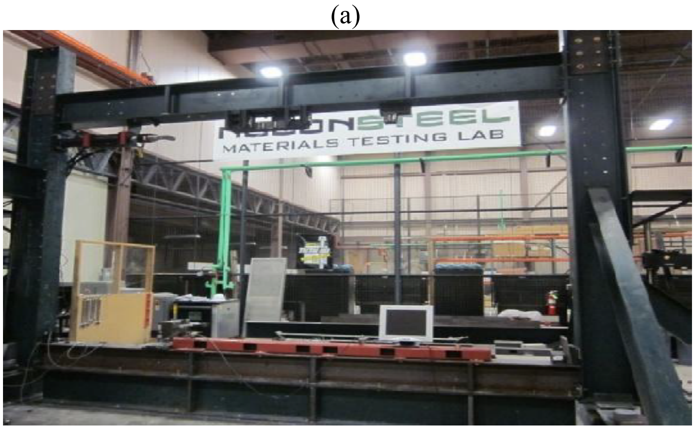

(b)

Fig. 1. Shear wall test set up (a) schematic of testing rig with specimen, (b) test frame[1]

The CUREE protocol was chosen for the cyclic tests[2]. The CUREE basic loading history is shown in the Figure 2. It includes 43 cycles with displacement amplitudes that are based on a percentage of ultimate displacement from the monotonic test. The CUREE protocol is in accordance with the test method CASTM E2126(2007).

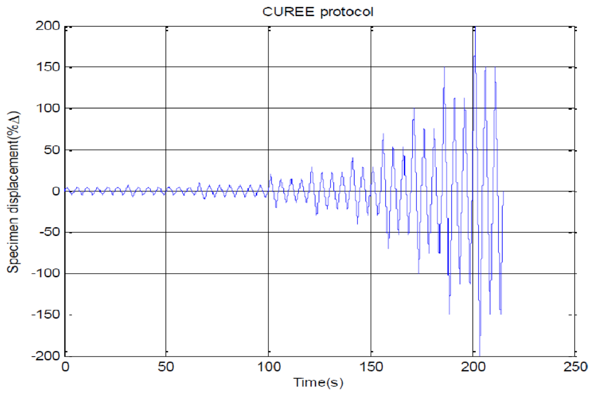

Fig.2 CUREE loading history[1]

3. Result of test

Table 1 shows the characteristics of the experimental specimen.

Table 1.charactrristic of the shear wall

Wall dimensions	4 ft × 9ft	Temperature	77F
Loading type	Cyclic	Humidity	43%
Front sheathing	OSB	Maximum +load	5060lbf
OSB Thickness	7/16’’	Maximum -load	-3830lbf
Back sheathing	Gypsum board	Lateral displacement	-2.435 in
Fastener spacing	12in	Average displacement	2.653in

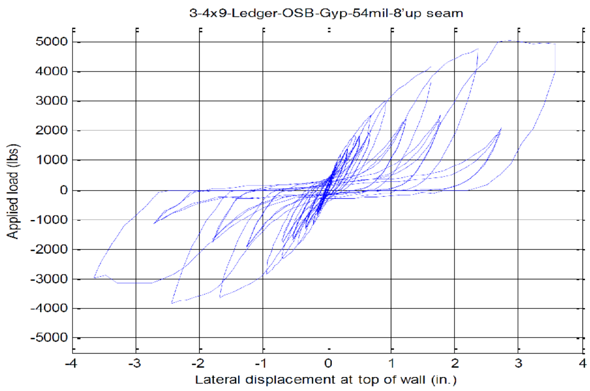

Fig.3 hysteresis behavior of the shear wall[1]

Fig.3 shows the hysteresis behavior of the shear wall that is obtained from experimental results. In the next step this hysteresis behavior is simulated with neural networks. Different views of shear wall are shown in fig.4.

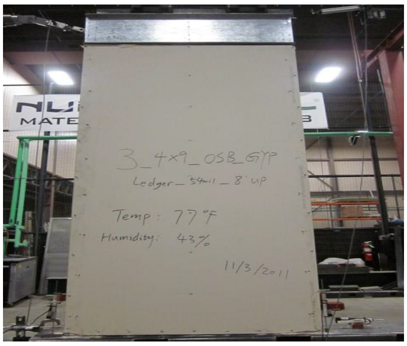

Back side[1]

Front side[1]

Gypsum board [1]

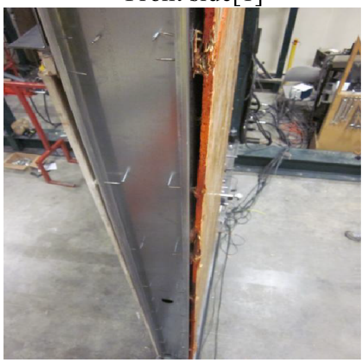

OSB failure[1]

Fig.4 Different views of shear wall

4 Neural network model

In this part the information obtained from load-displacement curve is used for estimating the hysteresis curve. At the present, Feed-Forward neural networks are widely used in the field of engineering. These neural networks are usually constructed with multiple layers of artificial neurons: an input layer, output layer, and hidden layers. In neural network architecture, the number of neurons in the input and output layers are determined by the formulation of the problem. The number of neurons in the input and output layers is related to the capacity of the neural network. The neural network requires sufficient capacity to represent the complexity of the underlying information in the training data. However, the degree of complexity of the problem cannot easily be quantified [3].

Back-propagation is a learning algorithm in Feed Forward networks. The back-propagation algorithm is a method of changing the connection weights so that the Feed-Forward network learns the input-output pairs in the training set. The learning

rule is based on the gradient descent algorithm, which suggest changing each weight proportional to the gradient of cost function (error measure) at the present location. It necessarily decrease the error (or cost function) if the learning rate is small enough. In order to represent the behavior of the path dependency, multi-point models which employ additional input variables such as immediate previous states of variables or variables increments should be used.
It was mentioned earlier that the relationship between the neurons in the hidden layers, the capacity of the neural network, and the degree of complexity in a given problem cannot be easily quantified. The adaptive technique allows the new neurons to be automatically added to hidden layers during the training, which is shown schematically in fig.7.

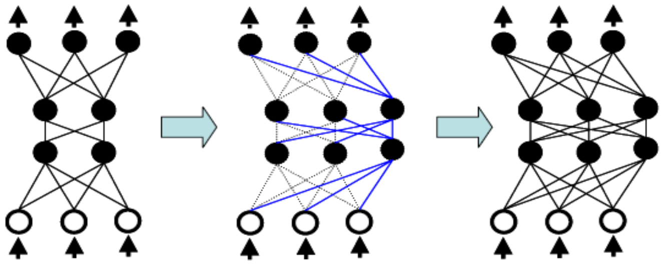

Fig.7. Adaptive feature[4]

4-1 Nonlinear hysteretic model

Even if great advances have been made in the inelastic modeling of materials and structural components, nonlinear analysis remains challenging [5,6] , especially in the case of cyclic or dynamic loading. Classical plasticity models combine properties of isotropic and kinematic plasticity to explain the cyclic or dynamic behavior[7-9]. However, those hardening rules have some difficulties in illustrating the bauchinger effect in materials and hysteretic degradation in structural components. In a typical cyclic response, one strain value is corresponding to multiple stress, and vice versa. This is referred to as one-to-many mapping[10]. The one-to-many mapping prevents the neural network from learning hysteretic behaviors. Introducing new additional variables in the input layer allow the neural network to create and learn a unique mapping between stresses and strains. Fig.8. shows a neural network hysteretic model developed by Yun et al.(2006) [11].

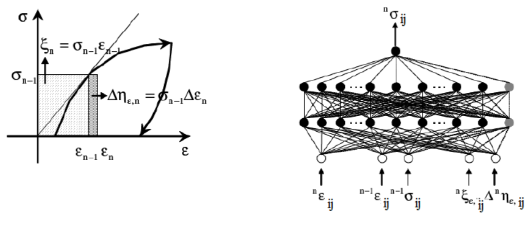

(a) Internal variables (b) Neural network structure

Fig.8. Neural network based cyclic model by Yun (2006) [11]

The proposed neural network model contain 5 input variables of ε_{n-1} ,σ_{n-1},ζ_n , ε_n and $\Delta\eta_n$ in strain control form. Two hysteretic parameters of ζ_n and $\Delta\eta_n$ were introduced to transform the one-to-many mapping to single valued mapping[12]. These were defined as $\zeta_n = \sigma_{n-1}\ \varepsilon_{n-1}$ and $\Delta\eta_n = \sigma_{n-1}\ \Delta\varepsilon_n$, where the subscript n indicates the n-th incremental step. The variable ζ relates to strain energy in the previous step along the equilibrium path. The variable $\Delta\eta$ indicates the direction for the next step along the equilibrium path[11].

4-2 Neural network for hysteretic behavior of shear walls

In this section, the neural network for modeling the cyclic behavior of shear wall is made. The neural network is defined in the load and displacement domain instead of the stress and strain domain, as can be seen in equation 1.

$$\mathbf{F_n = F_{NN}[\{D_n, D_{n-1}, F_{n-1}, \zeta_n, \Delta\eta_n, E_{n-1}\}]} \qquad \textbf{(1)}$$

Two hysteretic parameters are defined as $\zeta_n = F_{n-1}\ D_{n-1}$ and $\Delta\eta_n = F_{n-1}\ \Delta D_n$, where the subscript n indicates the n-th incremental step. These hysteretic parameters are key variables for unique mapping by determining the quadrant and path direction. Each path corresponds to the unique combination of the signs of the three variables $\Delta\eta_n$,ζ_n and D_n as can be seen in fig.9. In order to represent the degradation of stiffness and strength in consecutive cycles, a degradation parameter is introduced as an input variable and defined as $E_{n-1} = E_{n-2} + |F_{n-1}\ D_{n-1}|$. The degradation parameter indicates the accumulated strain energy until the previous step. The combination of current rotation and the degradation parameter provides the neural network with information about the level of fatigue and relaxation. For example, input variables including a large value degradation parameter predicts less load than when input variables contain a smaller value degradation parameter. Fig.10. illustrates the unique mapping with degradation. The trained neural network models should be verified with the target response in recurrent mode. In the recurrent mode, the output predicted by the trained neural network models is utilized in computing the input values in the next step, as can be seen in fig.11. Therefore, the inputs in the current step such as the hysteretic parameters and previous states of forces and displacement are determined with the output of the neural network in the previous step. This mode suits for nonlinear analysis techniques.

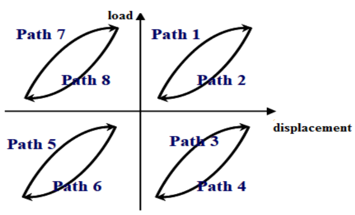

	ξ	$\Delta\eta$	D
Path 1	+	+	+
Path 2	+	-	+
Path 3	-	+	+
Path 4	-	-	+
Path 5	+	+	-
Path 6	+	-	-
Path 7	-	+	-
Path 8	-	-	-

Fig.9. unique mapping by hysteretic parameters and current rotation

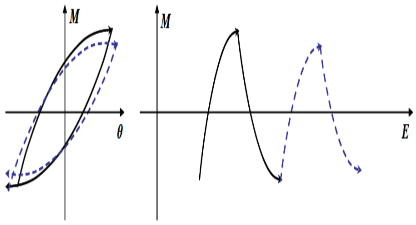

Fig.10. mapping with degradation

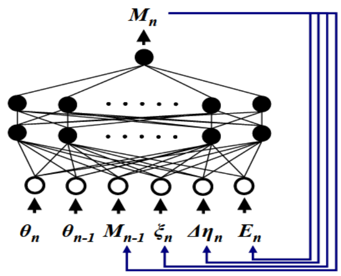

Fig.11. network in recurrent mode[13]

The experimental results in fig.3 exhibit a highly nonlinear response including pinching effects and light deterioration. These complicated phenomena are difficult to express with mathematical equations. From the experimental results, training data sets were collected and constructed with moment and rotation pairs digitized at random intervals.

$$\mathbf{F_n=F_{nn}[\{D_n,\ D_{n-1},\ F_{n-1},\zeta_n,\Delta\eta_n,E_{n-1}\}:\{6\text{-}15\text{-}15\text{-}1\}]} \qquad \textbf{(2)}$$

As seen in equation (2) for modeling the hysteresis behavior,6 input variable is used. this network contain 2 hidden layers and 15 neurons per hidden layer. After training the network with 12000 epochs, neural network model is tested in recurrent mode. As can be seen in fig.12. with using the outputs of the network the hysteresis curve can be drawn. The comparison between two curves shows that this neural network with defined variables can estimate the hysteresis behavior very well. So, the neural network with 6 input variable can be a good substitute for modeling this problem instead of complicating models. In summary, it can be said that this example shows, with using a neural network with proper design the hysteresis curve can be drawn with good accuracy. The importance and effect of each variable is shown in fig.13. As can be seen from fig.12. the effects of degradation parameter is clear. As can be seen from fig.13., it can be said that the importance of lateral load in the previous step is high and the importance of E is low in predicting the outputs of the network.

5 conclusion

In this study, the modeling of hysteresis behavior of shear wall is described. The proposed model is based on the information obtained from experiment and unlike the component method, that is not dependent on the mechanical characteristics and mathematical equations. As formerly mentioned with defining degradation parameters in input variables, the effects of degradation in stiffness and strength was seen in hysteresis curve. Considering aforementioned parameters in mathematical model is so complex. In this study with fitting a curve to outputs of the network the hysteresis curve is drawn . it can be seen that the curve is in a better situation than mathematical model. One of the defect of the neural network is that there is no perception toward the internal components and only the general behavior of the connection can be seen. the proposal for future studies of the author is that if this neural network model can be combined with component method and the effects of degradation in stiffness and strength can be considered in the model then the model will be shown the real behavior of the shear wall and the performance can be seen in the model.

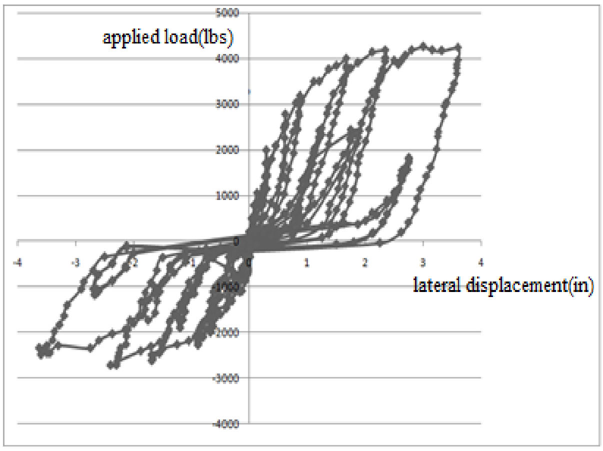

Fig.12. The hysteresis curve (the outputs of network)

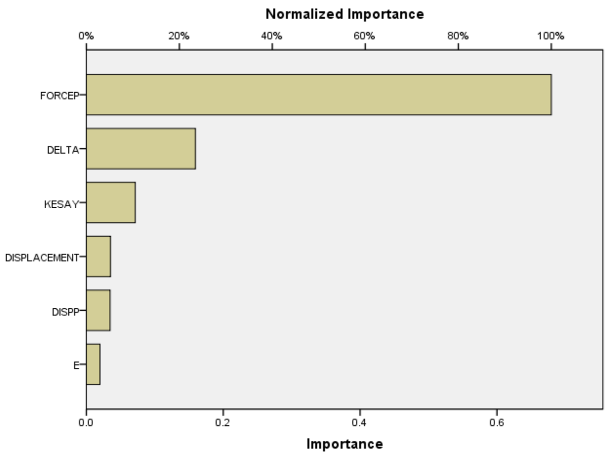

fig.13. The importance of each variable in predicting the outputs

References

1. P. Liu, K.D. Peterman and B.W. Schafer. Test Report on Cold-Formed Steel Shear Walls. Research Report, advancing cold-formed steel earthquake engineering, 2012.
2. ASTM E2126. Standard Test Methods for Cyclic Load Test for Shear

Resistance of Vertical Elements of the Lateral Force Resisting Systems for Buildings, 2011.
3. G. Yun, J. Ghaboussi and A. S. Enashai. A new neural network-based model for hysteretic behavior of materials. International Journal for Numerical Methods in Engineering 73(4):447- 469, 2008.

4. G. Yun, J. Ghaboussi and A. S. Enashai. Hybrid mathematical-informational modelling of beam-to-column connections, Report no.10-02, Mid-America Earthquake Center, 2010.

5. G. Yun, J. Ghaboussi and A. S. Enashai. A design-variable-based inelastic hysteric model for beam-column connections. Earthquake Engineering and Structural Dynamics 37: 535- 555, 2008.

6. JA Swanson and RT Leon. Bolted steel connections: Tests on T-stub components, J Struct Eng 126(1):50_60, 2000.

7. J. Ghaboussi, JH. Garrett and X. Wu. Knowledge-based modeling of material behavior with neural networks. J Eng Mech 117(1):32_53, 1991.

8. D. Gawin, M. Lefik and Schrefler BA. ANN approach to sorption hysteresis within a coupled hydro-thermo-mechanical FE analysis. Internat J Numer Methods Eng 50(2):299_323, 2001.

9. T. Furukawa and M. Hoffman. Accurate cyclic plastic analysis using a neural network material model. Eng Anal Bound Elem 28(3): 195_204, 2004.

10. G. W. Willis, c. Yao, R. Zhao and D. Penumadu. Stress-strain modeling of sands using artificial neural networks. Journal of Geotechnical Engineering – ASCE 121(5):429-435,1995.

11. J. Ghaboussi and D. E. Sidarta. New nested adaptive neural networks(NANN) for constitutive modeling. Computers and Geotechnics 22(1): 29-52,1998.

12. J. H. Kim, J. Ghaboussi and A.S. Elnashai. Mechanical and informational modeling of steel beam-to –column connections. Engineering Strucyures 32(2):449-458, 2010.

Layer-Recurrent Neural Network Modelling of Reactive Distillation Process

Abdulwahab GIWA[1] and Saidat Olanipekun GIWA[2]

[1]Middle East Technical University, Ankara, Turkey
[2]Ankara University, Ankara, Turkey
E-mails: agiwa@metu.edu.tr and giwa@ankara.edu.tr

Abstract: Reactive distillation is one of the complex processes encountered in process industries as a result of the integration of both reaction and separation in a single unit. Nowadays, the modelling of this process has become a big challenge to Process Engineers. The use of a reliable model that can handle complex functions is very necessary to represent this complex process. It has been discovered that Neural Network can be used to handle complex functions very well. Therefore, the modelling of the reactive distillation process considered in this work has been carried out with the aid of a dynamic neural network known as Layer-Recurrent Neural Network. The simulated results obtained from the developed Neural Network models were compared with the measured results to confirm the validities of the developed models.

Keywords: Neural Network, Reactive distillation, Modelling, Simulation.

1. Introduction

In recent years, integrated reactive separation processes have attracted considerable attentions in both academic research and industrial applications (Völker et al., 2007; Giwa and Karacan, 2012a). One of these processes which is known as reactive distillation is potentially attractive whenever conversion is limited by reaction equilibrium (Balasubramhanya and Doyle III, 2000; Giwa and Karacan, 2012a).

Reactive Distillation (RD) combines the benefits of equilibrium reaction with a traditional unit operation (in this case, distillation) to achieve a substantial progress in not only promoting the reaction conversion through constant recycling of unconverted materials and removal of products but also reducing the capital and operating costs in one way by reducing the number of equipment units (Giwa and Karacan, 2012a). Moreover, its other advantages include improved selectivity, lower energy consumption, scope for difficult separations and avoidance of azeotropes (Jana and Adari, 2009). However, due to the integration of reaction and separation, reactive distillation exhibits complex behaviours (Khaledi and Young, 2005) such as steady state multiplicity, process gain sign changes (bidirectionality) and strong interactions between process variables (Jana and Adari, 2009). These complexities have made the modelling of Reactive Distillation Process extremely difficult (Giwa and Karacan, 2012b; Giwa and Giwa, 2012). As such, a robust tool that can handle complex functions very well is needed to represent this complex process. One of these tools has been discovered to be Neural Network model because, according to Beale et al. (2010), Neural Network can be trained to handle complex functions.

Neural Network model can be viewed as a nonlinear empirical model that is especially useful in representing input-output data, in making predictions in time, and in classifying data (Himmelblau, 2000). Neural Network can be highly nonlinear, can learn easily, requires little or no a priori knowledge of model structure, is fault-tolerant and can handle complex problems that cannot be satisfactorily handled by the traditional methods (MacMurray and Himmelblau, 2000). There are many kinds of Neural Network models available in the literature. For instance, a simple classification can be: Static Neural Network and Dynamic Neural Network. It is perceived that a dynamic network, especially Layer-Recurrent Network (LRN), will be better in representing this complex Reactive Distillation Process because of the presence of a delay ensuring proper dynamics in each of its layers except in the last one.

According to the information gathered from the literature, Giwa and Karacan (2012a) used three different types of delayed neural network (Nonlinear AutoRegressive (NAR), Nonlinear AutoRegressive with eXogenous inputs (NARX) and Nonlinear Input-Output (IO)) models to represent a reactive distillation column in predicting the temperatures of the top and the bottom sections of the reactive distillation column used for the production of ethyl acetate and they were able to obtain very good results from both NAR and NARX models while the results given by IO models were found not to be satisfactory. Also, Giwa and Karacan (2012c) developed two nonlinear black-box (treepartition and sigmoid network NARX) models for the Reactive Distillation Process used for the production of ethyl acetate from the esterification reaction between acetic acid and ethanol and found that sigmoid network NARX model was better than treepartition NARX model for the reactive distillation process studied in their work.

In this work, Reactive Distillation Process is aimed to be modelled with the aid of Layer-Recurrent Neural Network using the metathesis reaction of trans-2-pentene to trans-2-butene and trans-2-hexene as the case study.

2. Procedures

The methods used for the accomplishment of this work are as outlined below.

2.1 Data Acquisition

The diagram of the metathesis reactive distillation column, developed with the aid of Aspen HYSYS (Aspen, 2011), used for the production of trans-2-butene (obtained in high purity at the top segment of the column) and trans-2-hexene (obtained in high purity at the bottom segment of the column) from trans-2-pentene, and from which the measured data used for the neural network model development were generated is as shown in Figure 1 below. As can be seen from the figure, the column had one feed stream and two product streams. The olefin metathesis reaction that occurred in the column was a reversible type given as shown in Equation 1.

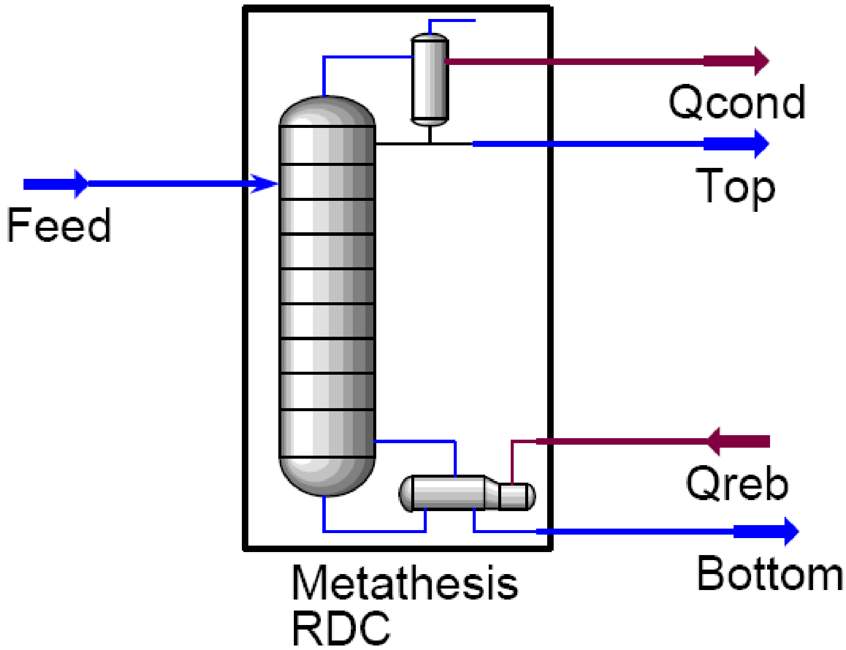

Fig. 1. Process flowsheet for metathesis reactive distillation process

$$2C_5H_{10} \xleftrightarrow{K_{eq}} C_4H_8 + C_6H_{12} \tag{1}$$

The data used for the development of the process in Aspen HYSYS environment are as given in Table 1.

Table 1. HYSYS metathesis reactive distillation process development data

Parameter	**Value**
Feed	
Flow rate (mL/min)	35
Temperature (K)	298.15
Pressure (atm)	1.11
Feed Composition (Mole fraction)	
trans-2-pentene	0.999998
trans-2-butene	1.00E-06
trans-2-hexene	1.00E-06
Fluid Package	UNIQUAC

Column	
Type	Packed
Packing type	Raschig Rings (Ceramic) 0.25 inch
No. of segment	15
Feed segment	8
Reaction	
Type	Equilibrium
Segment	6 - 10 and reboiler
K_{eq} source	Gibbs Free Energy
Basis	Molar concentration
Phase	Liquid

In the process development, reflux ratio and reboiler duty were chosen as the manipulated (input) variables while top segment and bottom segment temperatures were selected as the process (output) variables. By using the random data set values of the manipulated variables built with the aid of Parametric Utility of Aspen HYSYS, the column was run and the top segment and the bottom segment temperatures were obtained as the measured values of the output variables. Two different data sets were generated from the Aspen HYSYS system of the process. One was used for the training while the other was used for the testing of the Layer-Recurrent Neural Network models.

2.2 Modelling and Simulation

In the modelling of the Reactive Distillation Process in MATLAB (Mathworks, 2012) environment, the data sets obtained from Aspen HYSYS system of the process were converted from concurrent types to sequential ones because those were the types required by the dynamic Layer-Recurrent Neural Network. The parameters used for the formulation of the Neural Network models of the process considered in this work are as given in Table 2.

Table 2. Layer-Recurrent Neural Network model formulation parameters

Parameter	**Value**
Number of inputs	2
Number of outputs	2
Number of layers	2
Number of neurons in hidden layer	7
Hidden layer transfer function	*tansig*
Output layer transfer function	*purelin*
Training algorithm	Levenberg-Marquardt

Owing to the fact that there were two outputs, and even with two inputs, the structure of the neural network had two models in it – one for each process variable. The structure of the developed models is shown in Figure 2.

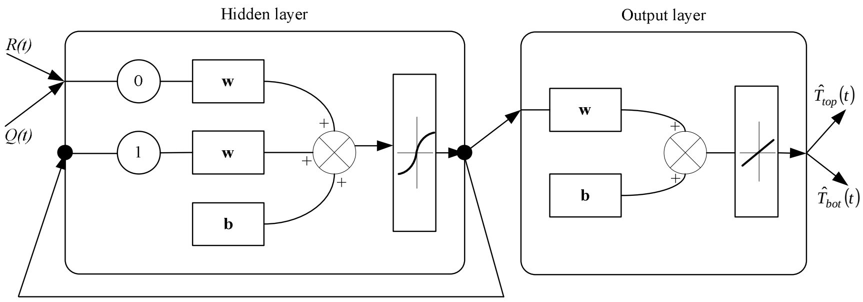

Fig. 2. Layer-Recurrent Neural Network of metathesis RD process

In determining the performances of the developed models, fit values (indicating the percentage of the data accounted for by the developed models), means of absolute errors and sums of squared errors were used as the criteria.

3. Results and Discussions

The acquired measured data sets of the input and the output variables used for the training and the testing the neural network models are given in Figures 3 and 4 respectively for the top segment and the bottom segment temperatures.

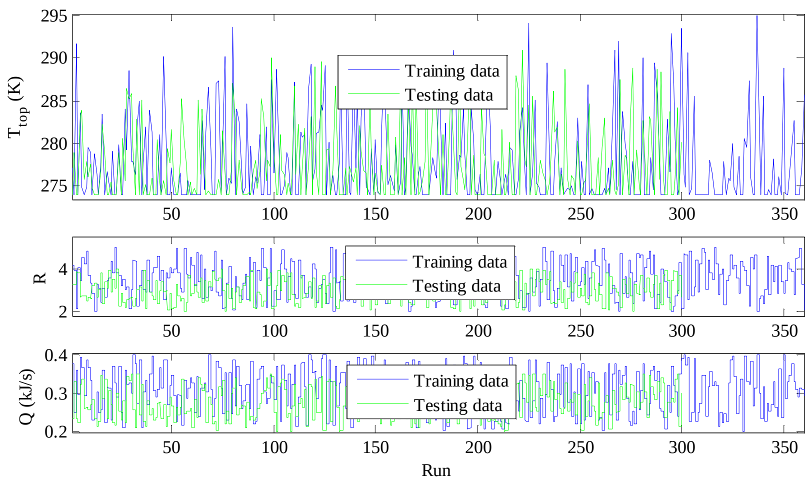

Fig. 3. Top segment temperature training and testing data sets

As can be seen from Figures 3 and 4, there were corresponding changes in the responses of the two segment temperatures as a result of the changes in the input variables. Also noticed from the results shown in Figures 3 and 4 was that the lengths of the training and the testing data for both segment temperatures were not the same but the overall limits of the testing manipulated variables used were within the ones used for the generation of the training data.

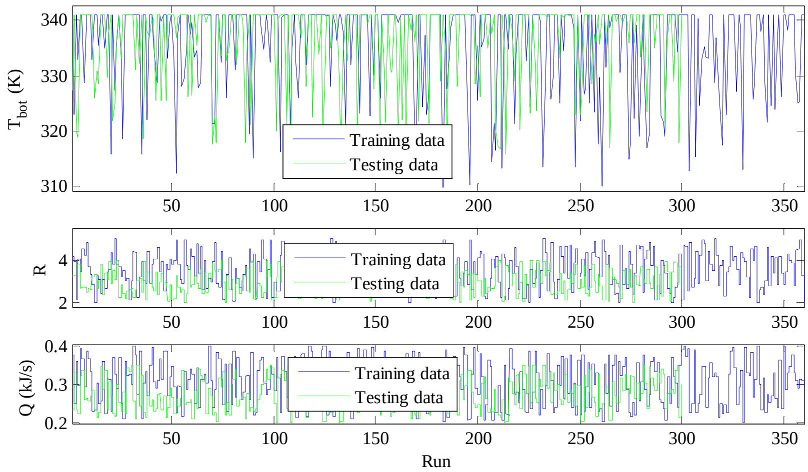

Fig. 4. Bottom segment temperature training and testing data sets

After training the Layer-Recurrent Network Models of the process, even though the models could not be obtained as physical ones, they were simulated using the manipulated variable values used for the training and the performance values of the models obtained from the training simulation are as shown in Table 3. It was observed from the table that the fit values of the models were appropriately very high and the means of absolute errors and the sums of squared errors were low enough to say that the models were well trained.

Table 3. Performance values of network training simulation

Performance criterion	**Performance value**	
	$\mathbf{T_{top}}$	$\mathbf{T_{bot}}$
Fit value	99.08	99.27
Mean of absolute errors	0.04	0.04
Sum of squared errors	0.80	1.33

Apart from simulating the developed models with the manipulated (input) variables used for the training, testing data set generated for the purpose of model testing and which was not used for the training of the models was also used to simulate the developed models and the performance values obtained from the testing simulation are given in Table 4. As can be seen from the table, in the testing simulation, the fit values were found to be very high. Also, the means of absolute errors and the sums of squared errors for both segment temperatures were obtained to be very low and appropriate for good models.

Table 4. Performance values of network testing simulation

Performance criterion	**Performance value**	
	T_{top}	**T_{bot}**
Fit value	98.74	98.63
Mean of absolute errors	0.05	0.07
Sum of squared errors	0.95	3.15

In addition, the representations of the Reactive Distillation Process of this work by the developed models were as well investigated by plotting the testing simulation results of both the top and the bottom segment temperatures against the measured ones as shown in Figures 5 and 6, respectively.

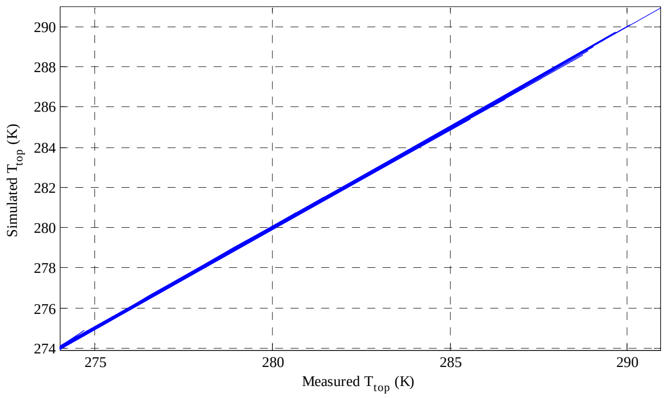

Fig. 5. Top segment simulation results of neural network testing

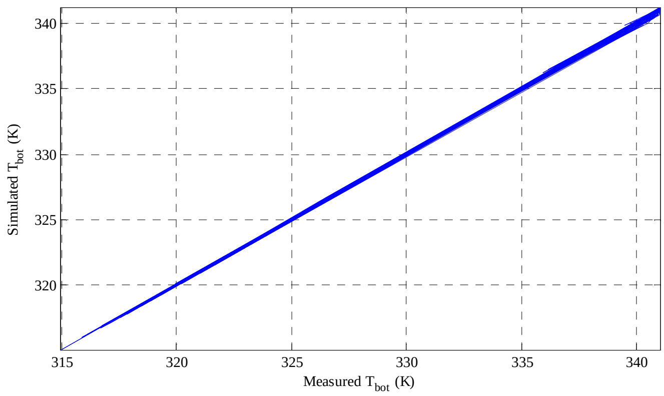

Fig. 6. Bottom segment simulation results of neural network testing

According to Figures 5 and 6, the 45 degree lines given by the plots of testing simulation temperatures against the measured ones are other indications of the good representations of the process by the developed models.

4. Conclusions

The very high fit values, the low means of absolute errors and the low sums of squared errors obtained from the training and the testing simulations of the Layer-Recurrent Neural Network models developed for the olefin metathesis Reactive Distillation Process have confirmed the validities of the developed models. Therefore, Layer-Recurrent Neural Network model has been discovered to be a good tool in representing the complex Reactive Distillation Process.

Acknowledgement

The authors acknowledge and appreciate the supports received from the Prime Ministry of The Republic of Turkey, Presidency for Turks Abroad and Related Communities for their programmes.

References

1. A. Giwa and S. Karacan. Black-Box Modelling of Ethyl Acetate Reactive Packed Distillation Column, *AU Journal of Technology,* 15(3):172-178, 2012b.
2. A. Giwa and S. Karacan. Modeling and Simulation of a Reactive Packed Distillation Column Using Delayed Neural Networks, *Chaotic Modeling and Simulation,* 2(1):101-108, 2012a.
3. A. Giwa and S. Karacan. Nonlinear Black-Box Modeling of a Reactive Distillation Process, *International Journal of Engineering Research & Technology,* 1(7):1-10, 2012c.
4. A. Giwa and S.O. Giwa. Optimization of Transesterification Reaction Integrated Distillation Column Using Design Expert and Excel Solver, *International Journal of Advanced Scientific and Technical Research,* 2(6):423-435, 2012.
5. A.K. Jana and P.V.R.K. Adari. Nonlinear State Estimation and Control of a Batch Reactive Distillation. *Chemical Engineering Journal,* 150(2-3):516-526, 2009.
6. Aspen. AspenONE V7.3, *Aspen Technology,* 2011.
7. D. M. Himmelblau. Applications of Artificial Neural Networks in Chemical Engineering, *Korean Journal of Chemical Engineering,* 17(4):373–392, 2000.
8. J. C. MacMurray and D. M. Himmelblau. Modeling and Control of a Packed Distillation Column Using Artificial Neural Networks, *Computers and Chemical Engineering,* 19(10):1077–1088, 1995.
9. L. S. Balasubramhanya and F. J. Doyle III. Nonlinear Model-Based Control of a Batch Reactive Distillation Column, *Journal of Process Control,* 10(2-3):209-218, 2000.
10. M. H. Beale, M. T. Hagan and H. B. Demuth. Neural Network Toolbox 7, *The MathWorks Inc.,* Apple Hill Drive, Natick MA, 2010.
11. M. Völker, C. Sonntag and S. Engell. Control of Integrated Processes: A Case Study on Reactive Distillation in a Medium-Scale Pilot Plant, *Control Engineering Practice,* 15(7):863–881, 2007.
12. Mathworks. MATLAB R2012b, The Language of Technical Computing, *The MathWorks, Inc.,* Natick, 2012.
13. R. Khaledi and B.R. Young. Modeling and model predictive control of composition and conversion in an ETBE reactive distillation column, *Industrial & Engineering Chemistry Research,* 44(9):3134-3145, 2005.

Stochastic Properties of Dynamical Systems Arising from (quantum) Spaces and Actions of (quantum) Groups

Nikolaj M. Glazunov

National Aviation University, Kiev.

Email: *glanm@yahoo.com*

Abstract:
We review novel results and investigate actions and transformations of (quantum) groups and semigroups on (quantum) spaces, present dynamical systems and zeta functions arising from these spaces, actions and transformations, discuss their stochastic properties.

Keywords: Dynamical System; Ergodic Transformation; Group Action; Equidistribution; Zeta function; Arithmetic Surface.

1 Introduction

A history of a semigroup and a group action on tori and projective spaces can be found among other in the book by A.G. Postnikov [1], in the paper by I.Ya. Gol'dsheid, G.A. Margulis [2] and in the supplement by B.M. Gurevich, Ya. G. Sinai [3] to the Russian translation of the English edition of the book by P. Billingsley [4].

Here we review novel results and investigate actions and transformations of (quantum) groups and semigroups on (quantum) spaces, present dynamical systems and zeta functions arising from these spaces, actions and transformations, discuss their stochastic properties.

2 Dynamical systems from spaces

It is well known that one-dimensional projective space $\mathbf{P}^1(\mathbf{Q})$ parametrize the set of dynamical systems in such a way that for any rational point

$Q \in \mathbf{P}^1(\mathbf{Q}), Q = (\frac{a}{b}, 1), a, b \in \mathbf{Z}, (a, b) = 1$ we naturally assiciate dynamical system $(\mathbf{T}, T_Q)$. Here $\mathbf{T} = \mathbf{R}/\mathbf{Z}, \mathbf{T}^{\mathbf{Z}} = (..., x_{-1}, x_0, x_1, ...), x_i \in \mathbf{T}, X = \{\mathbf{x} = (x_k) : bx_{k+1} = ax_k \text{ for all } k \in \mathbf{Z}\}, T_Q : X \to X$. More generally, for any primitive polynomial $g(x) \in \mathbf{Z}[x]$ of degree $d \geq 1$ it is possible to construct its Frobenius and companion matrices and define a homeomorphism T_F of a compact $d-$dimensional subgroup of $\mathbf{T}^d$. These considerations can be extended to elliptic curves [5] and to abelian varieties. For elliptic curves authors of the paper [5] implement these by the following way. Let $q \in \mathbf{Q}_p$ and $\log^+ x$ denotes $\max\{\log x, 0\}$. For a generic element x of $\mathbf{Z}_p$ authors define q-transformation $T_q(x)$ (a p-adic analogue of the β-transformation). Then the topological entropy of the p-adic β-transformation is given by $h(T_q) = \log^+ |q|_p$ ([5], Theorem 4.1). If $|q|_p \geq 1$ then the map T_q is ergodic with respect to Haar measure for $|q|_p > 1$ and is not ergodic for $|q|_p = 1$ ([5], Theorem 4.2). Let $Per_n(T_q)$ denotes the subgroup of $\mathbf{Z}_p$ consisting of elements of period n under T_q. Let U be the set of unit roots of $\mathbf{Q}_p$ and $q \in \mathbf{Q}_p \setminus U$. Then

$$\log |Per_n(T_q)| = n \log^+ |q|_p.$$

([5], Theorem 4.3). The authors use the topological entropy and measure theoretical arguments based on volume growth rate and arithmetic of $\mathbf{Z}_p$.
Let Q be a rational point of an elliptic curve over $\mathbf{Q}$ and let $\hat{h}(Q)$ be the global canonical height on rational points of the elliptic curve. Then with the definitions and assumptions of the paper [5] and $q = a/b = x(Q)$, (i) the entropy of T_Q is given by $h(T_Q) = 2\hat{h}(Q)$, and (ii) the asymptotic growth rate of the periodic points is given by the division polynomial $\nu_n(x)$: $\log |Per_n(T_Q| \sim \log |b^n \nu_n(q)|$ as $n \to \infty$. ([5], Theorem 5.2). In the case authors use also the elliptic analogue of Baker's theorem, which described in paper [6] and in paper [7] .

3 Dynamical systems on probability spaces

Let (X, B, μ, T) be a dynamical system on standard probability space with $T : X \to X$ is measurable, almost surely one to one, preserves μ, for which it is an ergodic transformation. Random dynamical systems relate a partial case of bundle dynamical systems by I. Cornfeld, S. Fomin, and Ya. Sinai [8]. Measurable partition of the space X transforms the initial random dynamical system into a symbolic dynamical system. We will present novel symbolic dynamical systems and their applications.

4 Rigid and weakly mixing ergodic transformations

In papers [9] and [10] authors present resent results on genericity of rigid and multiply recurrent infinite measure preserving and nonsingular transformations and on measurable sensitivity. In the paper [11] authors investigate properties of uniformly rigid transformations and analyze the compatibility of uniform rigidity and measurable weak mixing along with some of their asymptotic convergence properties. All spaces of the paper under review are considered simultaneously as topological spaces and as measure spaces. Presented results concern either the measurable dynamics on the spaces or the interplay between the measurable and topological dynamics. The notion of uniform rigidity was introduced as a topological version of rigidity by S. Glasner and D. Maon [12]. Authors of the paper [11] considers functional analytic properties of uniform rigidity that is similar to the properties of rigidity. Theorem 1 ([11]). Every totally ergodic finite measure-preserving transformation on a Lebesgue space has a representation that is not uniformly rigid, except in the case where the space consists of a single atom.

The proof of the theorem connects with results of authors of the theorem that uniform rigidity and weak mixing are mutually exclusive notions on a Cantor set, and follows from the Jewett-Krieger Theorem by K. Peterson [13].

5 Superrigidity for groups

The concept of superrigidity was introduced by G. D. Mostow [14] and by G. A. Margulis [15] in the context of studying the structure of lattices in rank one and higher rank Lie groups respectively. The notion of property (T) for locally compact groups was defined by D. Kazhdan [16] and the notion of relative property (T) for inclusion of countable groups $\Gamma_0 \subset \Gamma$ was defined by G. Margulis [17]. Now considerthe orbit equivalence (OE) superrigidity. One of the first result of this type of superrigidity was obtained by A. Furman [18], who combined the cocycle superrigidity by R. Zimmer [19] with ideas from geometric group theory to show that the actions $SL_n(\mathbf{Z})$ on $\mathbf{T}^n (n \geq 3)$ are OE superrigid. The deformable actions of rigid groups are OE superrigid by S. Popa [20]. The main result of the paper by A. Ioana [21] is the Theorem A on orbit equivalence (OE) superrigidity. As a consequence of Theorem A the author of the paper [21] can constructs uncountable many non-OE profinite actions for the arithmetic groups $SL_n(\mathbf{Z})(n \geq 3)$, as well as for their finite subgroups, and for the groups $SL_m(\mathbf{Z}) \times \mathbf{Z}^m (m \geq 2)$. The author deduces Theorem A as a consequence of the Theorem B on cocycle superrigidity.

Let the action of Γ on X be a free ergodic measure-preserving profinite action (i.e., an inverse limit of actions Γ on X_n with X_n finite) of a countable property (T) group Γ (more generally, of a group Γ which admits an infinite normal subgroup Γ_0 such that the inclusion $\Gamma_0 \subset \Gamma$ has relative property (T) and Γ/Γ_0 is finitely generated) on a standard probability space X. The author prove that if $\omega : \Gamma \times X \to \Lambda$ is a measurable cocycle with values in a countable group Λ, then ω is a cohomologous to a cocycle $\omega^{'}$ which factors through the map $\Gamma \times X \to \Gamma \times X_n$, for some n. As a corollary, he shows that any free ergodic measure-preserving action Λ on Y comes from a (virtual) conjugancy of actions.

6 Equidistribution for orbits of nonabelian semigroups on the torus

Furstenberg [22] and Berent [23] have investigated the action of abelian semigroups on the torus $\mathbf{T}^d$ for $d = 1$ and $d > 1$ respectively. Their results answer problems raising by H. Furstenberg [24]. Authors of the paper [25] extend to the noncommutative case some results of Furstenberg and Berent

7 Zeta functions from spaces and dynamical systems

Recall that Dedekind has defined zeta function for polynomials over prime finite field. The zeta function is trivial and equal to $\frac{1}{1-pz}$. However, combining the zeta function with Chebyshev-Mobius inversion formula we obtain the number of monic irreducible over $\mathbf{F}_p$ polynomials of natural degree m. Riemann and Dedekind zeta functions are first examples of motivic zeta functions. The authors of the paper [26] investigate sufficient conditions for (i) the existence of trace formulae for the Reidemeister number of a group endomorphism; (ii) the rationality of the Reidemeister zeta function and the convergence of the Nielsen zeta function; (iii) the equality of Reidemeister torsion of a group endomorphism to a special value of the Reidemeister zeta. This interesting survey[26] includes recent results on trace formulae, rationality and convergence of zeta functions and relations between special values of zeta functions and some simply homotopy invariants. The general setting of the paper [27] is braided zeta functions in q-deformed geometry. In the framework authors define a zeta function for any rigid object in a ribbon braided category. In the ribbon case they define braided Hilbert series for objects in an Abelian braided category. We will present some other types of zeta-functions.

8 Dynamical Systems from Arithmetic Surfaces

8.1 Sato-Tate case

Let $y^2 = f(x), f(x) = x^3 + cx + d$ be a cubic polynomial in prime finite field $\mathbf{F}_p$. For the number $\#C_p$ of points of the curve $C : y^2 = f(x)$ in $\mathbf{F}_p$ the well known formula

$$\#C_p = \sum_{x=0}^{p-1} \left(1 + \left(\frac{f(x)}{p}\right)\right),$$

take place, where $\left(\frac{f(x_0)}{p}\right)$ is the Legendre symbol with a numerator which is equal to the value of the polynomial $f(x_0)$ in point $x_0 \in \mathbf{F}_p$. It is ease to see that $\#C_p = p - a_p$, where

$$a_p = -\sum_{x=0}^{p-1} \left(\frac{f(x)}{p}\right)$$

If C is the elliptic curve , then the number of points $\#C(\mathbf{F}_p)$ of the projective model of the curve in $\mathbf{F}_p$ is represented by the formula $\#E_p = 1+p-a_p$, where $a_p = 2\sqrt{p}\cos\varphi_p$, If C is not the elliptic curve, then the value a_p is equal 1, -1 or 0 and ease to compute. In both cases compute: $\varphi_p = \arccos(a_p/2\sqrt{p})$ and reduce it to the interval $[0, \pi]$.

Let E be an elliptic curve over rational numbers $\mathbf{Q}$ which does not admit complex multiplication. Sato and Tate [28] have given computational and theoretical evidences suggesting the distribution of angles φ_p.

Recently L. Clozel, M. Harris, N. Shepherd-Barron, R. Taylor and their colleagues have proved the Sato-Tate conjecture for all elliptic curves E over $\mathbf{Q}$ (and over some its extensions) satisfying the mild condition of having multiplicative reduction at some prime.

Langlands conjectured that some symmetric power $L-$functions extend to an entire function and coincide with certain automorphic $L-$functions.

Theorem (Clozel, Harris, Shepherd-Barron, Taylor). Suppose E is an elliptic curve over Q with non-integral $j-$invariant. Then for all $n > 0, L(s, E, Sym^n)$ extends to a meromorphic function which is holomorphic and non-vanishing for $Re(s) \geq 1 + n/2$.

These conditions suffice to prove the Sato-Tate conjecture.

Theoretical considerations give

Proposition EC. It is possible the arithmetic modeling of the Brownian motion by quantity a_p.

8.2 Kloosterman sums

Let

$$T_p(c,d) = \sum_{x=1}^{p-1} e^{2\pi i (\frac{cx + \frac{d}{x}}{p})}$$

$$1 \leq c, d \leq p-1;\ x, c, d \in \mathbf{F}_p^*$$

be a Kloosterman sum.

By A. Weil estimate

$$T_p(c,d) = 2\sqrt{p} \cos \theta_p(c,d)$$

There are possible two distributions of angles $\theta_p(c,d)$ on semiinterval $[0, \pi)$:

a) *p is fixed and c and d varies over $\mathbf{F}_p^*$; what is the distribution of angles $\theta_p(c,d)$ as $p \to \infty$;*

b) *c and d are fixed and p varies over all primes not dividing c and d.*

For the case *a*) N. Katz [29] and A. Adolphson [30] proved that θ are distributed on $[0, \pi)$ with density $\frac{2}{\pi}\sin^2 t$.
Let

$$cd \not\equiv 0 \bmod p,\ T_p(c,d) = \sum_{x=1}^{p-1} e^{2\pi i(\frac{cx+\frac{d}{x}}{p})}$$

the Kloosterman sum. By A. Weil, $T_p(c,d) = 2\sqrt{p}\cos\theta_p(c,d)$. Compute $T_p, \cos\theta_p, \theta_p$ and reduce θ_p to the interval $[0, \pi]$. Experiments demonstrate random behavior of angles of Kloosterman sums.

Theoretical considerations give

Proposition KS. It is possible the arithmetic modeling of the Brownian motion by Kloosterman sums.

Conclusions

We have presented a review of new results on actions and transformations of (quantum) groups and semigroups on (quantum) spaces, have presented dynamical systems and zeta functions arising from these spaces, actions and transformations, discussed their stochastic properties.

References

[1] A.G. Postnikov, Selected papers (In Russian), Fizmatlit, Moscow, 2005.

[2] I.Ya. Gol'dsheid, G.A. Margulis, Uspekhi Mat. Nauk 44, no. 5, 13-60, 1989.

[3] B.M. Gurevich, Ya. G. Sinai, Algebraic automorphisms of the torus and Markov chains.

[4] P. Billingsley, Ergodicheskaya teoriya i informatsiya (Ergodic Theory and Information), Mir, Moscow, 1969.

[5] D'Ambros, P.; Everest, G.; Miles, R.; Ward, T. Dynamical systems arising from elliptic curves. Colloquium Math., vol. 84/85 (2000) 95 - 107.

[6] S. David. Mem. Soc. Math. France 62 (1995).

[7] G. Everest and T. Ward. Experiment. Math. 7 (1998), 305-316.

[8] I. Cornfeld, S. Fomin, and Ya. Sinai, Ergodic Theory, Grundlehren der Mathematischen Wissenschaften (Fundamental Principles of Mathematical Sciences), vol. 245 (1982), Springer-Verlag, New York.

[9] O. Ageev and C. Silva. Proceedings of the 16ty Summer Conference on General Topology and its applications (New York), Topology Proc. 26, No. 2, 357-365 (2002).

[10] J. James, T. Koberda, K. Lendsey, C. Silva. Proc. Amer. Math. Soc., 136, 3549-3559 (2008).

[11] James, Jennifer; Koberda, Thomas; Lindsey, Kathryn; Silva, Cesar E.; Speh, Peter. On ergodic transformations that are both weakly mixing and uniformly rigid. New York J. Math. 15, 393-403 (2009).

[12] S. Glasner and D. Maon. Ergodic Theory Dynam. Systems 9, 309-320 (1989).

[13] K. Peterson. Ergodic Theory. Cambridge Studies in Advanced Mathematics, 2. Cambridge University Press, Cambridge (1983).

[14] G. D. Mostow. Strong rigidity of locally symmetric spaces, Princeton University Press, Princeton, N.J., Annals of Mathematics Studies, No. 78. (1973).

[15] G. A. Margulis Discrete subgroups of semisimple Lie groups. Ergeb. Math. Grenzgeb. 17, Springer-Verlag, Berlin (1991; Zbl)]

[16] D. Kazhdan. Funct. Anal. and its Appl. 1, 6365 (1967).

[17] G. Margulis. Ergodic Theory Dynam. Systems 2, 383396 (1982).

[18] A. Furman. Ann. of Math., vol. 150, 2, 1059-1081, 1083-1108 (1999).

[19] R. Zimmer. Ergodic theory and semisimple groups, Monographs in Mathematics, 81, Birkhuser Verlag, Basel, x+209 pp. (1984).

[20] S. Popa. International Congress of Mathematicians. Vol. I, Eur. Math. Soc., Zurich, pp. 445-477 (2007).

[21] Ioana, Adrian. Cocycle superrigidity for profinite actions of property (T) groups, Duke Math. J. 157, No. 2, 337-367 (2011).

[22] H. Furstenberg. Math. System Theory 1 (1967), 1-40.

[23] D. Berent. Trans. Amer. Math. Soc. 286 (1984), no. 2, 505-535.

[24] H. Furstenberg. Tata Ins. Fund. Res. Stud. Math., vol. 14, Tata Ins. Fund. Res., Bombay, 105-117 (1998).

[25] Bourgain, Jean; Furman, Alex; Lindenstrauss, Elon; Mozes, Shahar. Stationary measures and equidistribution for orbits of nonabelian semigroups on the torus. J. Am. Math. Soc. 24, No. 1, 231-280 (2011).

[26] Fel'shtyn, Alexander; Hill, Richard. Trace formulae, zeta functions, congruences and Reidemeister torsion in Nielsen theory. Forum. Math. 10, no. 6, 641-663 (1998).

[27] Shahn, Majid; Ivan, Tomasic. On braided zeta functions. Bull. Math. Sci. 1, 379-396 (2011).

[28] B.J. Birch, J. London Math. Soc., 43, 57-60 (1968).

[29] Katz N. Gauss sums, Kloosterman sums, and monodromy groups. Princeton university press, (1988), 246p.

[30] Adolphson A. Journ. rein. angew. Math., 395, (1989), pp.214-220.

[31] N.M. Glazunov. Arithmetic maps and their modeling (In Russian), *International Conference Avia-2011*, Kiev, NAU, Vol.1. P.6.1-6.3, 2011.

[32] N.M. Glazunov. Dynamics, Coding And Entropies, *Fourth World Congress, AVIATION IN THE XXI-st CENTURY*, NAU, Kiev, P.18.39 18.42, 2010.

[33] N.M. Glazunov. Methods to Justifying of Arithmetic Hypotheses and Computer Algebra, *Programmirovanie*, N 3, P.2-8, 2006.

[34] N.M. Glazunov. On moduli spaces, equidistribution, bounds and rational points of algebraic curves, *Ukrainian Math. Journal*, 9: 1174-1183, 2001.

A Mathematical Model of the Metabolism of a Cell. Self-organization and Chaos*

Valerii I. Grytsay[a], Iryna V. Musatenko[b]

[a]Bogolyubov Institute for Theoretical Physics, Kyiv, Ukraine
E-mail: vgrytsay@bitp.kiev.ua
[b]Taras Shevchenko National University of Kyiv, Faculty of Cybernetics, Kyiv, Ukraine
E-mail: ivmusatenko@gmail.com

Abstract: Using the classical tools of nonlinear dynamics, we study the process of self-organization and the appearance of the chaos in the metabolic process in a cell with the help of a mathematical model of the transformation of steroids by a cell *Arthrobacter globiformis*. We constructed the phase-parametric diagrams obtained under a variation of the dissipation of the kinetic membrane potential. The oscillatory modes obtained are classified as regular and strange attractors. We calculated the bifurcations, by which the self-organization and the chaos occur in the system, and the transitions "chaos-order", "order-chaos", "order-order," and "chaos-chaos" arise. Feigenbaum's scenarios and the intermittences are found. For some selected modes, the projections of the phase portraits of attractors, Poincaré sections, and Poincaré maps are constructed. The total spectra of Lyapunov indices for the modes under study are calculated. The structural stability of the attractors is demonstrated. A general scenario of the formation of regular and strange attractors in the given metabolic process in a cell is found. The physical nature of their appearance in the metabolic process is studied.
Keywords: Mathematical model, Metabolic process, Self-organization, Phase portrait, Deterministic chaos, Regular attractor, Strange attractor, Bifurcation, Poincaré section, Poincaré map, Lyapunov indices.

1. Introduction

In the present work, we continue the study of the mathematical model of the metabolic process in a cell *Arthrobacter globiformis*. It is based on the process of transformation of steroids in a bioreactor, which is well investigated in experiments [1]. The constructed mathematical model allows us to determine the internal and external parameters, with which the model describes the stationary modes of a bioreactor. The studies within the model showed that autooscillations must appear in the biochemical reaction under certain conditions [2-17]. These autooscillations predicted as early as in 1985 [2] were found experimentally in [18, 19].

Analogous autooscillations are observed in the processes of photosynthesis, glycolysis, variations of the calcium concentration in a cell, oscillations in heart muscle, and other biochemical systems [20-24].

* The work is supported by the project N 0112U000056 of the National Academy of Sciences of Ukraine.

The study of such autooscillations will allow one to investigate the internal dynamics of metabolic processes in cells, to find the structural-functional connections in a cell, by which its vital activity runs, and to clarify the evolution of the formation of these connections. The application of the mathematical apparatus of nonlinear dynamics to the study of metabolic processes will allow one to develop the general methods of synergetics considering the physical laws of self-organization in the Nature.

2. The Mathematical Model

The mathematical model of the metabolic process running in a cell *Arthrobacter globiformis* at the transformation of steroids is constructed according to the general scheme of this process presented in Fig. 1. The model is based on the results of experimental studies of the process under flowing-through conditions with a fermenter in porious granules with immobilized cells *Arthrobacter globiformis* [3, 4].

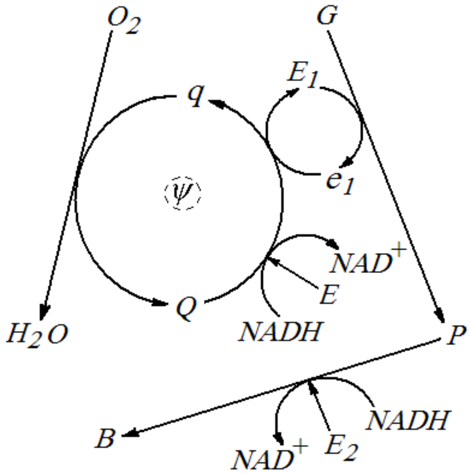

Fig. 1. General scheme of the metabolic process in a cell *Arthrobacter globiformis*.

The variation of the concentration of hydrocortisone (G) is described by the equation

$$\frac{dG}{dt} = \frac{G_0}{N_3 + G + \gamma_2 \psi} - l_1 V(E_1) V(G) - \alpha_3 G. \tag{1}$$

Under the action of the diffusion and the flow into pores of a macroporous granule to cells, hydrocortisone comes to the region of localization of the enzyme 3-ketosteroid-Δ-dehydrogenase (E_1) (term $\frac{G_0}{N_3 + G + \gamma_2 \psi}$) and is

transformed by this enzyme into prednisolone (term $l_1V(E_1)V(G)$). A part of hydrocortisone is taken out from the biosystem by the flow (term $\alpha_3 G$).
Here and below, the function $V(X)$ characterizes the adsorption of the enzyme in the region of local binding into active complexes; $V(X) = X/(1+X)$.
The variation of the concentration of prednisolone (P):

$$\frac{dP}{dt} = l_1V(E_1)V(G) - l_2V(E_2)V(N)V(P) - \alpha_4 P. \quad (2)$$

Prednisolone formed in the process (term $l_1V(E_1)V(G)$) is transformed by the enzyme 20β-oxysteroid-dehydrogenase (E_2) to its 20β-oxyderivative (term $l_2V(E_2)V(N)V(P)$). Under the action of a flow (term $\alpha_4 P$), a part of prednisolone goes out into the external solution.
The variation of the concentration of 20β-oxyderivative of prednisolone (B):

$$\frac{dB}{dt} = l_2V(E_2)V(N)V(P) - k_1V(\psi)V(B) - \alpha_5 B. \quad (3)$$

The increase of the concentration of B occurs as a result of the transformation of prednisolone (term $l_2V(E_2)V(N)V(P)$). Its decrease is due to the use of 20β-oxyderivative by cells in one of the possible modifications of the Krebs cycle (term $k_1V(\psi)V(B)$), which increases the level of $NAD \cdot H$. Under the action of a flow (term $\alpha_5 B$), B is washed out into the external solution.
The variation of the concentration of the oxidized form of 3-ketosteroid-Δ-dehydrogenase (E_1):

$$\frac{dE_1}{dt} = E_{10}\frac{G^2}{\beta_1 + G^2}\left(1 - \frac{P+mN}{N_1+P+mN}\right) - \\ -l_1V(E_1)V(G) + l_4V(e_1)V(Q) - \alpha_1 E_1. \quad (4)$$

The biosynthesis of the enzyme is described by the term $E_{10}\frac{G^2}{\beta_1 + G^2}\left(1 - \frac{P+mN}{N_1+P+mN}\right)$, which is defined by the activation by the substrate G and the inhibition by the reaction products P and N. The decrease of the concentration of this form of the enzyme in the process of transformation of hydrocortisone is given by the term $l_1V(E_1)V(G)$, and its increase in the process of reduction of the respiratory chain corresponds to the term $l_4V(e_1)V(Q)$. The inactivation of the enzyme due to the proteolysis is described by the term $\alpha_1 E_1$.

The variation of the concentration of the reduced form of 3-ketosteroid-Δ-dehydrogenase (e_1):

$$\frac{de_1}{dt} = -l_4 V(e_1)V(Q) + l_1 V(E_1)V(G) - \alpha_1 e_1. \tag{5}$$

Its level decreases in the process of reduction of the respiratory chain (term $-l_4 V(e_1)V(Q)$) and due to the inactivation (term $\alpha_1 e_1$) and increases at the transformation of hydrocortisone (term $l_1 V(E_1)V(G)$).
The variation of the level of the oxidized form of the respiratory chain (Q)

$$\frac{dQ}{dt} = 6lV(2-Q)V(O_2)V^{(1)}(\psi) - l_6 V(e_1)V(Q)_1 - l_7 V(Q)V(N), \tag{6}$$

where $V^{(1)}(\psi) = 1/(1+\psi^2)$. We accept that the concentration of menaquinone $Q^0 + q^0 = 2$, where q is the reduced form of the respiratory chain.
The respiratory chain is oxidized by oxygen (term $6lV(2-Q)V(O_2)V^{(1)}(\psi)$) and is reduced with the help of e_1 (term $-l_6 V(e_1)V(Q)$) and due to the high level of $NAD \cdot H$ (term $-l_7 V(Q)V(N)$).
The variation of the concentration of oxygen (O_2):

$$\frac{dO_2}{dt} = \frac{O_{20}}{N_5 + O_2} - lV(2-Q)V(O_2)V^{(1)}(\psi) - \alpha_7 O_2. \tag{7}$$

Under the action of a flow (terms $\frac{O_{2_0}}{N_5 + O_2}$ and $\alpha_7 O_2$), the level of aeration of a cell is changed. The concentration of oxygen decreases at the oxidation of the respiratory chain (term $-lV(2-Q)V(O_2)V^{(1)}(\psi)$).
The variation of the concentration of 20β-oxysteroid-dehydrogenase (E_2):

$$\frac{dE_2}{dt} = E_{20}\frac{P^2}{\beta_2 + P^2}\frac{N}{\beta + N}(1 - \frac{B}{N_2 + B}) - \\ -l_{10} V(E_2)V(N)V(P) - \alpha_2 E_2 \tag{8}$$

The increase of the level of the given enzyme occurs due to the biosynthesis: $E_{20}\frac{P^2}{\beta_2 + P^2}\frac{N}{\beta + N}(1 - \frac{B}{N_2 + B})$. Prednisolone and $NAD \cdot H$ are activators of this process, and 20β-oxyderivative is an inhibitor. The decrease of the level of the given enzyme occurs as a result of the inactivation ($-\alpha_2 E_2$) and the process of transformation of prednisolone ($-l_{10}V(E_2)V(N)V(P)$).

$$\frac{dN}{dt} = -l_2V(E_2)V(N)V(P) - l_7V(Q)V(N) + \\ + k_2V(B)\frac{\psi}{K_{10}+\psi} + \frac{N_0}{N_4+N} - \alpha_6 N. \quad (9)$$

The level of the co-enzyme N decreases in the process of transformation $P \Rightarrow B$, in the process of reduction of the respiratory chain ($-l_7V(Q)V(N)$), and due to a flow ($-\alpha_6 N$). It increases at the use of B by cells in the Krebs cycle as a substrate ($k_2V(B)\frac{\psi}{K_{10}+\psi}$) and in the presence of endogenous substrates ($\frac{N_0}{N_4+N}$) in the environment.

The variation of the level of kinetic membrane potential (ψ):

$$\frac{d\psi}{dt} = l_5V(E_1)V(G) + l_8V(N)V(Q) - \alpha\psi . \quad (10)$$

The kinetic membrane potential arises at the transformation of hydrocortisone ($l_5V(E_1)V(G)$) and the reduction of the respiratory chain ($l_8V(N)V(Q)$) at a high level of $NAD \cdot H$ and decreases due to other metabolic processes ($-\alpha\psi$). The variation of the level of ψ changes its regulatory role (1), (3), (6), (7), (9). If the potential is high, the respiratory chain is blocked and held in the reduced state.

The main parameters of the system, with which we fit the relevant experimental data, are as follows: $l = l_1 = k_1 = 0.2$; $l_2 = l_{10} = 0.27$; $l_5 = 0.6$; $l_4 = l_6 = 0.5$; $l_7 = 1.2$; $l_8 = 2.4$; $k_2 = 1.5$; $E_{10} = 3$; $\beta_1 = 2$; $N_1 = 0.03$; $m = 2.5$; $\alpha = 0.033$; $a_1 = 0.007$; $\alpha_1 = 0.0068$; $E_{20} = 1.2$; $\beta = 0.01$; $\beta_2 = 1$; $N_2 = 0.03$; $\alpha_2 = 0.02$; $G_0 = 0.019$; $N_3 = 2$; $\gamma_2 = 0.2$; $\alpha_5 = 0.014$; $\alpha_3 = \alpha_4 = \alpha_6 = \alpha_7 = 0.001$; $O_{20} = 0.015$; $N_5 = 0.1$; $N_0 = 0.003$; $N_4 = 1$; $K_{10} = 0.7$.

The study of solutions of the given mathematical model was carried out with the help of the theory of nonlinear differential equations [25-27].

In the numerical solution of this autonomous system of nonlinear differential equations, we used the Runge--Kutta--Merson method. The accuracy of calculations was set to be 10^{-8} . To attain the reliability of a solution, when the system passes from the initial transient phase onto the asymptotic solution with

an attractor, the duration of calculations was taken to be 10^6. For this time interval, the trajectory "sticks" onto the appropriate attractor.
The various types of autooscillatory modes are studied with the help of the construction of exact phase-parametric diagrams. We found the scenarios of appearance of bifurcations at the transition of the dynamical process from one type of an attractor to another one. For the most characteristic modes, we calculated the total spectra of Lyapunov indices (Table 1).
To construct a phase-parametric diagram, we used the method of section. In the phase space of trajectories of the system, we place a cutting plane with *P* = 0.2. Such choice is explained by the symmetry of oscillations relative to this point of this variable in multiple modes. If the trajectory *P*(*t*) crosses this plane in a certain direction, we mark the value of chosen variable (e.g., *G*) on the phase-parametric diagram. In such way, we have the point corresponding to the section of a trajectory by the two-dimensional plane. If the multiple periodic limiting cycle appears, we obtain a number of points, which will be coincide in a period. If a deterministic chaos arises, the points of intersection of trajectories by the plane will be placed chaotically.
In order to uniquely identify the form of an attractor for the chosen points, we calculated the total spectrum of Lyapunov indices and determined their sum $\Lambda = \sum_{j}^{10} \lambda_j$ (see Table 1). The calculation was carried out by Benettin's algorithm with orthogonalization of the vectors of perturbation by the Gram--Schmidt method [26, 28, 29].

3. Results of Studies

We now consider the dynamics of modes within the mathematical model (1)-(10) under a variation of the dissipation of a kinetic membrane potential α (10) [16, 17]. We found the autooscillatory and chaotic modes with various multiplicities. The projections of their phase portraits have a characteristic form shown in Fig. 2,a,b.

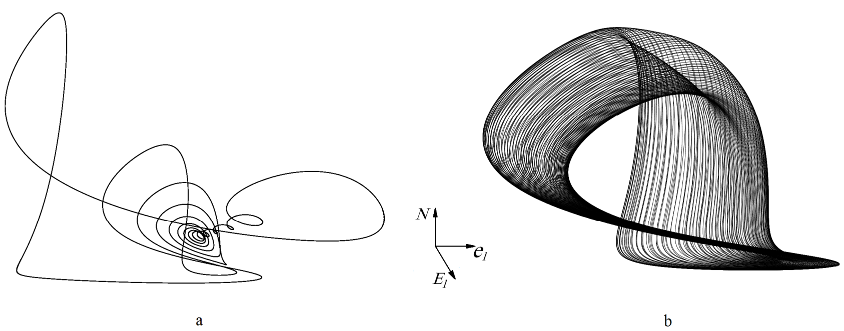

Fig. 2. Projections of the phase portraits of regular attractors: a – autoperiodic cycle $14 \cdot 2^0$ for $\alpha = 0.033$; b – quasiperiodic cycle $\approx 31 \cdot 2^0$ for $\alpha = 0.0321375$.

Let us consider a part of the bifurcation diagram not studied earlier. In Fig. 3, we show the bifurcation diagram for $\alpha \in (0.032159, 0.32166)$.

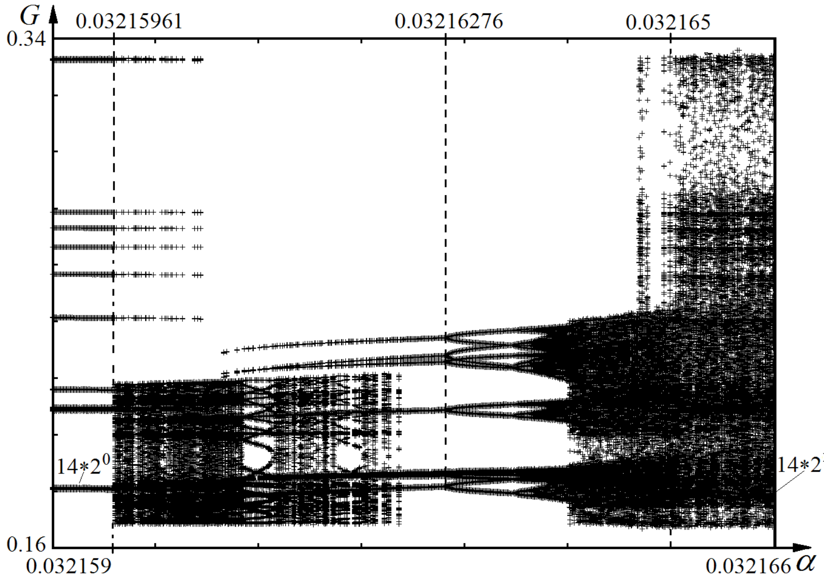

Fig. 3. Bifurcation diagram of the system for $\alpha \in (0.032159, 0.32166)$.

For $\alpha \in (0.0321590, 0.03215960)$, the regular attractor of the 14-fold period $14 \cdot 2^0$ is kept in the system. For $\alpha = 0.03215961$, we observe the appearance of the period doubling bifurcation with the generation of the regular attractor $14 \cdot 2^1$ (Table 1). Then for $\alpha = 0.03215962$, there arises the bifurcation of the generation of a two-dimensional torus (the Neimark bifurcation). The configuration of kinetic curves is instantly changed, and the quasiperiodic attractor with *n*-fold period is established on the toroidal surface $\approx n \cdot 2^0 (t)$ (Figs. 4,a and 5,a).

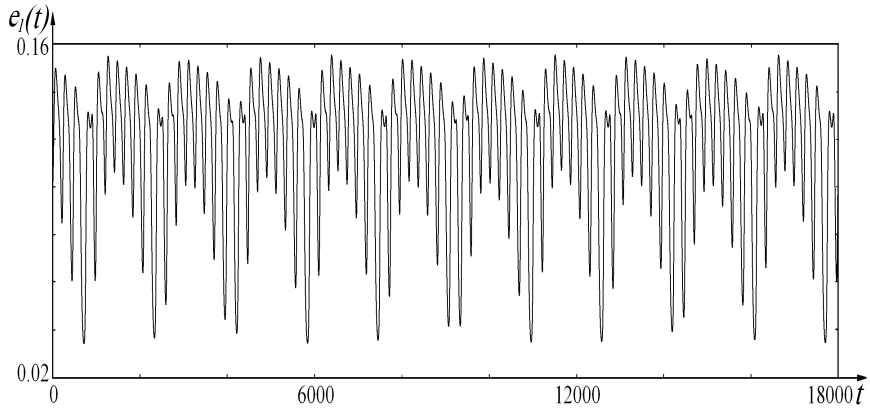

a - regular attractor of the quasiperiodic cycle $\approx n^* 2^0$ on the toroidal surface for $\alpha = 0.03215962$.

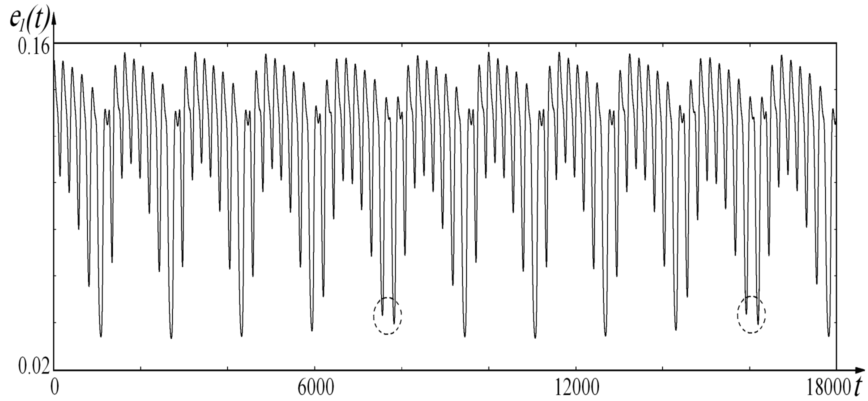

b - regular attractor $36 \cdot 2^0$ for $\alpha = 0.032162$.

Fig. 4. Kinetic curve of the variable $e_1(t)$.

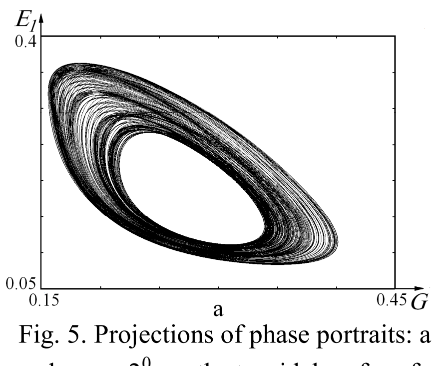

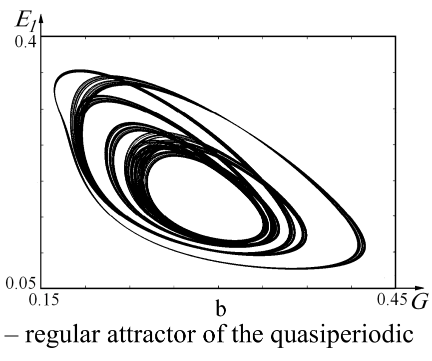

Fig. 5. Projections of phase portraits: a – regular attractor of the quasiperiodic cycle $\approx n \cdot 2^0$ on the toroidal surface for $\alpha = 0.03215962$; b – strange attractor $7 \cdot 2^x$ for $\alpha = 0.032164$.

As α increases, the given attractor loses the stability, by passing periodically to the 14-fold limiting cycle ($\alpha = 0.032160$), which corresponds to the gaps in Fig. 3,a. In addition, other various multiple modes arise. For example, for $\alpha =$ 0.032161, 0.0321615, and 0.032162, the regular attractors $29 \cdot 2^0$, $7 \cdot 2^0$, and $36 2^0$ appear, respectively (Fig. 4,b). As α increases, we see the appearance of bifurcations of the limiting cycle. Moreover, the instant structural rearrangement of the type "order-order" occurs; i.e., as a result of the self-organization, the regular attractor of some form is replaced instantly by a regular attractor of some other form. In this case, the trajectories leave the region of attraction of the attractor and are drawn in the region of attraction of another regular attractor.
The interesting scenario of the metabolic process is observed in the interval $\alpha \in (0.0321626, 0.032164)$. In Fig. 6, we present a magnified part of the bifurcation diagram in Fig. 3.

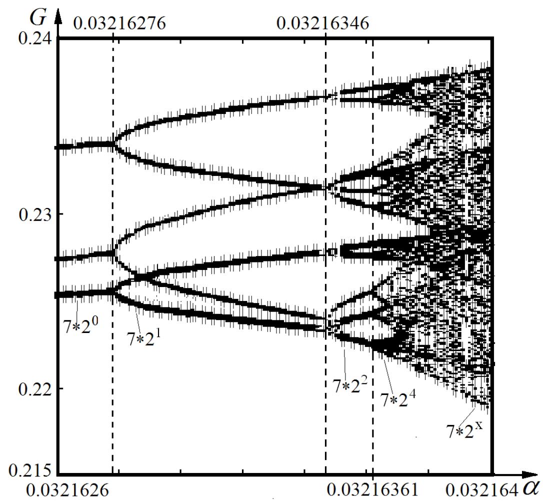

Fig. 6. Phase-parametric diagram of the system for $\alpha \in (0.0321626, 0.32164)$, where Feigenbaum's scenario is observed.

At the beginning of the interval at $\alpha = 0.0321626$, the regular attractor $7 \cdot 2^0$ is formed on the toroidal surface. For $\alpha_j = 0.03216276$, the bifurcation yields the doubling of the period, and the regular attractor $7 \cdot 2^1$ arises on the toroidal surface. For $\alpha_{j+1} = 0.03216346$ and $\alpha_{j+2} = 0.03216361$, we see the attractors $7 \cdot 2^2$ and $7 \cdot 2^4$, respectively. This sequence of bifurcations satisfies the relation

$$\lim_{t\to\infty}\frac{\alpha_{j+1}-\alpha_j}{\alpha_{j+2}-\alpha_{j+1}}\approx 4.667\,.$$

This number is very close to Feigenbaum's universal constant $\delta =$ 4.669211660910… characterizing the infinite cascade of bifurcations at the transition to a deterministic chaos. Thus, as the coefficient of dissipation α increases in this region, the period of a complicated regular attractor on the torus is doubled by Feigenbaum's scenario [37-40].

The further increase in α causes a deviation from the given scenario and the formation of the strange attractor $7\cdot 2^x$ ($\alpha = 0.032164$, Fig. 5,b) as a result of the intermittency. But then, for $\alpha = 0.032174$, the strange attractor $14\cdot 2^x$ appears (Fig. 7,b). In the interval $\alpha \in (0.032164, 0.032174)$ as a result of the intermittency of these chaotic cycles, we observe the transition between them: $(7\leftrightarrow 14)\cdot 2^x$. In Fig. 7,a for $\alpha = 0.032165$, we show a projection of the phase portrait of a mutual transition of the given strange attractors. Figure 8 presents the kinetic curve for the variable $e_1(t)$ for tis mode. We observe the transition "chaos-chaos": $(7\leftrightarrow 14)\cdot 2^x$. Moreover, the strange attractor $7\cdot 2^x$ on the left and the strange attractor $14\cdot 2^x$ on the right move toward each other. Since there are no other attractors of the system in this region, the trajectory is chaotically kept in the region of attraction of the strange attractor $14\cdot 2^x$ or the strange attractor $7\cdot 2^x$ Under the effect of bifurcations, the trajectory is aperiodically drawn in one of the regions of the given strange attractors after the transient process. According to the values of higher Lyapunov indices (Table 1), the formed limiting set is unstable by Lyapunov.

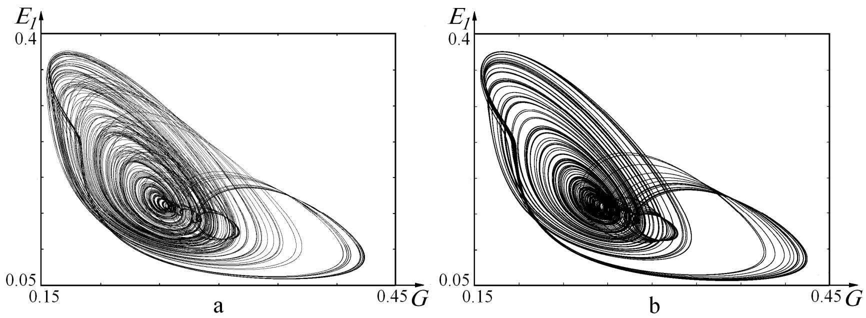

Fig. 7. Projections of the phase portraits: a – strange attractor of the mutual transition $(7\leftrightarrow 14)\cdot 2^x$ for $\alpha = 0.032165$; b – strange attractor $14\cdot 2^x$ for $\alpha = 0.032174$.

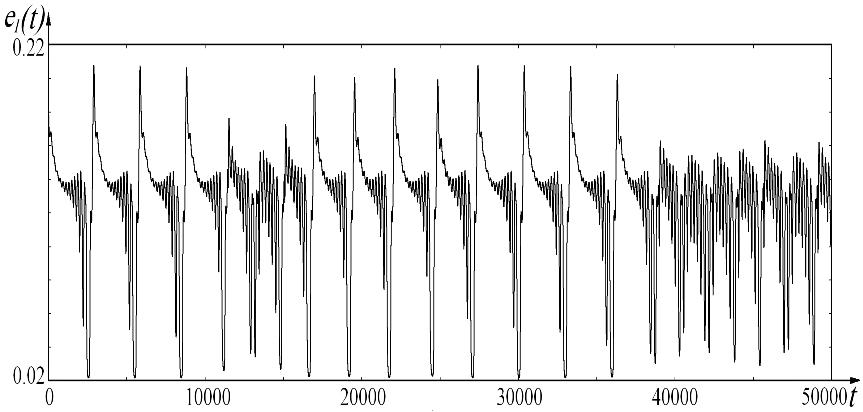

Fig. 8. Kinetic curve of the variable $e_1(t)$ of the mutual transition of the strange attractors $(7 \leftrightarrow 14) \cdot 2^x$ for $\alpha = 0.032165$.

For the given strange attractor, we constructed a projection of the section by the plane $P = 0.2$ and the Poincaré map in Fig. 9,a,b. The choice of a cutting surface was made to attain the maximum number of intersections of the given component and the phase trajectory $P(t)$, as the former decreases, without contacts.

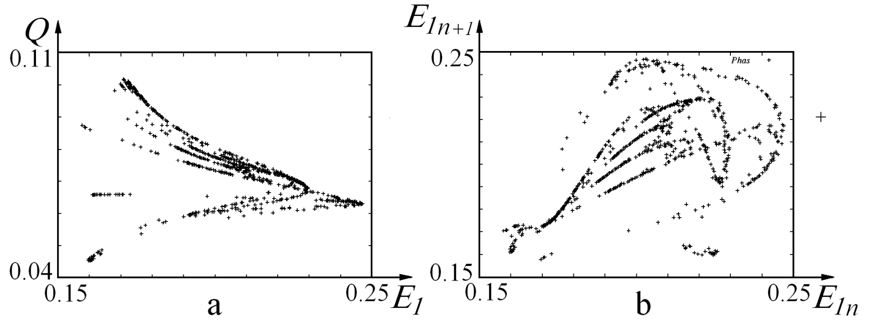

Fig. 9. Projection of the section by the plane $P = 0.2$ (a) and Poincaré map (b) of the strange attractor formed during the mutual transition $(7 \leftrightarrow 14) \cdot 2^x$ for $\alpha = 0.032165$.

The obtained points of intersections and the Poincaré maps are grouped along several curves that form a geometric self-similarity. On the projection, we see clearly the fractality of this strange attractor. In addition, these curves do not create a quasistrip structure. Their number increases permanently with the duration of numerical integration of the system. This testifies to the impossibility of any reduction of the given complicated mathematical model to some one-dimensional discrete approximation without loss of the information about the dynamics of the metabolic process in a cell. We note that the general scheme (Fig. 2) includes only the main parts of the metabolic process running in any cell with substrate-enzyme reactions and in the respiratory chain. Therefore, the model gives a rather general qualitative representation of the dynamics of the internal self-organization of the metabolic process in a cell.

Table 1. Total spectra of Lyapunov indices for attractors of the system under study (λ_4 - λ_{10} are not important for our investigation).

α	Attractor	λ_1	λ_2	λ_3	Λ
0.0321590	$14 \cdot 2^0$	.000056	-.000214	-.003250	-.898509
0.0321596	$14 \cdot 2^0$	.000040	-.000142	-.003306	-.898550
0.03215961	$14 \cdot 2^1$	.000078	-.000150	-.003394	-.899865
0.03215962	$\approx n \cdot 2^0 (t)$	.000063	.000026	-.000274	-.905553
0.032160	$14 \cdot 2^0$	.000040	-.000146	-.003365	-.899368
0.032161	$29 \cdot 2^0$	.000051	-.000142	-.000123	-.905352
0.0321615	$7 \cdot 2^0$	.000062	-.000596	-.000576	-.902277
0.032162	$36 \cdot 2^0$	.000064	-.000171	-.000155	-.905320
0.0321626	$7 \cdot 2^0 (t)$	.000063	-.000097	-.001180	-.902078
0.03216276	$7 \cdot 2^1 (t)$	.000062	-.000005	-.001267	-.902189
0.03216346	$7 \cdot 2^2 (t)$	.000047	.000025	-.001252	-.902056
0.03216361	$7 \cdot 2^3 (t)$	.000048	-.000023	-.001265	-.902267
0.032164	$7 \cdot 2^x$	.000367	.000018	-.001641	-.902164
0.032165	$(7 \leftrightarrow 14) \cdot 2^x$	.000363	-.000004	-.001598	-.904005
0.032174	$14 \cdot 2^x$	.000693	.000020	-.003534	-.901422

4. Conclusions

We have constructed a mathematical model of the metabolic process in a cell *Arthrobacter globiformis* at the transformation of steroids. With the help of the given model, we have found the autooscillations in agreement with experiment, which show the complicated internal dynamics in a cell. The model is optimized by the number of variables of the system required for a qualitative description of the metabolic process under study. The given model involves the general regularities characteristic of any cell consuming a substrate, on the whole. The autooscillations arise on the level of the substrate-enzyme interaction with participation of the redox process in the respiratory chain and characterize the times of such interactions. At the synchronization of the given processes, the autooscillations characterizing the self-organization of the metabolic process on the whole are observed. At the desynchronization of the given processes, we see the adaptation of the metabolic process in a cell to varying external conditions in the environment with conservation of its functionality. The scenario of the transitions "order-chaos", "chaos-order", "order-order", and "chaos-chaos" is studied with the help of Poincaré sections and maps. The total spectra of Lyapunov indices are calculated, and the structural stability of the obtained attractors is studied. Feigenbaum's scenario and the Neimark bifurcation are found. The results will allow one to carry on the search for metabolic oscillations in a cell and to clarify the physical laws of self-organization.

References

1. A. A. Akhrem and Yu. A. Titov. *Steroids and Microorganisms*, Nauka, Moscow, 1970 (in Russian).
2. V. P. Gachok and V. I. Grytsay. Kinetic model of macroporous granule with the regulation of biochemical processes. *Dokl. Akad. Nauk SSSR* 282: 51-53, 1985.
3. V. P. Gachok, V. I. Grytsay, A. Yu. Arinbasarova, A. G. Medentsev, K. A. Koshcheyenko and V. K. Akimenko. Kinetic Model of Hydrocortisone 1-en Dehydrogenation by *Arthrobacter globiformis*. *Biotechn. Bioengin.* 33: 661-667, 1989.
4. V. P. Gachok, V. I. Grytsay, A. Yu. Arinbasarova, A. G. Medentsev, K. A. Koshcheyenko and V. K. Akimenko. A kinetic model for regulation of redox reactions in steroid transformation by *Arthrobacter globiformis* cells. *Biotechn. Bioengin.* 33: 668-680, 1989.
5. V. I. Grytsay. Self-organization in the macroporous structure of the gel with immobilized cells. Kinetic model of bioselective membrane of biosensor. *Dopov. Nats. Akad. Nauk Ukr.* No 2: 175-179, 2000.
6. V. I. Grytsay. Self-organization in a reaction-diffusion porous media. *Dopov. Nats. Akad. Nauk Ukr.* No. 3: 201-206, 2000.
7. V. I. Grytsay. Ordered structure in a mathematical model biosensor. *Dopov. Nats. Akad. Nauk Ukr.* No. 11: 112–116, 2000.
8. V. I. Grytsay. Self-organization of biochemical process of immobilized cells bioselective of membrane biosensor. *Ukr. J. Phys.* 46: 124-127, 2001.
9. V. V. Andreev and V. I. Grytsay. Modeling of inactive zones in porous granules of a catalyst and in a biosensor. *Matem. Modelir.* 17**,** no. 2: 57-64, 2005.
10. V. V. Andreev and V. I. Grytsay. Influence of heterogeneity of diffusion-reaction process for the formation of structures in the porous medium. *Matem. Modelir.* 17, no. 6: 3-12, 2005.
11. V. I. Grytsay and V. V. Andreev. The role of diffusion in the active structures formation in porous reaction-diffusion media. *Matem. Modelir.* 18, no. 12: 88-94, 2006.
12. V. I. Grytsay. Unsteady Conditions in Porous Reaction-Diffusion. *Roman. J. Biophys.* 17, no. 1: 55-62, 2007.
13. V. I. Grytsay. The uncertainty in the evolution structure of reaction-diffusion medium bioreactor. *Biofiz. Visn.* No.2: 92-97, 2007
14. V. I. Grytsay. Formation and stability of morphogenetic fields of immobilized cell in bioreactor. *Biofiz. Visn.* No. 2: 25-34, 2008.
15. V. I. Grytsay. Structural instability of a biochemical process. *Ukr. J. Phys.* 55: 599-606, 2010.
16. V. I. Grytsay and I. V. Musatenko. Self-oscillatory dynamics of the metabolic process in a cell. *Ukr. Biochem. J.* 85, no. 2: 93 – 104, 2013.

17. *V. I. Grytsay and I. V. Musatenko*. The structure of a chaos of strange attractors within a mathematical model of the metabolism of a cell. *Ukr. J. Phys.* 58: 677-686, 2013.
18. A. G. Dorofeev, M. V. Glagolev, T. F. Bondarenko and N. S. Panikov. Unusual growth kinetics of *Arthrobacter globiformis* and its explanation. *Mikrobiol.* 61**,** no. 1: 33-42, 1992.
19. A. S. Skichko and E. M. Koltsova. A mathematical model to describe the fluctuations biomass of bacteria. *Teor. Osnov. Khim. Tekhn.* 40, no. 5: 540-550, 2006.
20. E. E. Selkov. Self-oscillations in glycolysis. *Europ. J. Biochem.* 4: 79-86, 1968.
21. B. Hess and A. Boiteux. Oscillatory phenomena in biochemistry. *Ann. Rev. Biochem***.** 40: 237-258, 1971.
22. A. Goldbeter and R. Lefer. Dissipative structures for an allosteric model. Application to glycolytic oscillations. *Biophys J.* 12: 1302-1315, 1972.
23. A. Godlbeter and R. Caplan. Oscillatory enzymes. *Ann. Rev. Biophys. Bioeng.* 5: 449–476, 1976.
24. *Chaos in Chemical and Biochemical Systems*. Field R., Györgyi L. (eds.), World Scientific, Singapore, 1993.
25. V. S. Anishchenko. *Complex Oscillations in Simple Systems*, Nauka, Moscow, 1990 (in Russian).
26. S. P. Kuznetsov, *Dynamical Chaos*, Nauka, Moscow, 2001 (in Russian).
27. T. S. Krasnopol'skaya and A. Yu. Shvets, *Regular and Chaotic Dynamics of Systems with Bounded Excitation*, R&C Dynamics, Moscow-Izhevsk, 2008 (in Russian).
28. I. Shimada and T. Nagashima. *Progr. Theor. Phys*. 61: 1605-1616, 1979.
29. M. Holodniok, A. Klic, M. Kubicek, M. Marek. *Methods of Analysis of Nonlinear Dynamical Models*, Academia, Praha, 1986. (in Czech).

A Supervisory Fuzzy System for Improving Temperature Control in an Industrial Gas Processing Unit

H. Habbi, N. Bekhadda and M. Kidouche

Applied Automation Laboratory, University of Boumerdès
Av. de l'indépendance 35000 Boumerdès, Algeria
E-mail: habbi_hacene@hotmail.com

Abstract: In this paper, a supervisory control system based on fuzzy reasoning is designed for a real gas processing unit. The system controls the gas temperature flowing through an industrial heat exchanger which is the main component of the unit. The design procedure aims at improving the performance of the existing conventional temperature control system by providing instantaneous monitoring of the control loop through auto-tuning of PID parameters. To show the performance of the designed system, simulations under different situations are performed and some implementation issues on DCS system are given.
Keywords: Supervision, Control loop, Fuzzy reasoning, Gas processing unit.

1. Introduction

In most industrial applications, physical plants usually operate under conventional regulatory strategies based on the common proportional-integral-differential (PID) controllers in order to minimize costs of real implementation, maintenance, operator's training, etc. Operator's experience with this type of controllers plays a substantial role while choosing the control strategy to be implemented for a particular application. Indeed, this issue is one of the main reasons for which control loops in highly sensitive processes such as chemical, petrochemical and nuclear industries are rather equipped with conventional PID controllers instead of more sophisticated strategies [8]. However, PID controllers usually show decreasing performance under varying operating conditions and system nonlinearities [1,6,7]. Manual tuning of PID parameters is usually performed to cope with some critical situations. However, this heuristic procedure does not take into account the required level of operational performance.
More advanced control mechanisms, like intelligent control, adaptive control or predictive control show considerable improvements, especially for processes operating under severe disturbances and over wide-range zones. Many works in the literature reported interesting theoretical and experimental results of intelligent control techniques showing for some application studies their robustness with respect to process and environmental variations, even in the absence of systematic design methodologies [9]. Intelligent paradigms can be integrated to the process control level and/or the supervisory level depending on the application of concern [1,4]. Supervisory control aims at making conventional PID controllers more flexible through auto-tuning so that optimal

or near optimal parameters can be found to meet some predefined stringent control requirements.

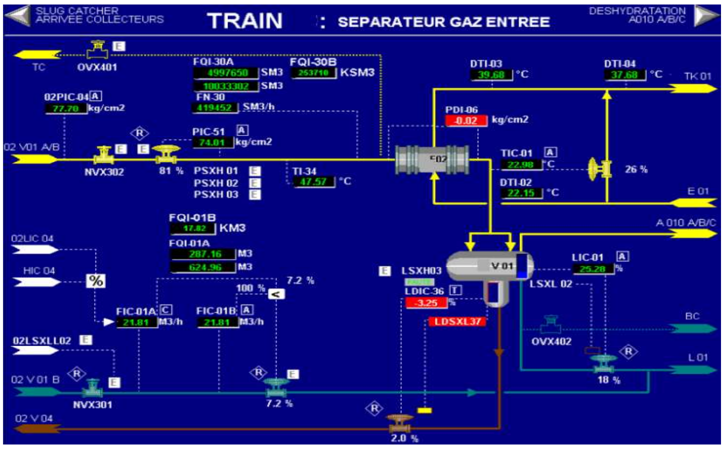

Fig. 1. Schematic picture of the heat exchanger 20E02 in chain 20.

This paper discusses some experimental issues related to the design of a fuzzy supervisory system to improve temperature control performance of an industrial gas processing unit. More precisely, the design procedure is achieved for an industrial co-current heat exchanger aiming at tuning the PID parameters of the gas temperature control loop based on fuzzy reasoning. The present study was subjected to a simulation-based evaluation on DCS (Distributed Control System) using the real parameters of the gas processing unit together with the on-site parameters of the temperature control loop.

2. Industrial Process Description

Natural gas feeding the industrial processing unit arrives from different production sites through twelve collectors at 84 kg/cm^2 and 50°C. The main task consists in achieving total condensate recovery, and gas compression and recycling to other units. To this end, five processing chains labeled as 10 to 40 and 70 are installed. Each chain is composed of two parts: the high-pressure (HP) part for the treatment of gaz-liquid phase, and the low-pressure (LP) part for unstable condensate processing. The crude gas passes first via the slugcatcher unit, and after flowing through different pipes, it is supplied to a co-current type heat exchanger for cooling, and then evacuated with temperature 22°C to a triphasic separator for separation purposes.

In this paper, the heat exchanger under investigation is labeled as 20E02 as depicted in the schematic picture of Figure 1. This physical plant of 16.5 m height and 1418 tubes is one of the most important and critical component of the gas processing unit. The crude gas entering the exchanger is cooled through a heat exchange process with cold gas coming from the gas/gas primary exchanger 20E01. The outlet temperature is controlled at 22°C with a conventional PID controller and must be maintained around this value in order to meet the stringent separation process requirements and keep safe the chain equipments.

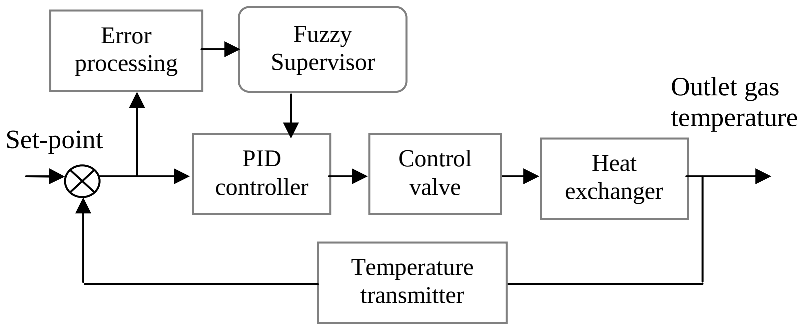

Fig. 2. Block diagram of the fuzzy supervisory gas temperature control system.

3. Design of the Fuzzy Supervisor

All of control loops in the gas treatment unit are based on conventional PID controllers. The temperature control loop of the heat exchanger 20E02 is designed to ensure regulatory task about 22°C of the outlet gas temperature. This value is to be maintained to ensure good separation between gas, water and condensate in the high-pressure triphasic separator 20V01. Efficient separation process should be achieved in order to avoid the formation of hydrates in the corresponding chain which could occur at 18°C and 77 kg/cm^2. Alarm generating devices are installed to prevent reaching 19°C limit value. Obviously, it can be noticed that ensuring suitable operation of the whole unit depends strongly on the “perfect” functioning of the gas temperature control loops. This issue remains of substantial interest for the systems engineers.

From a modeling viewpoint, heat exchanger dynamics are difficult to capture accurately by simple model structures since the underlying physical effects are quite complex and a number of real parameters are unknown. Key dynamical properties of the heat exchange process are generally described by distributed-parameter models that are of little interest for control purposes [5]. Approximations through lumped-parameter models are usually used for dynamics analysis and control systems design. However, the simplified models upon which PID control strategies are built could not ensure a robust wide-range operation [2,3]. Indeed, it was easy to notice that in many practical situations, PID parameters need to be tuned manually to avoid performance degradation during gas processing unit operation. This heuristic tuning procedure which is applied with conventional operators’ experience methods cannot give optimal PID parameters for the gas temperature control system.

The fuzzy supervisory system designed in this paper aims at improving the performance of the conventional gas temperature control loop through auto-tuning of the PID parameters. The three PID parameters, *i.e.* K_p, K_i and K_d can be altered based on a fuzzy reasoning mechanism according to the size, the direction and the changing tendency of the system error. The diagram of the fuzzy supervisory PID control system is depicted in Figure 2. For the heat exchanger operation, control error e and the change of error Δe are the input linguistic variables of the fuzzy supervisor, and ΔK_p, ΔK_i and ΔK_d are their output linguistic variables. Each linguistic variable has seven values labeled as NB, NM, NS, ZO, PS, PM and PB. These triangular-shaped fuzzy sets are uniformly distributed on the common normalized universe of discourse [-1 1]. The fuzzy supervisor is a rule-based system composed of a set of n IF-THEN rules as follows:

$$IF\ e(k)\ is\ LE^j\ and\ \Delta e(k) is\ L\Delta E^j\ THEN$$
$$\Delta K_p(k)\ is\ LK_p^j\ and\ \Delta K_i(k)\ is\ LK_i^j\ and\ \Delta K_d(k)\ is\ LK_d^j$$
$$j = 1, \cdots, n,$$

where $LE^j,\ L\Delta E^j,\ LK_p^j,\ LK_i^j\ and\ LK_d^j$ represent the *j*-th linguistic values of the input/output fuzzy variables *e*, Δe, ΔK_p, ΔK_i and ΔK_d, respectively. The PID tuning mechanism is performed instantaneously according to the following equations [1]:

$$K_p = K_{p0} + \Delta K_p$$
$$K_i = K_{i0} + \Delta K_i$$
$$K_d = K_{d0} + \Delta K_d,$$

where K_{p0}, K_{i0} and K_{d0} denote the actual (on-site) PID parameters. The PID parameters tuning procedure based on this fuzzy reasoning mechanism defines a nonlinear mapping between the fuzzy supervisor outputs, and the control error and its rate of change.

4. Results and Discussion

The original conventional temperature control configuration of the gas treatment unit is implemented on DCS which offer many facilities allowing systems analysis, simulation and control through its IEE (Infusion Engineering Environment) software. The results presented in this paper are based on the physical parameters of the industrial heat exchanger and the on-site parameters of the PID control loop which are set as $K_{p0} = 2.5$, $K_{i0} = 1.11$ and $K_{d0} = 0.38$. The fuzzy supervisor blocks are embedded in DCS according to the diagram shown in Figure 3. The control parameters K_p, K_i and K_d of the real

PID controller are tuned off-line under different situations in order to check the effectiveness of the designed self-tuning mechanism.

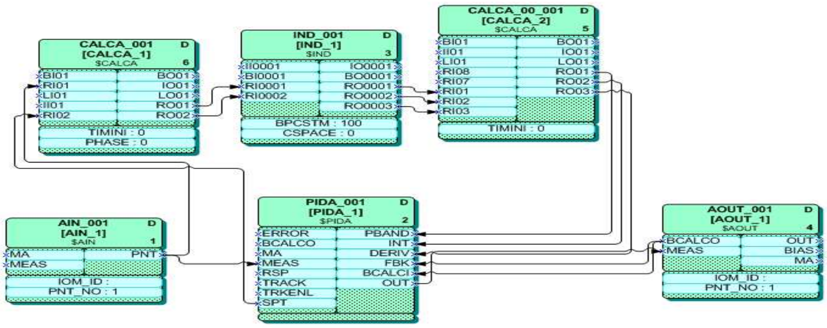

Fig. 3. Configuration of the fuzzy supervisory gas temperature control system on DCS.

Figure 4 shows the outlet gas temperature response in normal regulatory operation. This situation corresponds to inlet gas cooling process before evacuation to the HP triphasic separator. Here the gas temperature is decreased from 50°C (slugcatcher outlet gas temperature) to 22°C. It can be clearly seen that the fuzzy supervisor performs considerably well, mainly after applying an input disturbance on the control valve at t = 10 hrs. The PID controller induces an oscillatory response which is efficiently damped by the fuzzy supervisor through auto-tuning of the PID parameters.

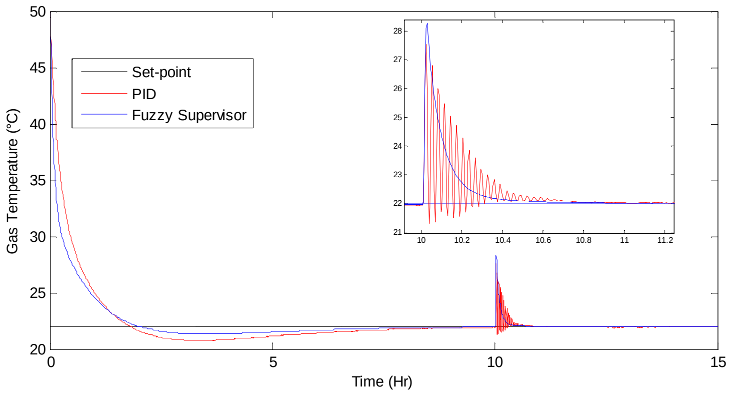

Fig. 4. Outlet gas temperature response in normal operation.

Degradation of the control loop performance is mostly caused by parameter variations of the controlled heat exchanger due to aging, thermal stress or environmental changes, for instance. To illustrate this situation, we considered a test case corresponding to parametric variation of the heat transfer coefficient. This physical parameter is generally unknown and difficult to obtain through first-principle modeling; it can only be estimated using observation data. In this case study, Figure 5 shows clearly the poor performance of the PID control loop. The gas temperature response fluctuates around non-admissible values that would contribute to the formation of hydrates in the chain. In this case, an alarm would occur while the temperature reaches the limit of 19°C. However, the heat exchanger operation under the supervisory control system seems very acceptable and the regulatory requirement is achieved efficiently. This demonstrates the robustness of the fuzzy control system with respect to the system parameter variations which are frequent in practice and for which manual tuning is usually operated to prevent plant operation degradation.

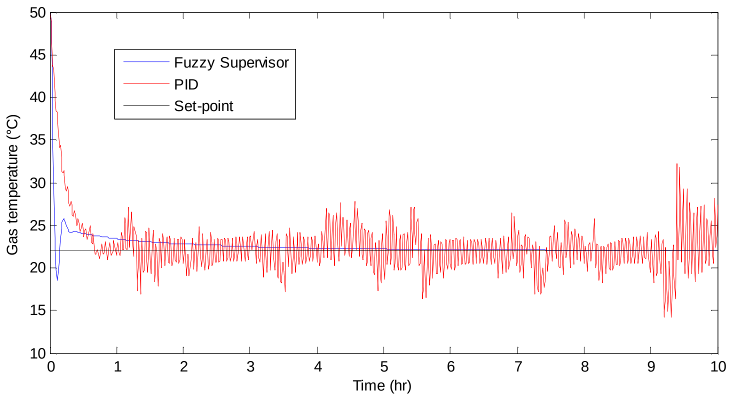

Fig. 5. Outlet gas temperature response under system parameter variations.

5. Conclusions

Throughout this contribution, a simulation-based evaluation on DCS of the performance of a fuzzy supervisory control system is achieved using the real parameters of an industrial gas processing unit together with the on-site parameters of the temperature control loop. Auto-tuning of the PID parameters through fuzzy reasoning improves considerably well the outlet gas temperature control loop performance. This problem is of major interest for systems engineers since the manual tuning of the PID parameters based on operators' experience could not always give satisfactory operational performance. In practical situations, stringent requirements on control strategies are usually imposed to meet production conditions. Embedding intelligent paradigms in conventional control configurations would achieve better results as shown in the present study.

References

1. L. Wang, W. Du, H. Wang and H. Wu. Fuzzy self-tuning PID control of the operation temperatures in a two-staged membrane separation process. *Journal of Natural Gas Chemistry*, no. 17, 409-414, 2008.
2. H. Habbi, M. Kidouche and M. Zelmat. Data-driven fuzzy models for nonlinear identification of a complex heat exchanger. *Applied Mathematical Modelling,* 35(3):1470-1482, 2011.
3. H. Habbi, M. Kidouche, M. Kinnaert and M. Zelmat. Fuzzy model-based fault detection and diagnosis for a pilot heat exchanger. *International Journal of Systems Science*, vol. 42, no. 4, 587-599, 2011.
4. C. Dey and R.K. Mudi. An improved auto-tuning scheme for PID controllers. *ISA Transactions* 48:396-409, 2009.
5. T. Zhang, T. Wen, J. Catano and R. Zhou. Stability analysis of heat exchanger dynamics. *Proceedings of the American Control Conference, St. Louis, MO, USA*, 2009.
6. D. Saez, F. Milla and L.S. Vergas. Fuzzy predictive supervisory control based on genetic algorithms for gas turbines of combined cycle power plants. *IEEE Trans Energy Conversion* 22:689-696, 2007.
7. P.M. Marry and N.S. Marimuthu. Design of self-tuning fuzzy logic controller for the control of an unknown industrial process. *IET Control Theory and Applications* 3:428-436, 2009.
8. W.C. Dunn. *Fundamentals of Industrial Instrumentation and Process Control*, McGraw-Hill, 2005.
9. W. Siler and J.J. Buckley. *Fuzzy Expert Systems and Fuzzy Reasoning*, John Wiley and Sons Inc, 2005.

Proceedings, 6th Chaotic Modeling and Simulation International Conference
11 - 14 June 2013 Istanbul, Turkey

SIGNALS OF CHAOS IN THE TRANSIENT CURRENT THROUGH $As_2S_3(Ag)$ and $As_2Se_3(Al)$ THIN FILMS

A. S. Hacinliyan[1], Y. Skarlatos[2], O. Ozgur Aybar[3], I. Kusbeyzi Aybar[4], E.Kandiran[5], A. C. Keles[6], and E. C. G. Artun[7]

[1] Yeditepe University, Department of Information Systems and Technologies, Istanbul, Turkey
Yeditepe University, Department of Physics, Istanbul, Turkey
Bogazici University, Department of Physics, Istanbul, Turkey
(E-mail: ahacinliyan@yeditepe.edu.tr)
[2] Bogazici University, Department of Physics, Istanbul, Turkey
Yeditepe University, Department of Physics, Istanbul, Turkey
(E-mail: sakarlat@boun.edu.tr)
[3] Gebze Institute of Technology, Department of Mathematics, Kocaeli, Turkey
Yeditepe University, Department of Information Systems and Technologies, Istanbul, Turkey
(E-mail: oaybar@yeditepe.edu.tr)
[4] Yeditepe University, Department of Computer Education and Instructional Technology, Istanbul, Turkey
(E-mail: ikusbeyzi@yeditepe.edu.tr)
[5] Bogazici University, Department of Physics, Istanbul, Turkey
(E-mail: engin.kandiran@boun.edu.tr)
[6] Yeditepe University, Department of Information Systems and Technologies, Istanbul, Turkey
Yeditepe University, Department of Physics, Istanbul, Turkey
(E-mail: ali.keles@yeditepe.edu.tr)
[7] Yeditepe University, Department of Physics, Istanbul, Turkey
(E-mail: ecgartun@hotmail.com)

Abstract: The transient current through a sample of $As_2S_3(Ag)$ and $As_2Se_3(Al)$ glass substrate has been analyzed in order to study possible chaotic behavior using methodology similar to that in work on polymers [1,2]. Rescaled range analysis (R/S) shows the presence of two regimes of fractal behavior, one of which can be attributed to short time scale relaxation and the other can be attributed to long term chaotic behavior. The mutual information data indicates the necessity of noise reduction using a moving average. Extending the moving average window gives correspondingly large delay times as expected. The indicated delay time starts at 20*s* and grows up to 250*s*. The false nearest neighbor results also indicate a value around 10. A robust increase in the Lyapunov exponent stretching graphs confirm long term chaos; the result is not sensitive to the precise values of the delay time and embedding dimension. Possible relaxation mechanisms [3] in the short time range include parametrizations involving stretched exponential relaxation and logarithmic relaxation, the latter suggested by a proposal of Trachenko [4,5].

Keywords: Chaotic Behavior, Lyapunov Exponents, Rescaled Range Analysis.

1. Introduction

The specimens under investigation were prepared as sandwiched metal-glass-metal structures with the glass as the isolating layer. 300 nm thick aluminum electrodes were thermally evaporated at 10^{-6} mbar on microscope glass slides cleaned in a detergent solution. Subsequently, aluminum top contacts were evaporated. The I-V measurement was performed via a programmable picoammeter/voltage source (Keithley, model 487) and a temperature controller (Lake Shore, model 300). The picoammeter and the temperature controller were interfaced to a computer through an interface card that automated data taking, schematically presented in Fig. 1. The picoammeter model 478 used is capable of reading currents in the range 10 fA to 2 mA. It also serves as a DC voltage supply in the range up to 500V.

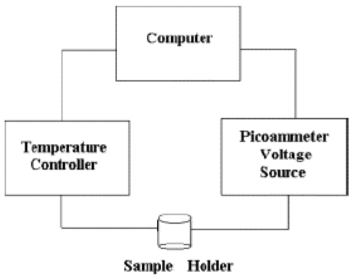

Fig. 1. Schematic of the experimental setup

The data of transient current against time for $As_2S_3(Ag)$ and $As_2Se_3(Al)$ are presented in Fig. 2 and Fig. 3. One horizontal unit represents 30 ms. Examining the graphs, we find that there is an overall relaxation in $As_2Se_3(Al)$ but not in $As_2S_3(Ag)$. However for both materials the data looks more like the behavior of the transient current data for polymer thin films such as PMMA [6] or PEG-Si[2].

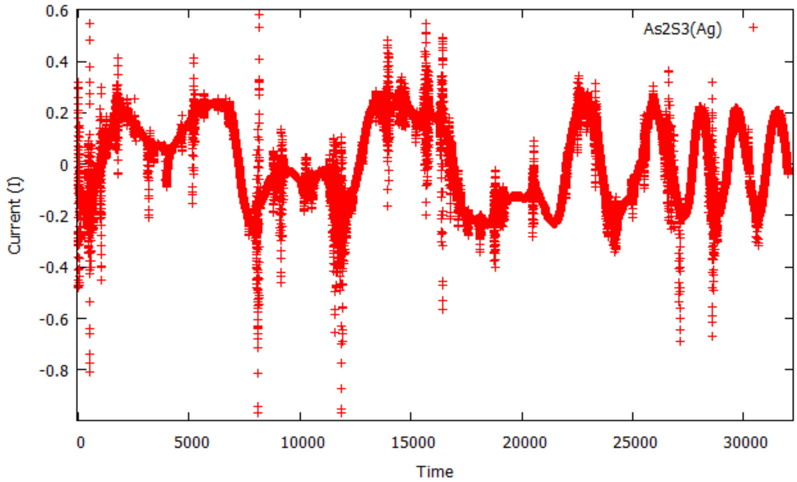

Fig. 2. The data of $As_2S_3(Ag)$

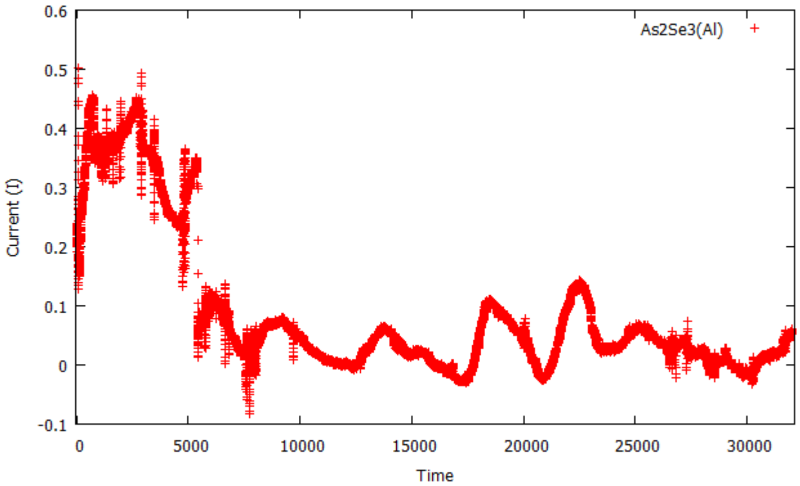

Fig. 3. The data of $As_2Se_3(Al)$

2. Time Series Analysis

Time series analysis is used for analysing the data of $As_2S_3(Ag)$ and $As_2Se_3(Al)$ using TISEAN [7,8] software package. The formulas used are part of the standard literature and are omitted. We observe one dimensional signal in uniform time intervals, x(0), x(T), …, x(nT). In fact the signal x(T) depends on an unknown number of parameters. To determine the number of parameters (dimensionality of the system), we find the meaningful time delay τ and the meaningful embedding dimension to construct time delay vectors. We find the embedding dimension by using the False Nearest Neighbors (FNN) method. We find the delay time by using Mutual Information (MUT) or correlation function (CORR). We calculate the autocorrelation function, which is the Fourier transform of the power spectrum and we present the results in Fig.4.

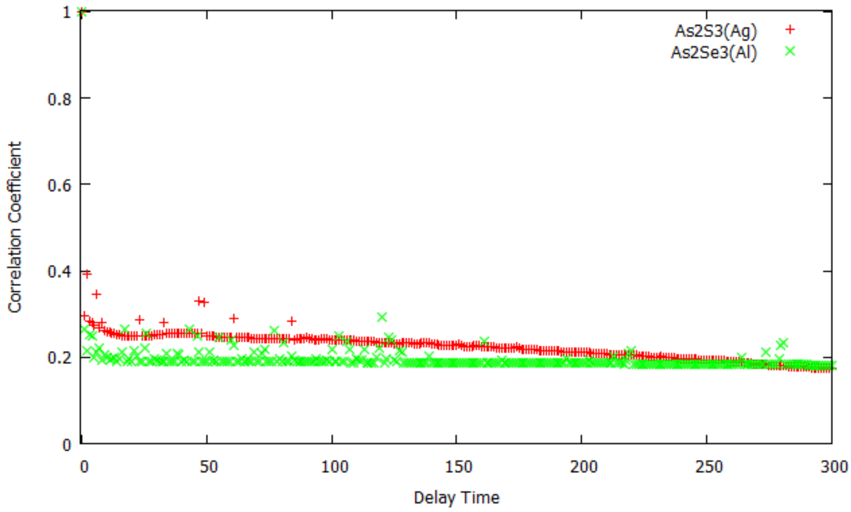

Fig. 4. Correlation coefficient

Another method for obtaining the delay time is to find the first minimum of the mutual information as presented in Fig. 5. We wish to represent a random variable with actual probability distribution p(x) with a code whose average length is H(p). In practice, because of missing information or sampling, we may not know the actual distribution p(x), so that we have to take the distribution to be q(x). In such a situation, we may need a longer code to represent the random variable. This difference in length, D(p(x)||q(x)) is known as the relative entropy. The knowledge that one random variable includes about another random variable is known as mutual information. We can only examine the information that we send to one channel in terms of information output from there. Let x and y be random variables with mutual distribution p(x,y). If variables x and y have distributions p(x) and p(y), the mutual information is the entropy between the mutual distribution and product distribution. If it is chosen to be too small, x(t) and x(t+τ) will be very close to each other and it will be difficult to distinguish them. If it is chosen too large, x(t) and x(t+τ) coordinates will be too far apart, will behave independently and cause loss of information.

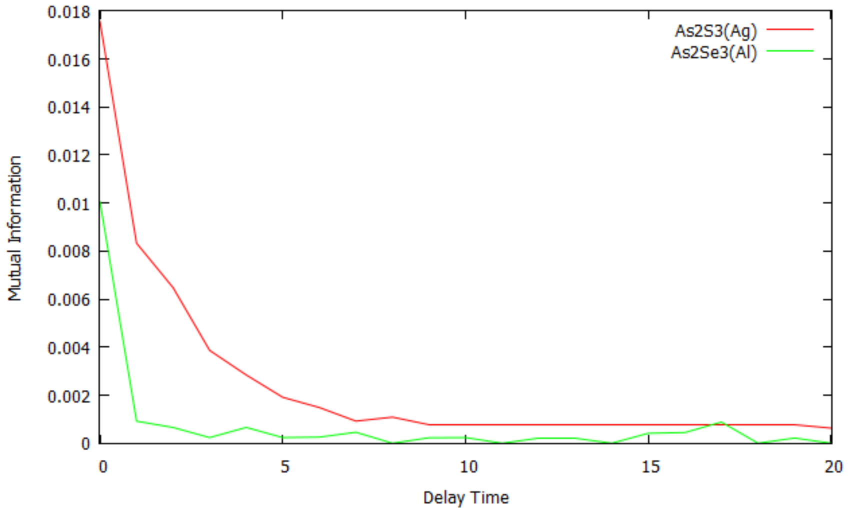

Fig. 5. Mutual information

False nearest neighbors graph (FNN) presented in Fig. 6. is useful for determining the minimal embedding dimension. The purpose is to find points near each other in the embedded space. If the embedding dimension is too small, points that are close in embedded space will appear as false neighbors. If the embedding dimension is too large, we lose statistics and information. By expressing the distance in (d+1) dimensions in terms of the distance in d dimensions, we can calculate the number of neighbors in d and d+1 dimensions, R_{d+1}/R_d . If this ratio is above a critical value, we have false nearest neighbors.

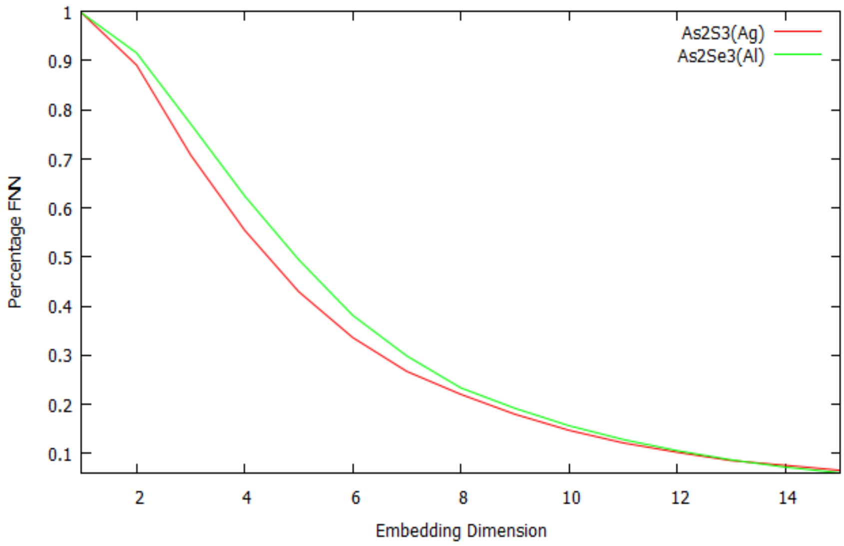

Fig. 6. False nearest neighbors

The largest lyapunov exponent presented in Fig.7 is usually used as an indicator of chaos. This is obtained by calculating the quantity

$$S(\Delta n) = \frac{1}{N}\sum_{n0=1}^{N} \ln\left[\frac{1}{|U(S_{n0})|}\sum_{S_n \in \bigcup(S_{n0})} \left|\left[S_{n0+\Delta n} - S_{n+\Delta n}\right]\right|\right] \qquad (1)$$

S_{n0} is our reference point, U is a hypersphere of distance ε to this point. If ε is too small, we can not find a sufficient number of points, if it is too large, a periodic component may be missed. For a few ε values, calculating the number of points in the hypersphere S(Δn), plotting it against Δn gives the largest Lyapunov Exponent. A positive slope implies a positive Lyapunov Exponent.

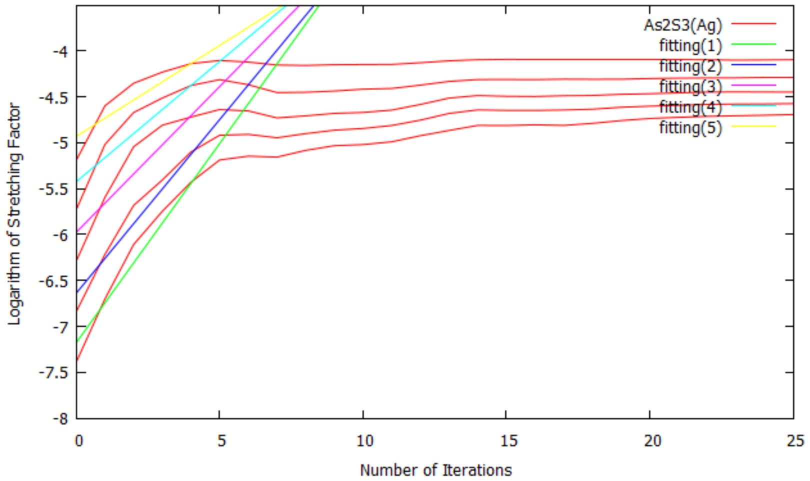

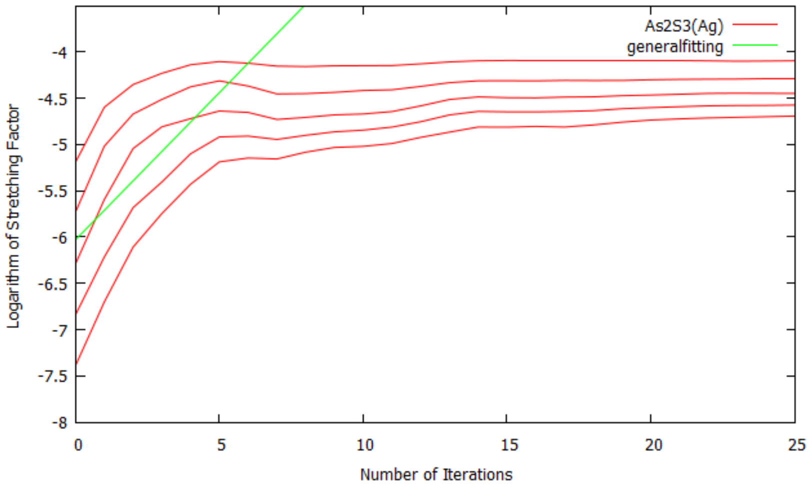

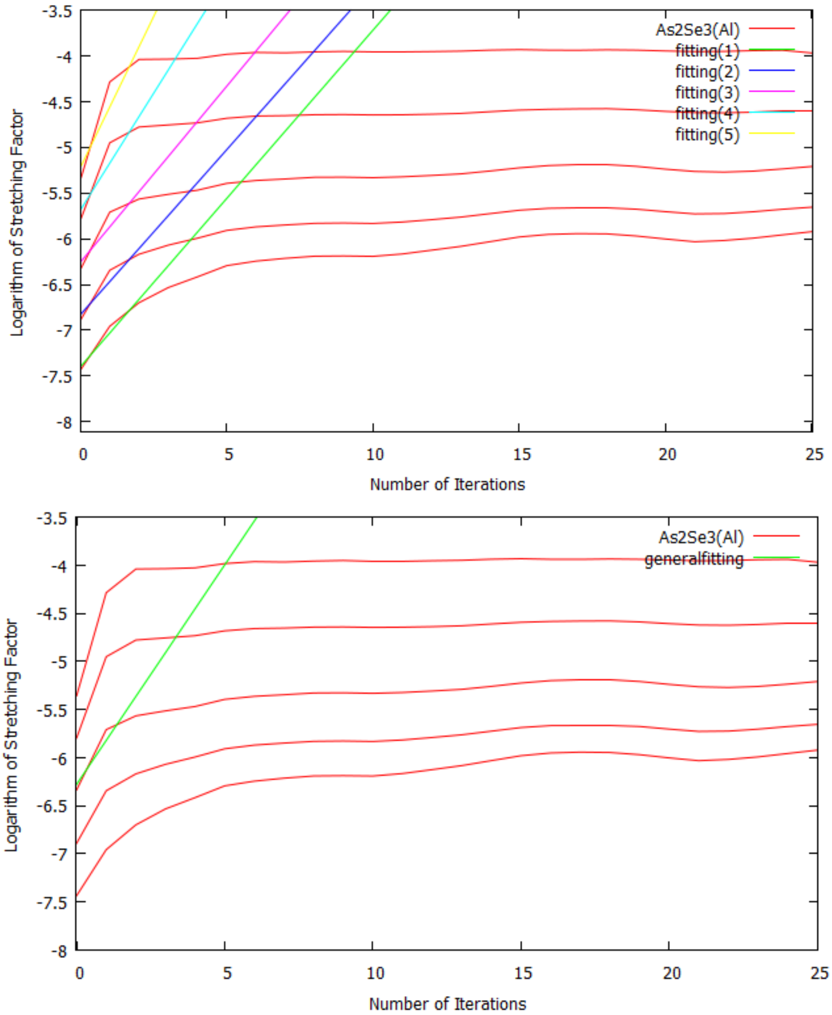

Fig. 7. Largest Lyapunov exponents

Thin Films	Lyapunov Exponent (slope)
$As_2S_3(Ag)$	0.317
$As_2Se_3(Al)$	0.456

3. Hurst (R/S) Analysis

The Hurst exponent is calculated using the standard approach and as presented in Fig. 8 it is a numerical approach to the predictability of a time series. If the Hurst exponent (H) is close to 0.5, the process is a random walk. (Brownian motion) A Hurst exponent (H) in the range $0 < H < 0.5$ implies non random behavior in the time series. A Hurst exponent (H) in the range $0.5 < H < 1$ implies a time series with long range, continuous evolution.

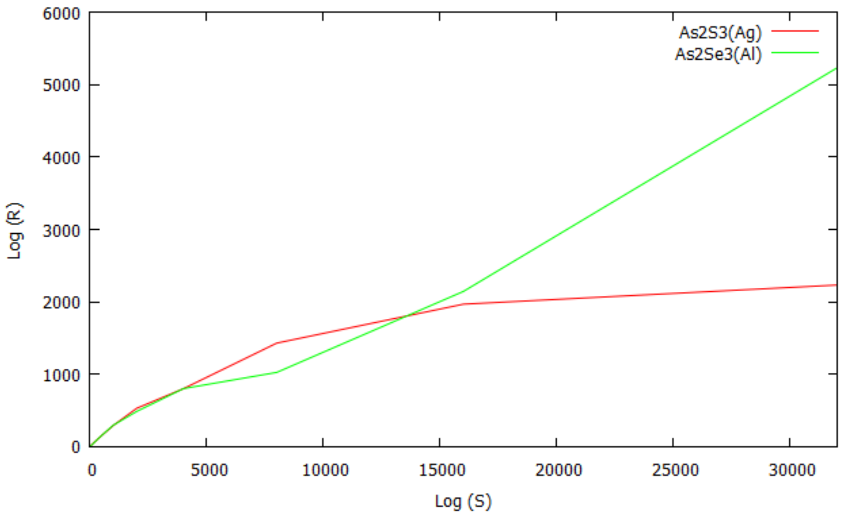

Fig. 8. Hurst Analysis

4. Conclusions

The complex structure of chalcogenites suggests many degrees of freedom and a multi-fractal structure. The transient current through the samples of $As_2S_3(Ag)$ and $As_2Se_3(Al)$ glass substrates has been analyzed in order to study possible chaotic behavior similar to that in our work on polymers. The conductivity mechanism measured by the time dependent behavior of transient current was analyzed by nonlinear considerations such as time series analysis, maximal Lyapunov exponent, Hurst (R/S) analysis. Intermediate dimensional chaos with positive maximal Lyapunov exponents was observed. The behaviors of the system with possibly two different regions, one with short range and another with long range correlation were seen by comparing the correlation coefficient and mutual information. As suggested by studies of other amorphous materials with irregular behavior, the use of nonlinear methods for analyzing the conductivity mechanisms in such materials seems crucial in modelling and show that the behaviors are comparable.

References

1. O. O. Aybar, A. Hacinliyan, Y. Skarlatos, G. Sahin, K. Atak, Possible Stretched Exponential Parametrization for Humidity Absorption in Polymers, *European Physical Journal E* 28: 369-376, 2009.
2. O. O. Aybar, A. Hacinliyan, Y. Skarlatos, G. Sahin, K. Atak, Chaoticity analysis of the current through pure, hydrogenated and hydrophobically modified PEG-Si thin films under varying relative humidity, *Central European Journal of Physics* 7:568-574, 2009.
3. O. Shpotyuk, J. Filipecki, M. Hyla, A. Ingram, Critical comments on speculations with open and closed free-volume defects in ion-conducting Ag/AgI - As_2S_3 glasses, *Solid States Ionics* 208: 1-3, 2012.
4. K. Trachenko, Slow dynamics and stress relaxation in a liquid as an elastic medium, *Physical Review B* 75, 2007.
5. K. Trachenko, Local events and stretched-exponential relaxation in glasses, *Physical Review B* 70, 2004
6. Y. Skarlatos, G. Şahin and G. Akın "Signals of Chaotic Behavior in PMMA" Chaos Solitons and Fractals, 17, 575-583(2003).
7. R. Hegger, H. Kantz, T. Schreiber, Chaos 94, 413 (1999).
8. Kantz, H.and T.Schreiber, Nonlinear Time Series Anaylsis, Cambridge University Press, Cambridge, 1997.

Blind Channel Equalization of Single Input Single Output Chaotic Communication System Using Stochastic Gradient Algorithms

Bassam A. Harb

Yarmouk University, Irbid,Jordan
E-mail: bharb64@gmail.com

Al-Obiedollah M. Haitham
The Hashemite University,Zarqa,Jordan
E-mail: eng.haitham83@yahoo.com

Abstract: The Quadrature Chaotic Shift Keying (QCSK) is one of the widely used chaotic modulation schemes in the chaotic communication systems. Extensive research has been done to study the performance of the QCSK systems. However, the QCSK systems were analyzed with the presence of only additive white Gaussian noise (AWGN) while the effect of the channel has not been considered. In this paper, we study the effects of the channel interference (i.e. AWGN and the channel response) on the modulated signal . The effect of the channel, oblige us to make an equalization process before the detection criteria. The blind equalization process will be implemented using the stochastic gradient algorithm, namely, the LMS algorithm. The performance of the proposed process will be measured based on the Bit Error Rate (BER).

Keywords: Chaotic Communications, Equalization, Quadrature Chaotic Shift Keying, Gradient Stochastic Algorithms.

1. Introduction

Due to some advantages for chaotic communication systems over the classical communications, digital communication based on chaos widely recommended in the field of digital communications, the major advantages of such systems are the less power consumption and security[2]. Quadrature Chaotic Shift Keying (QCSK) is one of the widely used chaotic modulation schemes in the chaotic communication systems, in this modulation scheme, each two bits are converted into a symbol and then these symbols are modulated (mapped) by chaotic carriers [1] , this process is similar to the Quadrature Amplitude Modulation (QAM) which implemented in the classical communications, the only difference is the chaos carries which are used on the chaotic communications instead of the sinusoids which are used in (QAM) [5].

Extensive research has been done to study the performance of the QCSK systems. However, the QCSK systems were analyzed with the presence of only additive white Gaussian noise (AWGN) [1], which isn't reliable case, while the effect of the channel has not been considered , the performance of such model was simulated and performed.

But it is well known that the full representation of the transmitting channel should contains the (AWGN) and the impulse response of the FIR channel as shown in figure (1) a, if the demodulation performed directly without undo the effect of the FIR channel, the (BER) will considerably be increased, which is the problem. In this paper, the performance of (QCSK) will be considered under effect of (AWGN) and the FIR channel.

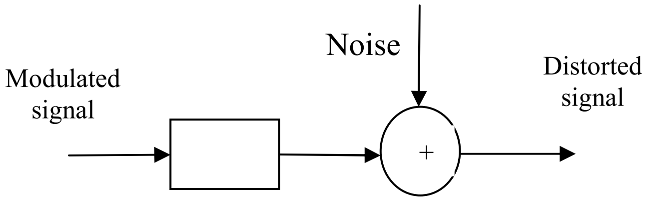

Fig.1.Full Representation of FIR Channel

Where $h[n]$ is the impulse response of FIR channel.

To undo the effect of the FIR channel, the equalization process is required where the equalization should be performed before the demodulation process, it is important to know that the receiver doesn't know the parameters of the channel, so the equalization process has to be blind [3], as the equalizer undo the effect the channel,demodulation process can be performed exactly as (AWGN) case. Adaptive algorithm equalizer; namely Least Mean Square (LMS) will be used to update the equalizer coefficients[6] as it is shown in the following block diagram.

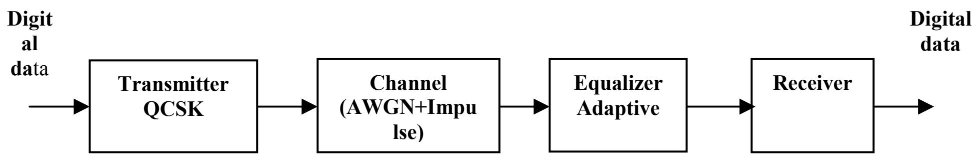

Fig.2 .General Quadrature Chaotic Shift Keying system with equalizer

2. The Model and Simulations

the performance of the QCSK with the presence of the AWGN was analysis and simulated in [1]. The suggested model which is shown in figure 3 seems to be ideal , because it ignores the effect of the transmitted channel.

The modulated signal $S_{QCSK}[n]$ can be expressed as

(1)

Where $c_x[n]$ is is reference chaotic sequence generated from certain map, is orthogonal chaotic to sequence with respect to $c_x[n]$, k is length of chaotic sequence and E_b is the bit energy.

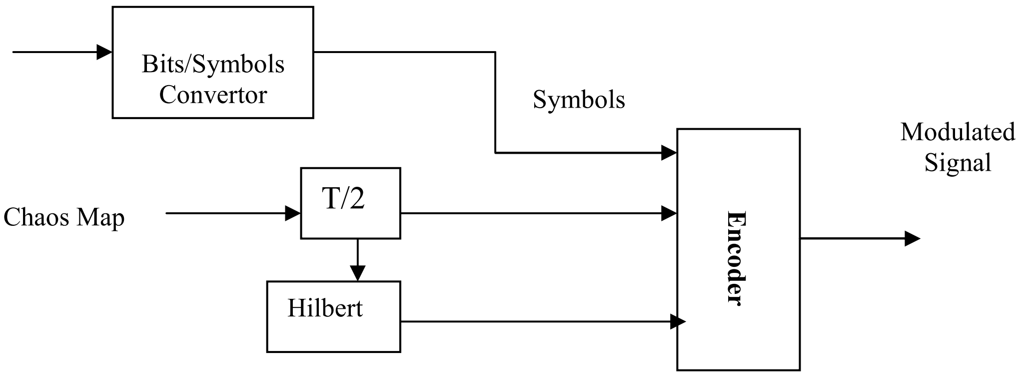

Fig.3. QCSK Modulation

The modulated sequence $s_{QCSK}[n]$ is transmitted through ideal channel ,where the sequence distorted by AWGN , then it will be demodulated using coherent detector[5] and BER of such a case was calculated and simulated.

2.1 Mathematical Model

In the practical case, the channel can't be represented by only AWGN, the full representation shown in figure 1. Is must , if the received distorted sequence demodulated directly , then we will get many bits with error (i.e. , high BER), so it is important to use a filter which undo the effect of the channel which is the Equalizer, in the proposed model of this paper , the stochastic gradient algorithm , namely the Least Mean Square (LMS) , will be used to update the coefficients adaptively[6].

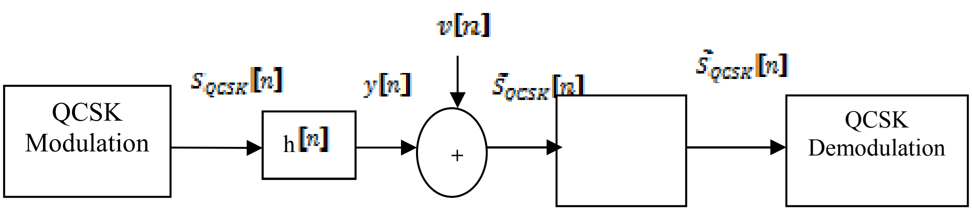

Fig.3. QCSK with equalization

Where is the modulated sequence, is distorted sequence by the channel which expressed in (1), $v[n]$ represents AWGN, and is the equalized version of the distorted sequence , and our target to make the equalized sequence closely matches the original transmitted sequence $S_{QCSK}[n]$. To get the ideal case , which is not reliable, the overall system response $g[n]$, such as $g[n] = h[n] * w[n]$, have to be delta. Mathematically , the equations below describes all what mentioned above,

$$\hat{S}[n] = \sum_{i=0}^{N+M-2} g[i]S[n-i] + \sum_{j=0}^{N-1} w[j]v[n-j] \tag{2}$$

N **is equalizer lenght** , M is channel length and $\sum_{j=0}^{N-1} w[j]v[n-j]$ represent additive colored noise.

The blind equalization can be performed using the Adaptive algorithms, mainly the LMS algorithm [6] , the complete block diagram for such a system is shown in the figure below.

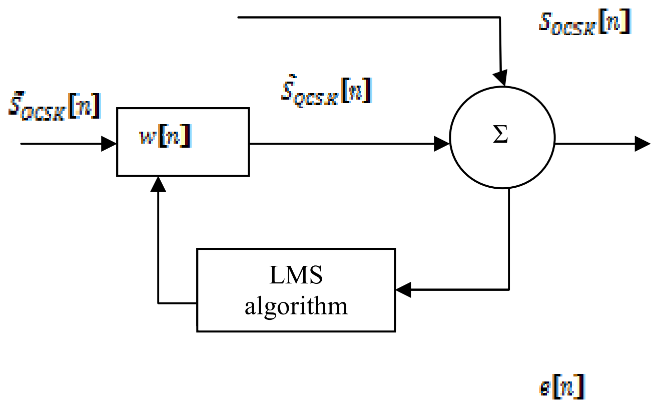

Fig.4. LMS Equalizer

The cost function $j[n]$ which is will be used to minimize the error function will determine the algorithm, in the equalization process proposed in this paper, the LMS algorithm is suggested, so the cost function chosen to update the equalizer coffecirnts can be expressed as

$$j[n] = \frac{1}{(2)(e)^2}$$
(3)

$$j[n] = \frac{1}{(2)(\dot{S}[n] - S[n])^2}$$

(4)

The equalizer coefficients can be rewritten as

$$w_{j+1}(k) = w_j(k) - \mu \frac{dj[n]}{dw_j[k]}$$

(5)

Where μ *is* the step size of the equalizer.

2.2 Simulation Criteria and Results.

The simulation for the system shown above was performed with the consideration of Reney map as reference chaotic sequence, and the bits to be transmitted was (10^5) bits for different FIR channels. Results show that the performance of (QCSK) considerably improved when equalization process implemented ,for example , the BER of channel with impulse response of $[1\ .2\ \ .3]$ found to be $(1\times 10^{(-1)})$ at SNR equals to (14dB) which is very large, while the proposed equalization process can be reduce this value until $(7\times 10^{(-3)})$ at the same SNR which can considered as Significant improvement , taking in account that the ideal system (AWGN only) BER found to be (5×10^{-4}) . Simulations performed also under other FIR channels and algorithm parameters. Figure below shows an example of simulations performed in the paper, where the step size for the algorithm was (0.01).

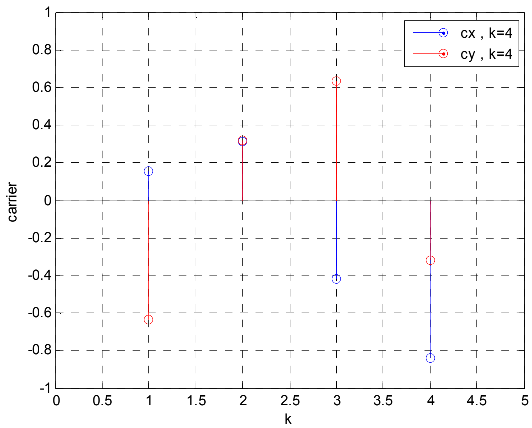

Fig.5. Chaotic Sequence

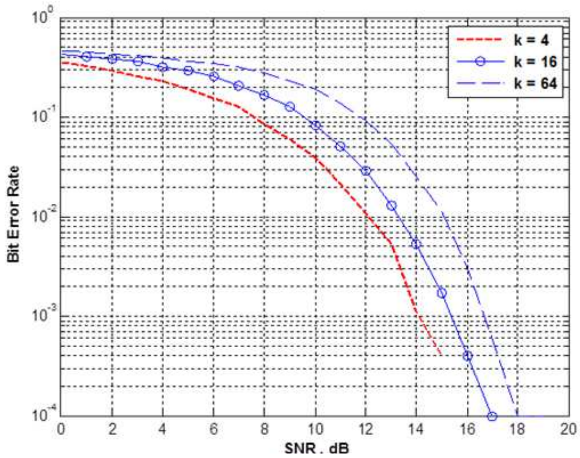

Fig.6. BER of QCSK without Channel Effect

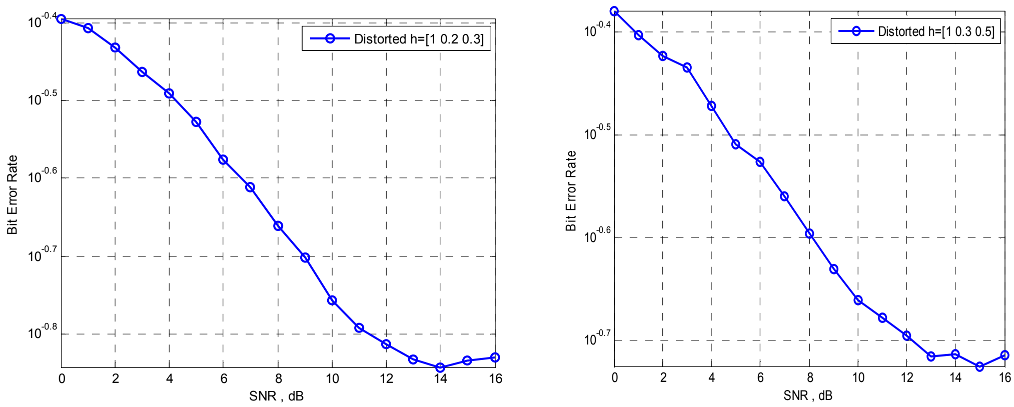

Fig.7. BER of QCSK with different FIR Channels , without equalization

It is noticed from Figure 7. That the BER is considerably high, so the same system will be simulated with the presence of the LMS equalizer, and the simulated results will be shown in following

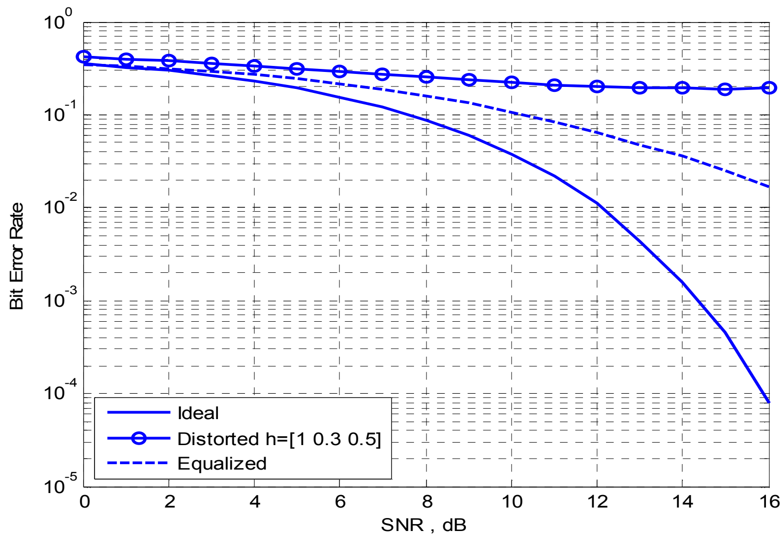

Fig.8. BER of QCSK with FIR channel(k=4,μ=0.01)

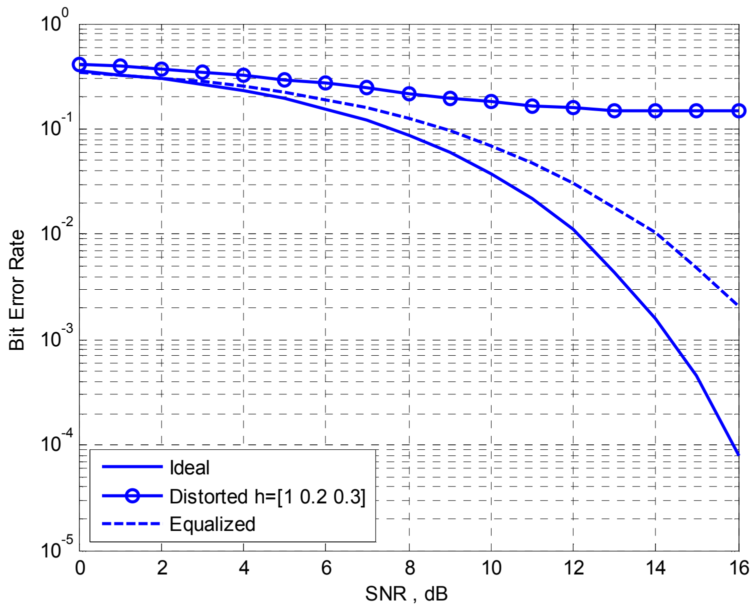

Figure 9 :BER of QCSK with FIR channel(k=4,μ=0.01)

3. Conclusions

This paper discussed the performance of chaotic communication systems when blind equalization performed , the QCSK was taken as example of chaotic modulation and the performance of such a system is simulated , it is found that the use of LMS algorithm improves the performance of chaotic modulation scheme, there is another factor which determines the performance of the QCSK , which is the number of chaotic carrier samples (k) that are used to modulate the incoming bits stream, as the number of samples increase as the BER decrease, however , the (k) is supposed to be large enough in the theoretical part in order to apply the Central Limit Theorem.

The simulation was performed based on four level QCSK constellation, and it can be extended to the second constellation easily, that by changing the coding map and the decision regions criteria.

References

[1]Z.Gallias and G.Mario " *Quadrature Chaos-Shift Keying: Theory and Performance Analysis*", IEEE Trans. Vol.48,no.12,pp. 1510-1519,2001.

[2] G.Kolumban and M.Kennedy " *The Role of Synchronization in Digital Communications Using Chaos –Part I*: Fundemnetals of Digital Communications IEEE Trans , vol.44,no.10, pp927-936,1997

[3] Cabir Vural and Getinel "*Blind equalization of single-input single-output fir channels for chaotic*" Digital Signal Processing 20 (2010) 201–211 communication systems.

[4] M.Cifitic and Doglas " *A novel channel equalizer for chaotic digital communications system*" center for signal and image processing . Atlanta Georgia.

[5] J.G . Proakis, *Digital Communication*. Singapore , McGraw-Hill,1983.

[6] S. Haykin, *Adaptive Filter Theory*, 4th ed., Prentice Hall, Englewood Cliffs, NJ, 2001.

Proceedings, 6th Chaotic Modeling and Simulation International Conference
11 - 14 June 2013 Istanbul, Turkey

Bifurcation Phenomena Observed in an Interrupted Electric Circuit with Two Switches

Yutaka Izumi[1], Hiroyuki Asahara[1], Takuji kousaka[1], and Kazuyuki Aihara[2]

[1] Faculty of Engineering, Oita University, 700 Dannoharu, Oita, Japan
(E-mail: {yutaka, asahara}@bifurcation.jp, takuji@oita-u.ac.jp)
[2] Institute of Industrial Science, The University of Tokyo, 7-3-1, Hongo, Bukyo-ku, Tokyo, Japan
(E-mail: aihara@sat.t.u-tokyo.ac.jp)

Abstract. Although the parallel-connected DC/DC converters have attracted attention in recently, analysis of it is not easy because of its complicity. In this study, we analyze a simple interrupted electric circuit, which has two interrupted switches. First, we show the circuit model and explain its dynamics. Then, we define the sampled data model. Using the sampled data model, we derive the 1- and 2-parameter bifurcation diagrams. Finally, we discuss characteristics of the circuit by comparing the circuit with single interrupted switch.
Keywords: Bifurcation, Interrupted electric circuit, Poincaré map, Stability.

1 Introduction

An electric circuit, which has the switch depending on the state and a periodic interval, has the interrupted characteristics. It is known that the interrupted electric circuit has two or more subsystems. Moreover, the discrete map of the interrupted electric circuit is categorized as the piecewise smooth map. The power conversion circuits, for example converters or inverters, are the typical example of them. There are rich nonlinear dynamics in the power conversion circuits upon varying the circuit parameter [1, 2]. It is important to analyze the nonlinear dynamics in the interrupted electric circuit not only for understanding circuit characteristics but also for the practical application. For this reason, many researchers have analyzed them for the past decades [3–6]. We have also proposed an interrupted electric circuit, which simulates switching dynamics of the frequency mode controlled DC/DC converter, for rigorously analyzing and understanding nonlinear phenomena of the interrupted electric circuit [7].

Circuit's characteristics and its nonlinear behavior of a simple class of the interrupted electric circuit, such as the single buck, boost, or buck-boost converters, have been completely studied in the previous works [8, 9]. But, detailed analysis of the high-dimensional interrupted electric circuit, such as the parallel connected DC/DC converters, resonate converters, and so on, is insufficient and their basic characteristics remains unclear because of the complex circuit dynamics. So, we have proposed the simplest interrupted electric circuit, which has two interrupted switches, for understanding characteristics of the parallel-connected DC/DC converters; both of the proposed model and parallel-connected DC/DC converters have the two interrupted switches, whose switching action is dependent on the state and a periodic interval. Although the circuit has been analyzed in Ref. [10] a little, detailed analysis is insufficient.

In this study, we discuss the characteristics of the circuit with two switches by using the simplest class of the interrupted electric circuit. First, we show the circuit model with two switches and then we explain behavior of the waveform. Next, the waveform is discretized by every period of the clock interval, and the return map is defined. By using the discrete map, we derive the 1-parameter bifurcation diagram and the 2-parameter bifurcation diagram. Moreover, we analyze the bifurcation phenomena in the interrupted electric circuit with two switches. Finally, we discuss how connecting two switches in parallel affects the qualitative property of the system compared with that of a circuit with the single switch based on the numerically analysis.

2 Circuit dynamics

2.1 Circuit model

Figure 1 shows the circuit model. The switch 1 and the switch 2 change from B to A per the clock pulse interval $2T$. Note that the clock pulse of the switch 2 delays a gap T compered with the switch 1. Also, the circuit parameters are follows:

$$R = 10[\mathrm{k}\Omega], C = 0.33[\mu\mathrm{F}], E = 3.0[\mathrm{V}], T = 1.0[\mathrm{ms}] \tag{1}$$

Moreover, the state in the circuit model is classified into four cases as follows:

Case1**:** The switch 1 and the switch 2 are A.
Case2**:** The switch 1 is A and the switch 2 is B.
Case3**:** The switch 1 is B and the switch 2 is A.
Case4**:** The switch 1 and the switch 2 are B.

The circuit equations are defined easily and the solution of them are expressed as follows:

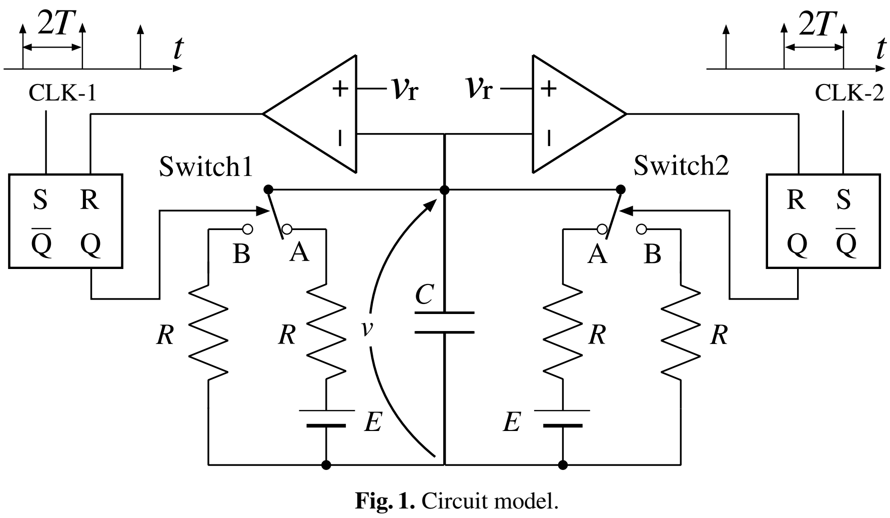

Fig. 1. Circuit model.

$$v(t) = \begin{cases} \varphi_1(t, kT, v_k, \lambda, \lambda_1) \text{ , for state 1} \\ \varphi_2(t, kT, v_k, \lambda, \lambda_2) \text{ , for state 2} \\ \varphi_3(t, kT, v_\mathrm{r}, \lambda, \lambda_3) \text{ , for state 3} \end{cases}, \quad (2)$$

where v_k denotes an initial value at $t = kT$.

2.2 Behavior of the waveform

Figure 2 shows an example of the behavior of the capacitance voltage in the circuit model with two switches. In the following analysis, we call the behavior of the capacitance voltage v as the waveform. When the waveform reaches the reference value v_r, the switch 1 and the switch 2 change from A to B, i.e., the state of the circuit model changes to state 3. After that, if the clock pulse is impressed, the state of the circuit model changes to state 2. Moreover, if the clock pulse is impressed when the state of the circuit model is state 2, the state of the circuit model changes to state 1 again. Note that the clock pulse is ignored if it appears when the switch connects to A. Also, if the state of the circuit model is state 2 when the waveform v reaches the reference value v_r, the state of the circuit model changes to state 1.

3 Discrete map

We sampled the waveform by every period of T for defining the discrete map in the circuit. The waveform during the clock pulse interval T is classified into four types by using the initial value v_k at $t = kT$ and the borders D and D'. The borders D and D' are satisfied following condition:

$$\varphi_1(T, kT, D, \lambda, \lambda_1) = v_\mathrm{r} \quad (3)$$

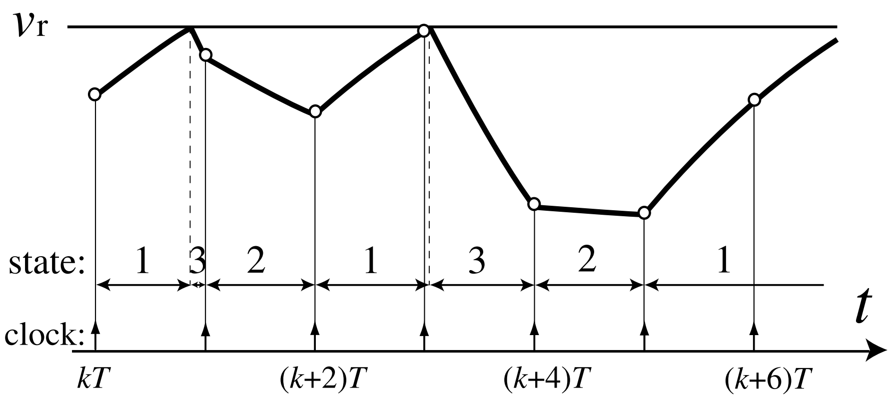

Fig. 2. Waveforms.

$$\varphi_2(T, kT, D', \lambda, \lambda_2) = v_\mathrm{r} \tag{4}$$

The switch keeps state 1 during the clock interval if $v_k \leq D$ is satisfied. Thus, the discrete map M_1 is defined as follows:

$$\begin{aligned} M_1 : \boldsymbol{R} &\to \boldsymbol{R} \\ v_k &\mapsto v_{k+1} = \varphi_1(T, kT, v_k, \lambda, \lambda_1), \end{aligned} \tag{5}$$

where λ_1 denotes a dependency parameter. Also, v_k and v_{k+1} are the solutions at $t = kT$ and $t = (k+1)T$.

The waveform reaches to the reference value v_r at $t = kT + t_\mathrm{A}$ if $v_k > D$ is satisfied. Thus, we define the following map $M_{2\mathrm{A}}$:

$$\begin{aligned} M_{2\mathrm{A}} : \boldsymbol{R} &\to \boldsymbol{\Pi} \\ v_k &\mapsto v_\mathrm{r} = \varphi_1(t_\mathrm{A}, kT, v_k, \lambda, \lambda_1), \end{aligned} \tag{6}$$

where Π denotes the reference value. After that, the waveform reaches to v_{k+1} at $t = (k+1)T$. Therefore, we define the following map $M_{2\mathrm{B}}$:

$$\begin{aligned} M_{2\mathrm{B}} : \boldsymbol{\Pi} &\to \boldsymbol{R} \\ v_\mathrm{r} &\mapsto v_{k+1} = \varphi_3(T - t_\mathrm{A}, kT + t_\mathrm{A}, v_\mathrm{r}, \lambda, \lambda_3), \end{aligned} \tag{7}$$

where λ_3 denotes a dependency parameter. Thus, the discrete map is defined as follows:

$$\begin{aligned} M_2 : \boldsymbol{R} &\to \boldsymbol{R} \\ v_k &\mapsto v_{k+1} = M_{2\mathrm{B}} \circ M_{2\mathrm{A}}. \end{aligned} \tag{8}$$

The switch keeps state 2 during the clock interval if $v_k \leq D'$ is satisfied. Thus, the discrete map M_1' is defined as follows:

$$\begin{aligned} M_1' : \boldsymbol{R} &\to \boldsymbol{R} \\ v_k &\mapsto v_{k+1} = \varphi_2(T, kT, v_k, \lambda, \lambda_2), \end{aligned} \tag{9}$$

where λ_2 denotes a dependency parameter. Also, v_k and v_{k+1} are the solutions at $t = kT$ and $t = (k+1)T$.

The waveform reaches to the reference value v_r at $t = kT + t'_\mathrm{A}$ if $v_k > D'$ is satisfied. Thus, we define the following map $M'_{2\mathrm{A}}$:

$$\begin{aligned} M'_{2\mathrm{A}} : \boldsymbol{R} &\to \boldsymbol{\Pi} \\ v_k &\mapsto v_\mathrm{r} = \varphi_2(t'_\mathrm{A}, kT, v_k, \lambda, \lambda_2). \end{aligned} \tag{10}$$

After that, the waveform reaches to v_{k+1} at $t = (k+1)T$. Therefore, we define the following map $M'_{2\mathrm{B}}$:

$$\begin{aligned} M'_{2\mathrm{B}} : \boldsymbol{\Pi} &\to \boldsymbol{R} \\ v_\mathrm{r} &\mapsto v_{k+1} = \varphi_3(T - t'_\mathrm{A}, kT + t'_\mathrm{A}, v_\mathrm{r}, \lambda, \lambda_3), \end{aligned} \tag{11}$$

Thus, the discrete map is defined as follows:

$$\begin{aligned} M_2' : \boldsymbol{R} &\to \boldsymbol{R} \\ v_k &\mapsto v_{k+1} = M'_{2\mathrm{B}} \circ M'_{2\mathrm{A}}. \end{aligned} \tag{12}$$

By using the discrete maps, we derive the bifurcation diagram and discuss the qualitative property of the circuit in the following analysis.

4 Analytical result

First, we discuss the bifurcation phenomena of the circuit with two switches. Figure 3 shows an example of the 1-parameter bifurcation diagrams upon varying the bifurcation parameter v_r from $v_r = 0.5$[V] to $v_r = 2.0$[V]. Note that we calculate the 1 parameter bifurcation diagram in the circuit with single switch in order to compare with the circuit with two switches. Moreover, Fig. 4 shows the waveforms and the discrete maps, respectively. Here, (a) and (b) in Fig. 4 correspond to the parameters (a) and (b) in Fig. 3. Note that we have numerically calculated Figs. 3 and 4 using Eqs. (5), (8), (9), (12). We observe the bifurcation phenomena in the bifurcation diagram. For example, the period-1 solution bifurcates to the period-2 solution around $v_r = 0.8$[V]. After that the period-2 solution bifurcates to the period-3 solution around $v_r = 1.9$[V]. Moreover, there are the various kinds of the periodic solution and the chaotic attractors in the circuit.

Figure 5 shows examples of the 2-parameter bifurcation diagrams of v_r–T plane. Note that we derive the 2-parameter bifurcation diagram of the single switch case for

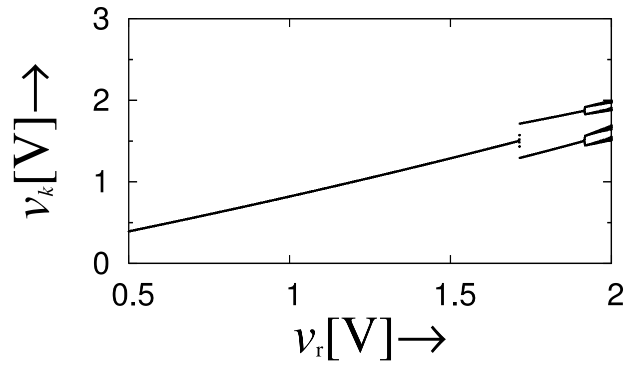

(I) Single switch

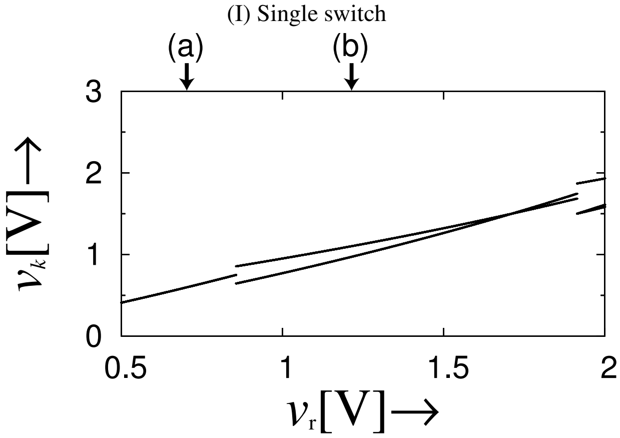

(II) Two switches

Fig. 3. Example of the 1-parameter bifurcation diagram.

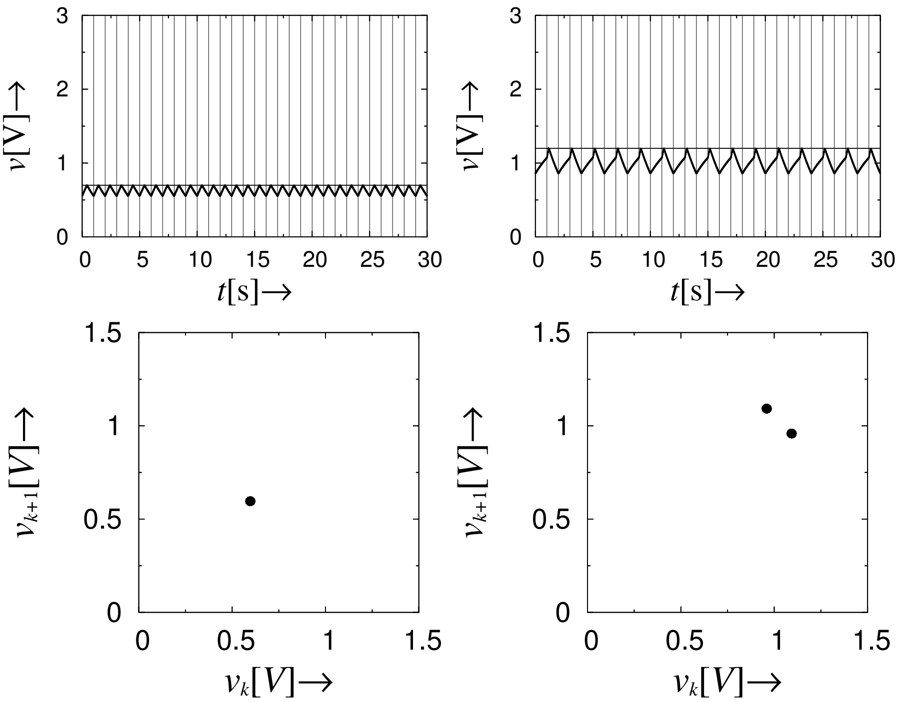

(a) Period-1 solution (v_r = 0.7[V]) (b) Period-2 solution (v_r = 1.2[V])

Fig. 4. Examples of the waveform and the discrete map.

comparing with the circuit with two switches. In this figure, we express the existence region of the period-m solution as mP ($m = 1, 2, 3$). There is the period-doubling bifurcation in the circuit. Here, we only calculate the period-doubling bifurcation in this study. Also, the condition of the period-doubling bifurcation is defined as follows:

$$\left(\frac{dM_1}{dv_k}\right)^{n-2} \frac{dM_2}{dv_k}\frac{dM_1'}{dv_k} + 1 = 0 \qquad (n \geq 2)\,. \tag{13}$$

Note that the condition of the period-1 solution defined as follows:

$$\frac{dM_2'}{dv_k} + 1 = 0\,. \tag{14}$$

The solid lines in Fig. 5 are the bifurcation sets of the period doubling bifurcation.

Tables 1 and 2 show the stability of the period-1 solution in the circuit with single switch and that of with two switches, respectively. Tables say that two interrupted switches make the existence region of the period-1 solution small. This characteristics may be same in the parallel-connected DC/DC converters, because both of the parallel-connected DC/DC converters and our model have the two interrupted switches, whose switching action is dependent on the state and a periodic interval.

5 Conclusion

In this study, we have studied an electric circuit with two switches. First, we showed the circuit model and its behavior. Next, we defined the discrete map and derived the bifurcation diagrams. Finally, we discussed the characteristics the circuit using the bifurcation diagrams. We found that the two interrupted switches makes the existence region of the period-1 solution small. We consider that the same the parallel-connected DC/DC converters has same characteristics. In future, we will clarify the characteristics of the circuit in more detail.

References

1.S. Banerjee, G. C. Verghese, eds., “Nonlinear Phenomena in Power Electronics: Attractors, Bifurcations, Chaos, and Nonlinear Control.” IEEE Press 2001.
2.C. K. Tse, “Complex Behavior of Switching Power Converters.” New York: CRC, 2003.
3.G. Yuan, S. Banerjee, E. Ott, J.A. Yorke, “Border-Collision Bifurcations in the Buck Converter.” IEEE Transaction on Circuits and Systems I, Vol. 45, No. 7, Pp. 707–716, 1998. piecewise linear map
4.A. EI. Aroudi, G. Olivar, L. Benadero, T. Toribio, “Hopf bifurcation and chaos from torus breakdown in a PWM voltage-controlled DC-DC boost converter.” IEEE Transaction on Circuits and Systems I, Vol. 46, Pp. 1374–1382, 1999.
5.T. Kabe, S. Parui, H. Torikai, S. Banerjee, and T. Saito, “Analysis of Piecewise Constant Models of Current Mode Controlled DC-DC Converters.” IEICE TRANS. FUNDAMENTALS, vol.E90-A, no.2, 2007.
6.D. Fournier-Prunaret, P. Charge, L. Gardini, “Border collision bifurcations and chaotic sets in a two-dimensional.” Communications in Nonlinear Science and Numerical Simulation, Vol. 16, No. 2, Pp. 916-927, 2011.
7.T. Kousaka, T. Ueta, S. Tahara and H. Kawakami, “Implementation and Analysis of a Simple Circuit Causing Border-Collision Bifurcation.” IEE Japan, Vol.122-C, No.11, pp.1908–1916, 2002. (In Japanese)

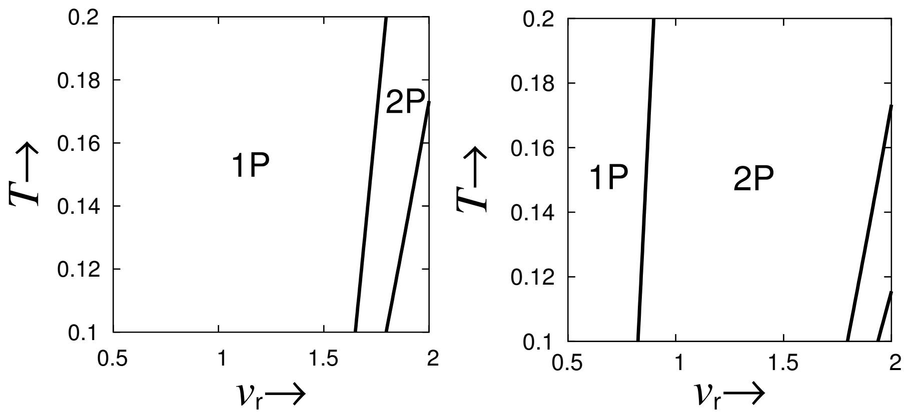

(a) Single switch

(b) Two switches

Fig. 5. Example of the 2-parameter bifurcation diagrams.

Table 1. Stability in the circuit with single switch.

Bifurcation parameter v_r	Characteristicmultiplier	Remark
1.6056	-0.99962	Stable
1.6057	-0.99975	Stable
1.6058	-0.99989	Stable
1.6059	-1.00002	Period doubling bifurcation
1.6060	-1.00016	Unstable
1.6061	-1.00029	Unstable
1.6062	-1.00042	Unstable

Table 2. Stability in the circuit with two switches.

Bifurcation parameter v_r	Characteristicmultiplier	Remark
0.855100	-0.999295	Stable
0.855200	-0.999567	Stable
0.855300	-0.999839	Stable
0.855400	-1.000111	Period doubling bifurcation
0.855500	-1.000383	Unstable
0.855600	-1.000655	Unstable
0.855700	-1.000928	Unstable

8.H. H. C. Iu et al., "Comparative Study of Bifurcation in Single and Parallel-Connected Buck Converters Under Current-Mode Control: Disappearance of Period-Doubling." Circuits Systems Signal Processing Vol. 24, No. 2, 2005, Pp. 201–219.

9.Y. Huang, C.K. Tse, "Circuit theory of paralleling switching converters." International Journal of Circuit Theory and Applications Vol. 37, No. (1), Pp. 109–135, 2009

10.H. Asahara, T. Kousaka, "FUNDAMENTAL CHARACTERISTICS OF AN ELECTRIC CIRCUIT WITH TWO STATE- AND TIME-DEPENDENT INTERRUPTED SWITCHES." Proc. ITC-CSCC 2012, B-T3-01, 2012.

Best Trapezoidal Solution of fuzzy nonlinear equations by metric space

Yousef Jafarzadeh

Sama technical and vocational training college, Islamic Azad University, Karaj Branch, Karaj, Iran
E-mail: Mat2j@yahoo.com

Abstract: Fuzzy logic is powerful tool for modeling uncertainties associated with human cognition, thinking and perception, which has been successfully applied in various fields such as neural network and financial time series. The models are leads to a nonlinear system.
In this paper, we propose a method for finding trapezoidal approximation of solution of fuzzy nonlinear equations using the metric (distance) between two fuzzy numbers. Numerical test is given to state efficiency of the proposed method. The proposed method is compared to Newton's method for a fuzzy nonlinear equation
Keywords: Fuzzy distance- Fuzzy number- Fuzzy nonlinear equation.

1. Introduction

Systems of simultaneous nonlinear equations play a major role in various areas such as mathematics, statistics, engineering and social sciences. The numerical solution of a fuzzy nonlinear equation in general, as $F(x) = C$, by Newton's method was considered in [1- 3].
In this paper, we propose a method for finding trapezoidal approximation of fuzzy nonlinear equations solution using the distance between two fuzzy numbers u, v. The function $D(u, v)$ is a metric in E and (E, D) is a complete metric space.
We use the concept of the trapezoidal fuzzy number, and propose new approach to solving fuzzy nonlinear equations. The basic idea of the new method is to obtain the nearest trapezoidal fuzzy number which is related to a fuzzy quantity. We generalize it for finding trapezoidal approximation solution of fuzzy nonlinear equations.
Recently, there have been many research papers investigating on approximation of fuzzy numbers [4- 6]. In 2001, Chanas [4] have introduced the notion of an approximation interval of a fuzzy number. In 2002, Grzegorzewski [5], have suggested a new approach to interval approximation of fuzzy numbers.
There have been many papers investigating triangular and trapezoidal approximation of fuzzy numbers [7-12]. In 2000, Ma et. al. [7] have used the concept of the symmetric triangular fuzzy number, and they have introduced a new method to defuzzy a general fuzzy quantity. The basic idea of their method was obtaining the nearest symmetric triangular fuzzy number for each fuzzy

quantity. In 2004, Abbasbandy and Asady [12] introduced a fuzzy trapezoidal approximation using the metric (distance) between two fuzzy numbers.
In section 2, we recall some fundamental result of fuzzy number. In section 3, we state Newton's method for solving fuzzy nonlinear equations. In section 4, we propose new approach for solving fuzzy nonlinear equations.

2. Preliminaries

Definition 2.1

A fuzzy number is a function $u : R \to I = [0,1]$ having the properties:
(i) u is normal;
(ii) u is fuzzy convex set;
(iii) u is upper semicontinuous on R;
(iv) The support $\{x \in R : u(x) > 0\}$ is a compact set.

The set of all fuzzy numbers is denoted by R_F. For $0 < r \le 1$, consider the level sets $[u]^r = \{x \in R : u(x) \ge r\}$ and $[u]^0 = \text{support}\{x \in R : u(x) > 0\}$.

A fuzzy subset $\widetilde{A}$ can be characterized as a set of ordered pairs of element x and grade $\mu_{\widetilde{A}}(x)$ and is often written $\widetilde{A} = \{(x, \mu_{\widetilde{A}}(x)) | x \in X\}$.

Definition 2.2

A fuzzy number u in parametric form is a pair $(\underline{u}, \overline{u})$ of function $\underline{u}(r)$ and $\overline{u}(r)$, $0 \le r \le 1$, which satisfies the following requirements:

(i) $\underline{u}(r)$ is a bounded monotonic increasing left continuous function,
(ii) $\overline{u}(r)$ is a bounded monotonic decreasing left continuous function,
(iii) $\underline{u}(r) \le \overline{u}(r) \qquad 0 \le \text{r} \le 1.$

A popular fuzzy number is the trapezoidal fuzzy number $u = (x, y, \delta, \beta)$ with left fuzziness δ and right fuzziness β where the membership function is

$$\mu_u(x)=\begin{cases}\frac{1}{\delta}(x-x_0+\delta) & x_0-\delta\le x\le x_0\\ 1 & x_0\le x\le y_0\\ \frac{1}{\beta}(y_0-x+\beta) & y_0\le x\le y_0+\beta\\ 0 & otherwise\end{cases}$$

And its parametric form is

$\underline{u}(r)=x_0-\delta+\delta r$ and $\overline{u}(r)=y_0+\beta-\beta r$.

Definition 3.2

For arbitrary $u=(\underline{u},\overline{u})$ and $v=(\underline{v},\overline{v})$ and $k>0$ the addition and multiplication by scalar k are defined as

$\underline{(u+v)}(r)=\underline{u}+\underline{v}$, $\overline{(u+v)}(r)=\overline{u}+\overline{v}$,

$\underline{(ku)}(r)=k\underline{u}$ and $\overline{(ku)}(r)=k\overline{u}$.

Definition 4.2

For arbitrary fuzzy number $u=(\underline{u},\overline{u})$ and $v=(\underline{v},\overline{v})$ the quantity

$$D(u,v)=[\int_0^1(\underline{u}-\underline{v})^2\,dr+\int_0^1(\overline{u}-\overline{v})^2\,dr]^{1/2}$$

is distance between u and v.

3. The Newton's method

For finding approximation of α, root of fuzzy nonlinear equation $F(x)=C$, with Newton's method, the parametric form is as followed:

$$\begin{cases}\underline{F}(\underline{x_n},\overline{x_n},r)=\underline{c}(r),\\ & \forall r\in[0,1]\\ \overline{F}(\underline{x_n},\overline{x_n},r)=\overline{c}(r).\end{cases}$$

Approximated solution is

$$\begin{cases}\underline{x_n}(r)=\underline{x_{n-1}}(r)+\underline{h_{n-1}}(r)\\ \\ \overline{x_n}(r)=\overline{x_{n-1}}(r)+\overline{h_{n-1}}(r)\end{cases}$$

Where

$$\begin{bmatrix} \underline{h_n} \\ \overline{h_n} \end{bmatrix} = \begin{bmatrix} \underline{F}_{\underline{x}} & \underline{F}_{\overline{x}} \\ \overline{F}_{\underline{x}} & \overline{F}_{\overline{x}} \end{bmatrix}^{-1} \begin{bmatrix} \underline{c}(r) - \underline{F}(\underline{x_{n-1}}, \overline{x_{n-1}}, r) \\ \overline{c}(r) - \overline{F}(\underline{x_{n-1}}, \overline{x_{n-1}}, r) \end{bmatrix}.$$

For initial guess, one can use the fuzzy number

$$x_0 = (\underline{x}(1), \overline{x}(1), \underline{x}(1) - \underline{x}(0), \overline{x}(0) - \overline{x}(1)),$$

Where $(\underline{x}, \overline{x}) = (\underline{\alpha}, \overline{\alpha})$ is parametric form of root of fuzzy nonlinear equation $F(x) = C$.

Parametric form of initial guess is

$$\underline{x}_0(r) = \underline{x}(1) + (\underline{x}(1) - \underline{x}(0))(r - 1)$$

And

$$\overline{x}_0(r) = \overline{x}(1) + (\overline{x}(0) - \overline{x}(1))(1 - r).$$

4.Trapezoidal Approximation for solving fuzzy nonlinear equation

To obtain a trapezoidal fuzzy number $x = (a, b, \delta, \beta)$ which is the nearest solutions of nonlinear systems $F(x) = C$ with respect to metric D, we minimize

$$D(F(\underline{x}(r), \overline{x}(r)), C(r)) =$$

$$[\int_0^1 (\underline{F}(\underline{x}(r), \overline{x}(r)) - \underline{C}(r))^2 dr + \int_0^1 (\overline{F}(\underline{x}(r), \overline{x}(r)) - \overline{C}(r))^2 dr]^{\frac{1}{2}}$$

where parametric form of $x = (a, b, \delta, \beta)$ is $\underline{x}(r) = a + \delta(r-1)$ and $\overline{x}(r) = b + \beta(1 - r)$.

Hence we have to minimize

$$d(a, b, \delta, \beta) = D(F(\underline{x}, \overline{x}), C(r))^2$$

in order to minimize $d(a, b, \delta, \beta)$, we consider

$$\frac{\partial d_n(\delta,\beta)}{\partial \delta}=0,$$
$$\frac{\partial d_n(\delta,\beta)}{\partial \beta}=0,$$
$$\frac{\partial d_n(\delta,\beta)}{\partial a}=0,$$
$$\frac{\partial d_n(\delta,\beta)}{\partial b}=0. \qquad (1)$$

Since the solution of above equation is not unique there for, we replace solution Of a,b,δ,β in $d(a,b,\delta,\beta)$ and best trapezoidal approximation is selected.

Numerical application

Example

Consider the fuzzy nonlinear equation

$(4,4,1,1)x^2+(2,2,1,1)x=(2,2,1,1)$

Without any loss of generality, assume that x is positive, then the parametric form of this equation is as follows

$$\begin{cases}(3+r)\underline{x}^2(r)+(1+r)\underline{x}(r)=(1+r),\\ (5-r)\overline{x}^2(r)+(3-r)\overline{x}(r)=(3-r).\end{cases}$$

With replace above equation system in (1) and replace solution of a,b,δ,β in D trapezoidal approximation is selected, if it was be minimize value. We have $a=.503$ and $\delta=.062$, $b=.502$, $\beta=.03$ so trapezoidal approximation is $x=(.503,.503,.062,.03)$

But in Newton's method to obtain initial guess we use above system for $r=0$ and $r=1$, therefore

$$\begin{cases}3\underline{x}^2(0)+1\underline{x}(0)=1,\\ 5\overline{x}^2(0)+3\overline{x}(0)=3.\end{cases} \quad \text{And} \quad \begin{cases}4\underline{x}^2(1)+2\underline{x}(1)=2,\\ 4\overline{x}^2(1)+2\overline{x}(1)=2.\end{cases}$$

Consequently $\underline{x}(0)=0.4343$ and $\overline{x}(0)=.5307$ and $\underline{x}(1)=\overline{x}(1)=1/2$

Therefore initial guess is $x_0=(.5,.5,.065,.031)$

After 2 iterations, we obtain the solution $x=(.5,.5,.063,.03)$ which the maximum error would be less than 10^{-3}.

References

[1] S. Abbasbandy, B. Asady, Newton's method for solving fuzzy nonlinear equations, Appl. Math. Comput. 159 (2004) 349–356.
[2] S. Abbasbandy, R. Ezzati, Newton's method for solving a system of fuzzy nonlinear equations, Appl. Math. Comput. 175 (2006) 1189–1199.
[3] J.J. Buckley, Y. Qu, Solving fuzzy equations: a new solution concept, Fuzzy Sets Syst. 39 (1991) 291–301.
[4] S. Chanas, On the interval approximation of a fuzzy number, Fuzzy Sets and Systems, 122(2001) 353-356.
[5] P. Grzegorzewski, Nearest interval approximation of a fuzzy number, Fuzzy Sets and Systems, 130 (2002) 321-330.
[6] E. Roventa , T. Spircu, Averaging procedures in defuzzification processes, Fuzzy Sets and Systems 136 (2003) 375-385.
[7] M. Ma, A. Kandel, M. Friedman, A new approach for defuzzification, Fuzzy Sets and Systems, 111 (2000) 351-356.
[8] S. Abbasbandy, M. Amirfakhrian, The nearest trapezoidal form of a generalized left right fuzzy number, International Journal of Approximate Reasoning, 43 (2006) 166-178.
[9] P. Grzegorzewski, E.Mrowka, Trapezoidal approximations of fuzzy numbers, Fuzzy Sets and Systems, 153 (2005) 115-135.
[10] P. Grzegorzewski, E.Mrowka, Trapezoidal approximations of fuzzy numbers-revisited, Fuzzy Sets and Systems, 158 (2007) 757-768.
[11] P. Grzegorzewski, E.Mrowka, Trapezoidal approximations of fuzzy numbers preserving the expected interval -algorithms and properties, Fuzzy Sets and Systems, 159 (2008) 1354-1364.
[12] S. Abbasbandy, B. Asady, The nearest trapezoidal fuzzy number to a fuzzy quantity, Applied Mathematics and Computation, 156 (2004) 381-386.

Nonlinear Dynamic System Theory and Economic Complexity

Aleksander Jakimowicz

University of Warmia and Mazury in Olsztyn, Faculty of Economic Sciences, Department of Quantitative Methods, Poland
E-mail: aleksander.jakimowicz@uwm.edu.pl

Abstract: Catastrophe theory and deterministic chaos constitute basic elements of the science of complexity. Elementary catastrophes were the first form of nonlinear, topological complexity that were seriously studied in economics. Deterministic chaos and other types of complexity succeeded catastrophe theory. In general, chaos means the seemingly random behavior of a deterministic system, which stems from high sensitivity to its initial conditions. Nonlinear dynamic systems theory, which unites various manifestations of complexity into one integrated system, is contrary to the assumptions that markets and economies spontaneously strive for a state of equilibrium. To the contrary, their complexity seems to grow due to the influence of classic economic laws. In my paper, I indicate that with time, model economic systems strive for a state we call "the edge of chaos". I consider two cases. The first case concerns an economy based on a two-stage accelerator, where the economic cycle adopts the form of chaotic hysteresis. The second case concerns a Cournot-Puu duopoly model in which striving for the edge of chaos stems from profit maximization by entrepreneurs. The evolution of systems at the edge of chaos can be sudden, which makes it necessary to consider it in terms of elementary catastrophes.
Keywords: Cusp catastrophe, Chaotic hysteresis model, Cournot-Puu duopoly model, Edge of chaos, System classification, Economic transformation, Rule of progressive complexity.

1. Introduction: Foundations of catastrophe theory

1.1. Classification Theorem

The theory of catastrophes, also known as the theory of morphogenesis, appeared in science in the mid-1970s [25]. It is a general method of system modeling focusing on the way in which discontinuous effects can emerge from continuous causes. Let the dynamic system be represented by a smooth function:

$$f : \mathbf{R}^k \times \mathbf{R}^n \to \mathbf{R}, \tag{1}$$

where $\mathbf{R}^k$ is a control space representing a set of causes, whereas $\mathbf{R}^n$ is a space of states (behavior) representing a set of effects. The function *f* is called a potential function. If the internal dynamics of the system consist in striving for a local maximum, then the potential function can represent the probability of it being found.

The basis of catastrophe theory is the classification theorem [26]. This states that if the co-dimension *k* of elementary catastrophes is bigger than 5, they create a finite family of discontinuous transition types. Every sudden dynamic change can be assigned to one of those types. The relation between the number of catastrophes and the co-dimension is shown in Table 1.

Table 1. Elementary catastrophe classification in relation to the co-dimension *k*

Co-dimension value (*k*)	1	2	3	4	5	6	7 …
Number of elementary catastrophes	1	2	5	7	11	∞	∞

From an application point of view, the case $k = 4$ is important, since $\mathbf{R}^4$ can be interpreted as a physical space-time in which all events take place. There are seven types of singularities in this case: fold, cusp, swallowtail, butterfly, hyperbolic umbilic, elliptic umbilic, and parabolic umbilic [5].
The application of the catastrophe theory in economics is possible only when the law governing a given phenomenon or process has been well-defined. In such a case, the catastrophe theory will facilitate the choice of the easiest mathematical structure, which will generate a behavior closest to real. Another equally point is to use metaphors properly [8].

1.2. The cusp catastrophe

The cusp catastrophe is one of the most common elementary catastrophes in economic applications. The potential function has the following form:

$$f : \mathbf{R}^2 \times \mathbf{R}^1 \to \mathbf{R}, \tag{2}$$

Thus, the control space is two-dimensional, whereas the state space is one-dimensional. The function (2) has a simple multinomial representation:

$$f(c_1, c_2, x) = \frac{1}{4}x^4 + \frac{1}{2}c_1x^2 + c_2x, \tag{3}$$

where x stands for the state variable, whereas c_1 and c_2 are the control parameters [28]. The manifold of the catastrophe defining the surface area of the system equilibrium is dependent on the following formula:

$$M_3 = \left[(c_1, c_2, x) : \frac{df}{dx} = 0, \frac{df}{dx} = x^3 + c_1x + c_2\right]. \tag{4}$$

The system proceeds along this surface in a continuous way, until it comes across a set of singularities. There is then a sudden jump to another equilibrium surface and the continuous evolution continues until the next jump.

2. Deterministic chaos

2.1. Nonlinearity as a necessary condition for complexity

In order to define nonlinearity it is necessary to clearly define linearity. In all linear systems, the binding rule is the rule of superposition. This states that the system's reaction to two or more stimuli is the sum of reactions triggered individually by each of these stimuli. If factor *A* triggers reaction *X*, and factor *B* reacts to *Y* then the factor ($A + B$) results in ($X + Y$). In other words, linear systems are additive.

The rule of superposition implies the linearity of the system if we supplement it with the condition of homogeneity. A lack of additiveness and homogeneity implies the nonlinearity of the system. The main causes of nonlinearity in economics are:

- Limitations imposed on the economic variables [2].
- Technical-balance laws of production [15].
- Technical-organizational factors [10].
- Bounded rationality [24].
- Processes of expectation formation [4].
- Adaptive processes of economic-agent learning [3].
- The shape (protuberance) of the indifference curves.
- Aggregation processes of some variables [27].
- Evolution of competition rules [3].
- Psychological laws [14].

Nonlinearity is a necessary condition, but it is not enough to trigger chaos. Statistical tests confirm that nonlinearity is a phenomenon that is common in economic time series, and part of them proves that deterministic chaos exists. There are strong grounds to claim that in the future, the role of nonlinearity in economic explorations will become more significant.

2.2. The butterfly effect

Deterministic chaos means a seemingly random behavior of the deterministic system, thus one which is strictly subject to specific rules. The reason for the stochastic behavior of some nonlinear deterministic systems is their unusually sensitive dependence on initial conditions, which was named 'the butterfly effect' by Lorenz [16]. A slight disturbance in the initial conditions after some time causes significant changes in the system behavior as trajectories begin to disperse exponentially. As picturesquely described Lorenz, a proverbial flap of butterfly wings in Brazil can cause a tornado in Texas.

The Lyapunov exponents are amongst the most frequently-used quantitative measures of the trajectory divergence. This notion has been used by Oseledec [20] in a well-known multiplicative ergodic theorem. The Lyapunov exponent for one-dimensional map is as follows:

$$W^L = \lim_{n\to\infty} \lim_{\varepsilon\to 0} \frac{1}{n} \ln \left| \frac{f^n(x_0+\varepsilon) - f^n(x_0)}{\varepsilon} \right| = \lim_{n\to\infty} \frac{1}{n} \ln \left| \frac{d\, f^n(x_0)}{d\, x_0} \right| . \quad (5)$$

Symbols $f^1, f^2, \ldots, f^n$ stand for subsequent iterations, x_0 and $x_0 + \varepsilon$ are the initial conditions for the two trajectories. The number $\varepsilon > 0$ is very small. With every iteration, the distance between the trajectories increases exponentially. This definition can also be generalized with multi-dimensional systems. The number of exponents has to correspond to the number of dimensions. If the largest exponent of a dynamical system is positive, this indicates a chaotic trajectory, while an exponent equal to zero indicates the bifurcation point, and a negative value means convergence of the trajectory with the constant point of attraction or a periodic attractor.
The basic notion of nonlinear dynamical systems theory is also the notion of an attractor, primarily a chaotic attractor. Let *F* stand for a map of *m*-dimensional space into itself. The compact set *A*, which is situated in the *m*-dimensional space, we call the attractor for *F* if it meets the conditions of invariance, density, stability and attraction. An attractor is a chaotic attractor if it contains a chaotic trajectory [19].

2.3. System classification in nonlinear dynamical systems theory
In order to compare the subjects of conventional science, the theory of deterministic chaos, and the theory of complexity, we can classify systems based on the following criteria: the number of constituents of the system *N* and the average number of links between these elements *K* (see [11, 12, 13]). Depending on the relationship between these parameters, we can distinguish three types of the *NK* systems:

- Type I – subcritical systems. The number of links is very small, given the number of elements. Every element is technically independent from others, thus the behavior of the whole system can be treated as a simple sum of its parts. Because the rule of superposition is met in such a case, systems of this type are approximately linear. Their dominating behavior is striving for states of equilibrium.
- Type II – critical systems. The average number of links is substantially greater than in the subcritical systems. These systems are characterized by more complex dynamics and can reveal emergent properties [7]. Local changes can be dispersed in a system so they usually do not bring about global consequences. These types of systems often balance on the edge of chaos (this is a state when the system's ability to survive is the greatest and its computing power reaches maximum value).
- Type III – supercritical systems. The ratio of the number of links to the number of elements approaches one. It is a state in which almost every element is interlinked with all the rest. It includes deterministic systems, which are characterized by complex dynamics.

The largest Lyapunov exponent for subcritical systems is negative, for critical systems it oscillates around zero, whereas for supercritical systems it is positive. Classical science deals with systems of type I, the theory of chaos explores systems of type III, whereas the subject of interest for the theory of complexity is type II and the transitions between various types of systems (see [7, 21]).

3. Applications in economics

3.1. The theory of economic transformation

The first step towards elaborating a theory of transformation was taken by American researchers who formulated a model of chaotic hysteresis (see [22, 23]). Two basic nonlinear dynamic system theory methods were applied concurrently, i.e. elementary catastrophes and deterministic chaos. The starting point is a socialist economy. According to the Marxist convention, the economy was divided into two sectors: consumption-goods and capital-goods. The notion of a technological gap and the cusp catastrophe were used to describe social-economic crises. The attractor in the form of a chaotic hysteresis that appears in a reformed economy is a result of a two-phase activity of a nonlinear accelerator.

The dynamic system is described by a two-dimensional formula:

$$I_t = I_{t-1} + Z_t , \tag{6}$$

$$Z_t = u\left(Z_{t-1} - Z_{t-1}^3\right) - v\,I_{t-1} , \tag{7}$$

where: I_t – total investment within the period *t*, Z_t – increase in the investment, whereas symbols *u* and *v* means respectively the values of accelerators in the capital-goods sector and in the consumption-goods sector. These formulas cannot be solved analytically, but they can be the subject of numerical explorations.

An analysis of the system (6)–(7) was conducted assuming the constant value of the accelerator in the sector of capital goods $u = 2$, whereas the value of the parameter v was gradually decreased. For $0.01 \le v \le 0.1395$ in the phase space of the system there is an investment cycle in the form of a chaotic attractor. Lowering the value of the accelerator of the consumption-goods sector means the metamorphosis of the attractor – eventually for the value of $v = 0.00005$ it takes on the form of chaotic hysteresis. The attractor in this form is featured in Figure 1. In the model, there is a trade-off between complexity (chaos) and instability, understood as the increase of period and amplitude of oscillation of investment [6].

The next element of the theory is the technological gap (*G*), which stems from the higher rate of capital-intensive nature of production in socialism compared to a capitalist economy. Paradoxically, this phenomenon is a result of pursuing the postulates of stability of production and full employment, which were to make socialism a system more bearable for people than capitalism with its chronic unemployment and crises.

Another step is to introduce the cusp catastrophe, whose space area of equilibrium meets condition (4). In the theory under investigation, the variable of this state is the probability of an introduction of market reforms $x = P(s)$, the bifurcation parameter is the dimensions of the technological gap $c_1 = G$, whereas the asymmetric parameter is the rate of growth of investment $c_2 = Z/I$. In the Figure 2 there is a geometrical interpretation of the morphogenetic model of transformation.

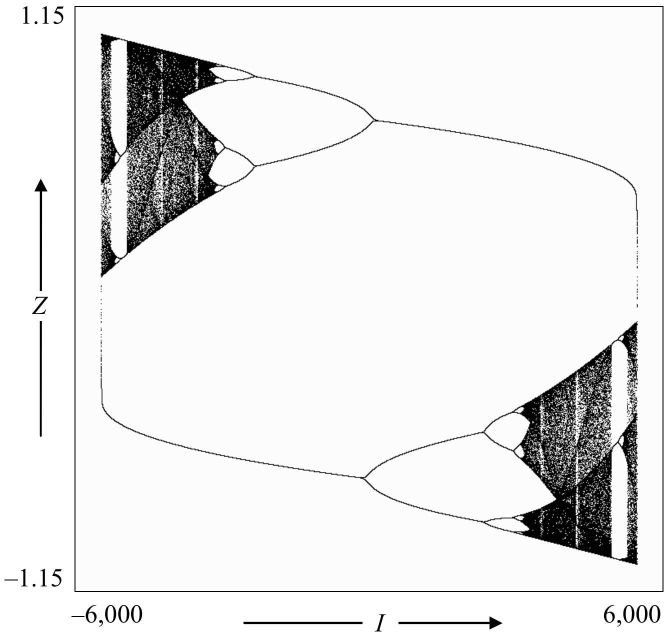

Figure 1. The chaotic attractor in the form of chaotic hysteresis for $u = 2$, $v = 0.00005$

The space of the catastrophe equilibrium describes various scenarios of economic crises and the corresponding reforms that sought to answer them. For $G = 0$ we have an example market economy. The occurrence of the technological gap, which happens after passing through the beginning of catastrophe, causes a division of the equilibrium space into two layers – an upper and lower. They suggest the occurrence of nonlinear changes in the probability of transformation, whenever the rate of investment growth reaches a necessary value. Sudden leaps take place when the asymmetric factor crosses the bifurcation set of the catastrophe located in the parameter space marked by the following formula:

$$B_3 = \left[(c_1, c_2) : 4c_1^3 + 27c_2^2 = 0 \right]. \tag{8}$$

Numerical explorations of model (6)–(7) have shed new light on a certain macroeconomic problem which has been neglected by mainstream economics regarding the macroeconomic costs of the reform complexity. An intuitive understanding of this category of costs is known from the theory of the corporation [18]. The global financial crisis prompted a wider look at the complexity of economic processes and the accompanying problems [1]. An economy under transformation is vulnerable to falling victim to trade-offs between complexity and instability, which accounts for the fact that benefits

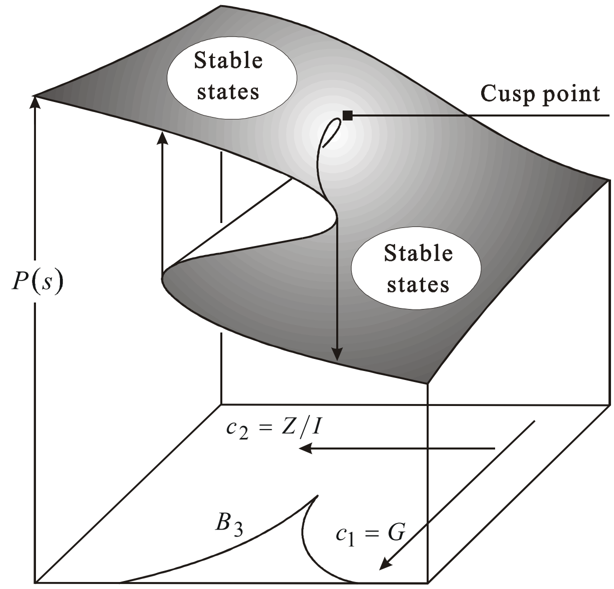

Figure 2. Geometrical interpretation of a morphogenetic transformation model

stemming from reforms can, over a long period of time, consolidate below the costs of complexity. It is a new, quality-based position in the balance of transformation. Future research should focus on methods of its measurement. In addition, it constitutes a challenge to economic policy, which should seek to simplify economic life.

3.2. The rule of progressive complexity

Mathematical studies of standard nonlinear economic models have revealed an interesting regularity, which I called "the rule of progressive complexity" [9]. It appears that there are two active forces in economic systems. The first force is short term in nature, and its source stems from rational, typical endeavors of business entities. One of the manifestations of this activity is profit maximization by producers and maximization of utility by consumers. As a result, these systems seek a state of short-term equilibrium. The second force is active over a long period of time and even though its source is identical to the first one, the effects are totally different. It destabilizes the short-term states of equilibrium and pushes market structures towards a state known as "the edge of chaos". It is a transition field between a periodic behavior and chaotic behavior, where the computing power of systems, which means their ability to collect and process information, reaches its maximum. The complexity of a system, which can been measured by Lapunov exponents, increases in this field.

Let us consider a duopoly model using the following equations:

$$x_{t+1} = \sqrt{\frac{y_t}{a}} - y_t\,, \tag{9}$$

$$y_{t+1} = \sqrt{\frac{x_t}{b}} - x_t\,, \tag{10}$$

where: x – the production output of the first entrepreneur, y – the production output of the second entrepreneur, whereas a and b stand for their marginal costs, respectively. In the static version, these equations set the reaction functions. Each of them describes the choice of the production output made by an entrepreneur assuming that the production output of their competitor is known. The collision of these two functions takes place at the point known as the Cournot-Nash equilibrium point.

The standard analysis of the model's stability allows us to set two critical values of the marginal costs ratio:

$$\frac{a}{b} \vee \frac{b}{a} = 3 \pm 2\sqrt{2}\,. \tag{11}$$

This is where the analytical methods give up. We do not know what happens to this model when the stability threshold is crossed, or how it behaves over a long period.

It is best to start numerical explorations of a duopoly (9)–(10) with making a period plot [19]. This is a two-dimensional space of parameters in which various behavior of the system has been specified (with emphasis on periodic behavior). In order to do this, one should define the interval of changeability of both parameters and the initial condition of the trajectory bundle. A plot of this type allows us to follow the dynamics of the system depending on a simultaneous change in two control parameters.

Numerical explorations of parameter space reveal the following types of behavior: states of short-term equilibrium, periodic dynamics, chaos and divergent trajectories (see Figure 3). Pairs of parameters responsible for states of stable equilibrium account for 82.77% of the parameter space, whereas pairs of chaotic parameters account for mere 0.15% of this space. Consequently, it seems that stability predominates and the claims of conventional economics have been confirmed. However, it is a false conclusion. Entrepreneurs are interested not only in maximizing profit over a short time, but also in the long run. Maximizing profit in the long run requires introducing technical-organizational progress and it results in lowering marginal costs. Consequently, every producer strives for one of the two edges of chaos (11), i.e. states with growing complexity [9].

The system displays a certain type of globally rational behavior which contributes to its survival. As of the moment the efficient producer achieves the

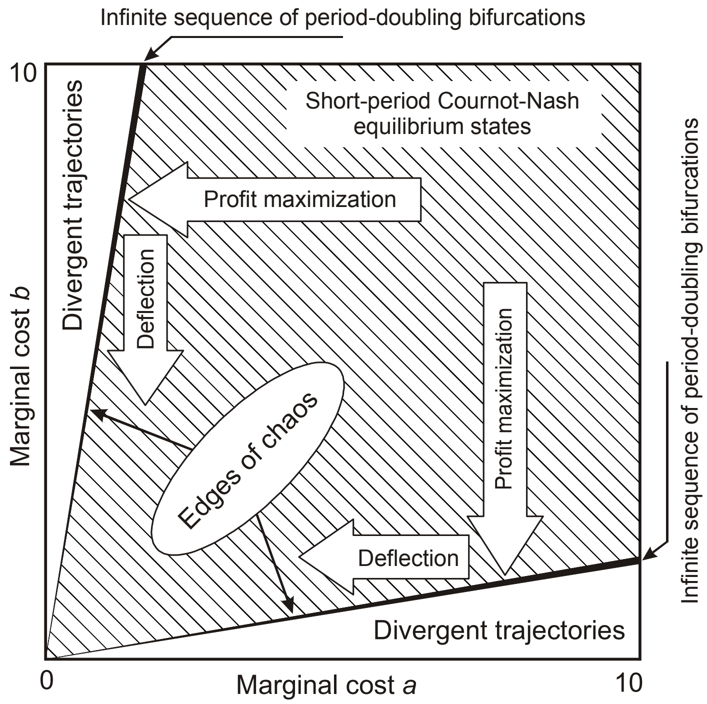

Fig. 3. Dynamics of the Cournot-Puu duopoly in the parameter space

edge of chaos, his long-term profit decreases, and the long-term profit of the inefficient producer begins to grow [17]. This leads to role reversal, and in the diagram, the market bounces off the edge of chaos.

4. Conclusions

Catastrophe means a violent, sudden transition of the tested system into a new state. What is important here is the rapidity of the changes in the behavior of an object as compared with the mean change in the past. Catastrophe theory merges two apparently contradictory and unrelated kinds of phenomena descriptions to form one coherent notion system: evolutionism and revolutionism, continuity and discontinuity. In economics, the application of catastrophe theory is of great cognitive importance, particularly in issues of explanation and forecasting in economics.

In transitional economies, there is a trade-off between complexity and instability. In the economic calculation of transformations, a new type of cost needs to be considered – the social costs connected with the change of the dynamic complexity of the systems. Numerical explorations of an archetypal duopoly model have proven that states of equilibrium are stable only for a short period. In the long run, such systems strive for the edge of chaos.

References

1. J. C. Bogle. Dość. *Prawdziwe miary bogactwa, biznesu i życia*, PTE, Warszawa, 2009.

2. J. R. Hicks. *A Contribution to the Theory of the Trade Cycle*, Clarendon Press, Oxford, 1951.
3. C. H. Hommes. Economic dynamics. In: Scott AC (ed) *Encyclopedia of Nonlinear Science*. Routledge, New York, pp. 245–248, 2005.
4. C. H. Hommes. Heterogeneous agent models in economics and finance. In: Tesfatsion L, Judd KL (eds) *Handbook of Computational Economics*, vol. 2: *Agent-Based Computational Economics*. North-Holland, Amsterdam, pp. 1109–1186, 2006.
5. A. Jakimowicz. *Od Keynesa do teorii chaosu. Ewolucja teorii wahań koniunkturalnych*, Wydawnictwo Naukowe PWN, Seria: „Współczesna Ekonomia”, Warszawa, 2005.
6. A. Jakimowicz. Interdisciplinary Matrix in Economics: Two Applications to the Transition from Socialism to Capitalism, *Nonlinear Dynamics, Psychology, and Life Sciences*, vol. 13, no. 4, 393–421, 2009a.
7. A. Jakimowicz. O niektórych implikacjach nieliniowości w keynesizmie, *Ekonomista*, no. 1, 15–48, 2009b.
8. A. Jakimowicz. Catastrophes and Chaos in Business Cycle Theory, *Acta Physica Polonica A*, vol. 117, no. 4, 333–339, 2010a.
9. A. Jakimowicz. *Źródła niestabilności struktur rynkowych*, Wydawnictwo Naukowe PWN, Seria „Współczesna Ekonomia”, Warszawa, 2010b.
10. M. Kalecki. Zarys teorii wzrostu gospodarki socjalistycznej. In: Kalecki M, *Dzieła*, vol. 4: *Socjalizm. Wzrost gospodarczy i efektywność inwestycji*. PWE, Warszawa, pp. 17–124, 1984.
11. S. A. Kauffman. *The Origins of Order: Self-Organization and Selection in Evolution*, Oxford University Press, New York, 1993.
12. S. A. Kauffman and S. Levin. Towards a General Theory of Adaptive Walks on Rugged Landscapes, *Journal of Theoretical Biology*, vol. 128, no. 1, 11–45, 1987.
13. H. Kaul and S. H. Jacobson. Global Optima Results for the Kauffman NK Model, *Mathematical Programming*, vol. 106, no. 2, 319–338, 2006.
14. J. M. Keynes. *Ogólna teoria zatrudnienia, procentu i pieniądza*, PWN, Warszawa, 1985.
15. O. Lange. Prawa ekonomiczne. In: O. Lange, *Dzieła*, vol. 3: *Ekonomia polityczna*. PWE, Warszawa, pp. 260–304, 1975.
16. E. N. Lorenz. *The Essence of Chaos*, UCL Press, London, 1995.
17. A. Matsumoto. Controlling the Cournot-Nash Chaos, *Journal of Optimization Theory and Applications*, vol. 128, no. 2, 379–392, 2006.
18. A. Noga. *Teorie przedsiębiorstw*, PWE, Warszawa, 2009.
19. H. E. Nusse and J. A. Yorke. *Dynamika. Badania numeryczne*, Wydawnictwo Naukowe PWN, Warszawa, 1998.
20. V. I. Oseledec. Мультипликативная эргодическаяа теорема. Характеристичес-кие показатели Ляпунова динамических систем, *Труды Московского Математического Общества*, vol. 19, 179–210, 1968.
21. M. Pigliucci. Chaos and Complexity. Should We Be Skeptical?, *Skeptic*, vol. 8, no. 3, 62–70, 2000.
22. J. B. Rosser and M. V. Rosser. Discrete Dynamics in Transitional Economies, *Discrete Dynamics in Nature and Society*, vol. 1, 269–281, 1998.

23. J. B. Rosser, M. V. Rosser, S. J. Guastello and R. W. Bond. Chaotic Hysteresis and Systemic Economic Transformation: Soviet Investment Patterns, *Nonlinear Dynamics, Psychology, and Life Sciences*, vol. 5, no. 4, 345–368, 2001.
24. T. J. Sargent. *Bounded Rationality in Macroeconomics*, Clarendon Press, Oxford, 1993.
25. R. Thom. *Structural Stability and Morphogenesis. An Outline of a General Theory of Models*, Benjamin, London, 1975.
26. D. Trotman and E. C. Zeeman. Klasyfikacja elementarnych katastrof kowymiaru ≤ 5. In: Cieślak M, Smoluk A (eds) *Zbiory rozmyte. Rozpoznawanie obrazów. Teoria katastrof. Wybór tekstów*. PWN, Warszawa, pp. 123–194, 1988.
27. H. R. Varian. *Mikroekonomia. Kurs średni. Ujęcie nowoczesne*, Wydawnictwo Naukowe PWN, Warszawa, 1995.
28. E. C. Zeeman. *Catastrophe Theory: Selected Papers, 1972–1977*, Addison-Wesley, London, 1977.

Proceedings, 6th Chaotic Modeling and Simulation International Conference
11 - 14 June 2013 Istanbul, Turkey

Fast-slow and Chaotic Behaviors in a Delay-coupled Flexible Joint System

Shanying Jiang, Jian Xu, Yu Huang

School of Aerospace Engineering and Applied Mechanics, Tongji University, Shanghai 200092, China
E-mail: xujian@tongji.edu.cn

Abstract: The delay-coupled flexible joint system is presented in this paper. The geometric singular perturbation method is used to obtain the critical manifold defining as the equilibrium of the fast subsystem. The eigenvalue analysis of the fast subsystem reveals a relation between the stability of the critical manifold and the time delay. With different values of the time delay, numerical simulations are performed to display some interesting dynamic behaviors of the fast-slow system. The formation mechanisms of these complex dynamics are expounded.
Key words: flexible joint, time delay, geometric singular perturbation, bursting, chaos

1. Introduction

Systems with multiple time scales are usually named as the singularly perturbed systems or the fast-slow systems. The fast-slow property of such systems may cause various complex nonlinear dynamics, representative ones are spiking, bursting and relaxation oscillation. Izhikevich [1] given out a comprehensive classification of spikes and bursters in his brilliant work. He well explained the bifurcation mechanisms involved in the generation of spiking and bursting and completed the existing classification. Because of the multiple time scales, the fast-slow systems usually have special structures and thus cause the failure of general perturbation methods [2]. Jones [3] proposed an improved perturbation method named geometric singular perturbation method from the view of geometry. This method was proved to be quite effective in the ecosystems [4] and in neuroscience [5].

The rigid-link flexible-joint arm is a representative fast-slow system in the mechanical field. It was firstly derived by Spong [6] in 1980s. Chen [7] considered the neglected time delay and improved Spong's model into a delay-coupled one. In this paper, the wave propagation time along the long, thin, elastic shaft is defined as the origin of the time dealy. The purpose of this paper is to explore the influence of such kind of time delay. The paper is organized as follows. In section 2, an improved model of time-delayed flexible-joint system is established. In section 3, the bursting behavior and the chaotic bursting are obtained in numerical simulation. Then, with the increasing of the time delay, the continuous chaotic oscillation appears. Section 4 contains some conclusions.

2. The Flexible Joint System

To investigate the effect of the multiple time scales on a delay-coupled system, we introduce the one rigid-link flexible-joint robot manipulator. As is shown in Fig.1, a rigid rotor is connected with a rigid link via an elastic long shaft which is modeled as a liner torsion spring with stiffness K. Assume that the inertia of the link is I and the inertia of the rotor is J about the rotation axis. Let $\theta_1(t)$ be the angular displacement of the link and $\theta_2(t)$ be the angular displacement of the shaft, both having the vertical axis as their angular reference. Considering that there is a time delay τ in the propagation of the angular displacement from the rotor to the link and vice versa from the link to the rotor in the reaction process, then, the governing equation is constructed to be

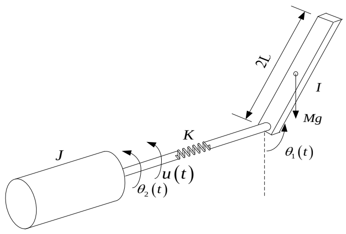

Fig.1. The flexible joint system

$$
\begin{aligned}
&I\ddot{\theta}_1(t)-c_1\left(\dot{\theta}_2(t)-\dot{\theta}_1(t-\tau)\right)-K\left(\theta_2(t)-\theta_1(t-\tau)\right)+MgL\sin\theta_1(t)=0,\\
&J\ddot{\theta}_2(t)+c_1\left(\dot{\theta}_2(t)-\dot{\theta}_1(t-\tau)\right)+K\left(\theta_2(t)-\theta_1(t-\tau)\right)+c_2\dot{\theta}_2(t)=u(t),
\end{aligned}
$$

where M is the total mass of the link, L is the distance from the axis of rotation to the mass centre of the link, g is the acceleration constant of gravity and $u(t)$ is the torque applied to the shaft by the actuator. Besides, c_1 stands for the damping coefficient inside the system and c_2 stands for the damping coefficient outside the system.

To distinguish the different scales, dimensionless parameters are introduced as

$$\frac{I}{J}=\varepsilon^2,\quad \frac{c_1}{\sqrt{KJ}}=\alpha_1,\quad \frac{c_2}{\sqrt{KJ}}=\alpha_2,\quad \frac{MgL}{K}=\beta .$$

Then, a typical fast-slow system is obtained as

$$\begin{aligned}
&\varepsilon\dot{\theta}_1(t)=p_1(t),\\
&\varepsilon\dot{p}_1(t)=\bar{\alpha}_1\left(\varepsilon p_2(t)-p_1(t-\tau)\right)+\left(\theta_2(t)-\theta_1(t-\tau)\right)-\beta\sin\theta_1(t),\\
&\dot{\theta}_2(t)=p_2(t),\\
&\dot{p}_2(t)=-\bar{\alpha}_1\left(\varepsilon p_2(t)-p_1(t-\tau)\right)-\left(\theta_2(t)-\theta_1(t-\tau)\right)-\alpha_2 p_2(t)+u(t),
\end{aligned}$$

where θ_1, p_1 are defined as the fast variables, θ_2, p_2 are slow variables and $0<\varepsilon\ll 1$, $\alpha_1=\varepsilon\bar{\alpha}_1$, $\alpha_1\sim 10^{-1}$, $\beta\sim 10^0$, $\alpha_2\sim 10^{-1}$.

According to the singular perturbation theory, the limit of the original full system as $\varepsilon\to 0$ is defined as the reduced slow subsystem and the limit of the rescaled full system with $t=\varepsilon\bar{t}$ as $\varepsilon\to 0$ is the reduced fast subsystem.

The slow manifold of the full system is defined as equilibrium of the fast subsystem, denoted as

$$M_0=\left\{(\theta_1,p_1,\theta_2,p_2)\in\mathbb{R}^4:\ p_1(t)=0,\ -\bar{\alpha}_1 p_1(t)+\left(\theta_2(t)-\theta_1(t)\right)-\beta\sin\theta_1(t)=0\right\}$$

and the equilibrium manifold is obtained as

$$M_\varepsilon=\left\{(\theta_1,p_1,\theta_2,p_2)\in\mathbb{R}^4: p_2(t)=0,\bar{\alpha}_1 p_1(t-\tau)-\left(\theta_2(t)-\theta_1(t-\tau)\right)-\alpha_2 p_2(t)+u(t)=0\right\}$$

To analyze the stability switches of the slow manifold M_0, a characteristic equation of the fast subsystem attracts our attention

$$D(\lambda)=\lambda^2+e^{-\lambda\tau}\bar{\alpha}_1\lambda+e^{-\lambda\tau}+\beta\cos\theta_1=0 .$$

When $1+\beta\cos\theta_1=0$, $\lambda=0$ is always a root of $D(\lambda)$, otherwise, when

$1+\beta\cos\theta_1 \neq 0$, assuming that the characteristic equation has a pair of pure imaginary roots $\lambda = \pm i\omega \ (\omega > 0)$, separating the real and the imaginary parts and considering the equation $\sin^2(\omega\tau)+\cos^2(\omega\tau)=1$, the following equation is obtained

$$F(\Omega)=\frac{\Omega^2-\left(\bar{\alpha}_1^2+2\beta\cos(\theta_1)\right)\Omega+\beta^2\cos^2(\theta_1)-1}{1+\bar{\alpha}_1^2\Omega}=0,$$

where $\Omega=\omega^2$.

Without loss of generality, set the values of the system parameters as $\bar{\alpha}_1=1.5,\ \beta=3$, and the relationship between the rest quantities, namely, Ω and θ_1, is illustrated in Fig.2.

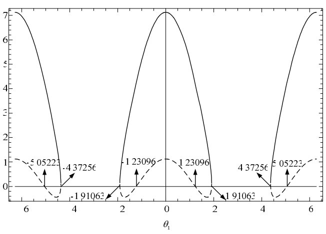

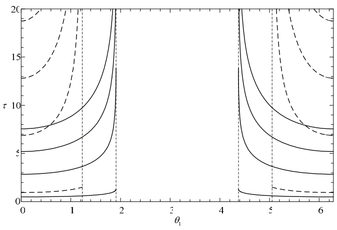

Fig.2. The solution curves of $F(\Omega)=0$ Fig.3. The stability boundaries

With $\theta_1 \in (0,\ 1.23096)$, $F(\Omega)=0$ has two positive roots,

$$\omega_{1,2}=\sqrt{0.125\left(9+24\cos(\theta_1)\mp 20.7846\sqrt{0.335648+\cos(\theta_1)}\right)}.$$

With $\theta_1 \in (1.23096,\ 1.91063)$, there' one positive root ω_1, with $\theta_1 \in (1.91063,\ 4.37256)$, no positive root and with $\theta_1 \in (4.37256,\ 5.05223)$, one positive root ω_1. At last, with $\theta_1 \in (5.05223,\ 2\pi)$, there are two positive roots, namely, ω_1 and ω_2, again.

Substituting ω_1, ω_2 back into the sinusoidal function, a series of branch lines on the θ_1-τ plane are determined as

$$\tau_{1,2} = \frac{1}{\omega_{1,2}}\left(2m\pi \pm \arcsin\left(\frac{1.5\omega_1\left(\omega_1^2 - 3\cos\left(\theta_1\right)\right)}{1+2.25\omega_1^2}\right)\right),\ m = 0,1,2\ldots.$$

As is shown in Fig.3, the θ_1-τ plane is divided by these branch lines and those interval boundaries into several regions. With a certain time delay τ_{const}, a horizontal line $\tau = \tau_{const}$ will cross these separatrix from the left to the right and thus determines the stability switch points of the slow manifold.

3. Delay-induced Chaotic Behaviors

In this section, discussion pivots on the free oscillation of the flexible-joint system, i.e., when $u\left(t\right) = 0$. Simulation results indicate that some complex phenomena will emerge due to the effect of the multiple scales and different values of the time delays.

Case 1, $\tau = 0.68$

In this case, the horizontal line $\tau = 0.68$ intersects with the boundary curves at four points and thus separates the slow manifold into five segments, see Fig.4.

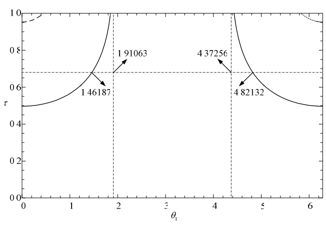

Fig.4. The zoom of Fig.3

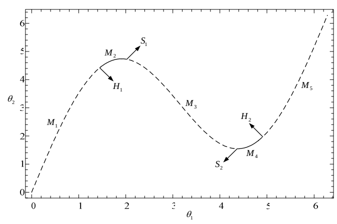

Fig.5. The structure of the slow manifold

Fig.5 illustrates the corresponding structure of the slow manifold. According to the geometric singular perturbation theory, the stable segments of the slow manifold attract the flow and those unstable ones repel the flow. Considering the slow manifold structure in Fig.5, it is surmised that starting from an initial point $\left(\theta_1,\theta_2\right) = \left(2,3\right)$, the flow of the system would be repelled by the unstable segment M_1 and move around the limit cycle bifurcated from the Hopf point H_1 until it is attracted by the stable segment M_2. It moves along M_2 and jumps at the saddle-node point S_1 from the left to the right unstable segment M_5. Because of the symmetry, the flow would move around the limit cycle bifurcated from the Hopf point H_2 and be attracted by the stable segment M_4 until it jumps at the saddle-node point S_2 to the left and thus forms a big loop, namely, the phase portrait, as is illustrated in Fig.6. Fig.7 shows the phase portrait on the p_1-θ_1 plane and Fig.9 presents from a three-dimensional view. The corresponding time history plot is presented in Fig.8 and this kind of periodic cluster phenomenon is called the bursting.

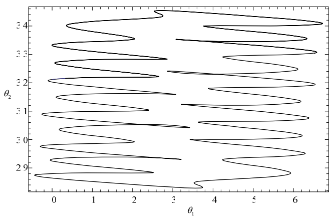

Fig.6. Phase portrait ($\tau = 0.68$)

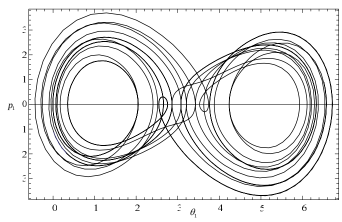

Fig.7. Phase portrait ($\tau = 0.68$)

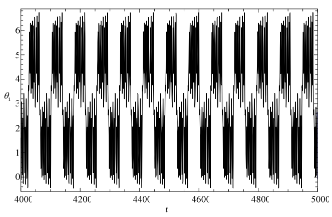

Fig.8. Time series ($\tau = 0.68$)

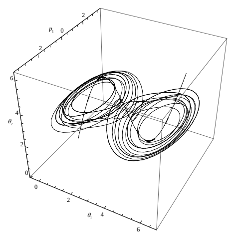

Fig.9. Solution trajectory ($\tau = 0.68$)

Case 2, $\tau = 0.685$

With the increase of the time delay, the flow begins to move and jump between the left and the right attractors irregularly and thus leads to a series of complex dynamics behaviors. As $\tau = 0.685$, keeping the other parameters fixed as the case when $\tau = 0.68$, the phase portraits of the system are shown as follows in Fig.10, Fig.11 and Fig.13. Fig.12 illustrates an irregular bursting phenomenon and in some literatures it is called the chaotic bursting.

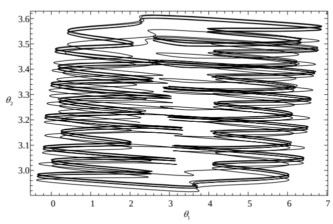

Fig.10. Phase portrait ($\tau = 0.685$)

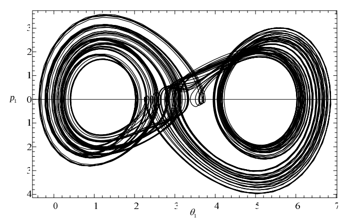

Fig.11. Phase portrait ($\tau = 0.685$)

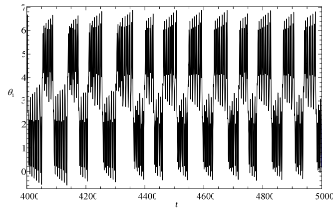

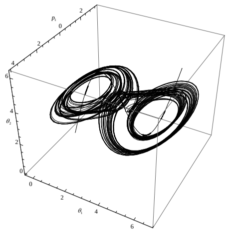

Fig.12.Time series ($\tau = 0.685$) Fig.13.Solution trajectory($\tau = 0.685$)

Case 3, $\tau = 0.7$

As the time delay continues increasing to $\tau = 0.7$, the irregularity of the flow motion gets worse and a chaotic behavior is obtained. Fig.14, Fig.15 and Fig.19 demonstrate the phase portraits and Fig.16, Fig.17 are the Poincare maps. Obtained from Fig.18, the behavior of the system is in an extreme disorder and it should be avoided in the design process.

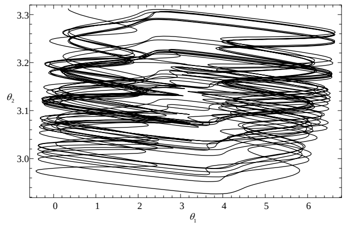

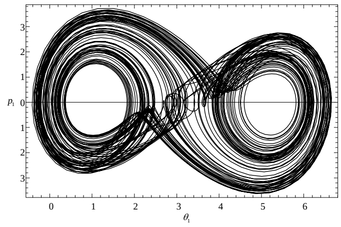

Fig.14. Phase portrait ($\tau = 0.7$) Fig.15. Phase portrait ($\tau = 0.7$)

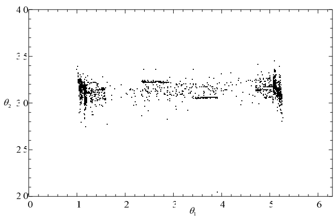

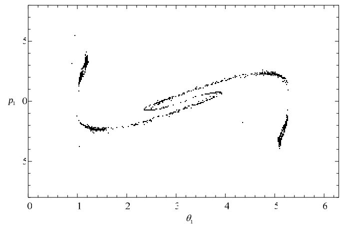

Fig.16. Poincare map ($\tau = 0.7$) Fig.17. Poincare map ($\tau = 0.7$)

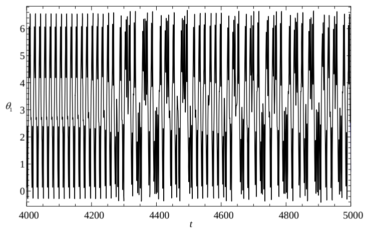

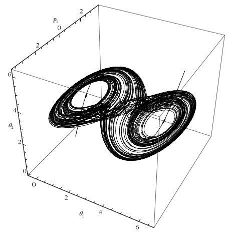

Fig.18. Time series ($\tau = 0.7$) Fig.19. Solution trajectory ($\tau = 0.7$)

4. Conclusions

In the present paper, a delay coupled flexible-joint robot arm is investigated and the geometric singular perturbation method is proved to be effective in dealing with such fast-slow systems with singularity. Geometric analysis reveals that the structure of the slow manifold directly determines the trends of the flow. Even a tiny variation of the structure will cause extremely different dynamics behaviors of the system. In this paper, such variation is brought about by the time delay. Simulation results indicate that with the increase of the time delay, the system can experience varied complex motions. The formation mechanisms of these dynamics behaviors are pictured on the basis of the slow manifold.

Acknowledgment

This work is supported by the State Key Program of National Natural Science Foundation of China under Grant No. 11032009 and Shanghai Leading Academic Discipline Project in No. B302.

References

[1] E. M. Izhikevich, Neural excitability, spiking and bursting, *International Journal of Bifurcation and Chaos*, Vol. 10, No. 6 (2000) 1171-1266.

[2] A. H. Nayfeh, *Perturbation methods*, New York: John Wiley & Sons, 1973.

[3] C. Jones, Geometric singular perturbation theory, *Lecture Notes in Math*, Vol. 1609 (1994) 45-118.

[4] S. Rinaldi, M. Scheffer, Geometric analysis of ecological models with slow and fast process, *Ecosystems*, 3 (2000) 507-521.

[5] Y. G. Zheng, Z. H. Wang, Time-delay effect on the bursting of the synchronized state of coupled Hindmarsh-Rose neurons, *Chaos*, 22 (2012) 043127-1-043127-6.

[6] M. W. Spong, Modeling and control of elastic joint robots, *Journal of Dynamic Systems, Measurement, and Control*, Vol. 109 (1987) 310-319.

[7] G. R. Chen, L. S. Shieh, On trajectory tracking of time-delayed systems with an application to flexible-joint robot arm, *Proceedings of the Conference on Control and Information*, 1995.

Energy Scalability of Dissipative Solitons in Presence of Quantum Noise

Vladimir L. Kalashnikov

Technical University of Vienna, Institute for Photonics, Gusshausstr. 25-29, A-1040 Vienna, Austria
(E-mail: kalashnikov@tuwien.ac.at)

Abstract. It is shown, that a dissipative soliton is strongly affected by a quantum noise, which confines its energy scalability. There exists some bifurcation point inside a soliton parametric space, where the energy scalability of dissipative soliton changes drastically so that an asymptotically unlimited accumulation of energy becomes impossible and the so-called "dissipaive soliton resonance" disappears.
Keywords: Dissipative soliton, Quantum noise, Dissipative soliton resonance.

1 Introduction

In the last decade, the concept of a dissipative soliton (DS), that is a strongly localized and stable structure emergent in a nonlinear dissipative system far from the thermodynamic equilibrium was actively developing and became well-established [1]. The unique feature of DS is its capability to accumulate the energy without stability loss [2]. As a result, the DS is energy-scalable. This phenomenon resembles a resonant enhancement of oscillations in environment-coupled systems so that it was proposed to name it as a "dissipative soliton resonance" (DSR) [3]. A capacity of DS to accumulate the energy is of interest for a lot of applications. For instance, it provides the energy scaling of ultra-short laser pulses and brings the high-field physics on table-tops of a mid-level university lab [4].

Nevertheless, the noise properties of DS remain practically unexplored. Such properties promise to be nontrivial because, as was found, the DS can contain the internal perturbation modes, which reveal themselves as the spectrum distortions and the peak power jitter [5]. Moreover, the parametric space of DS and, as a result, the DSR conditions can be modified substantively under action of gain saturation and another dynamic factors [6–8].

In this work, a numerical analysis of DS parametric space taking into account the quantum noise is presented. It is demonstrated, that the noise modifies the DS parametric space substantially and reduces the soliton energy scalability.

2 Concept of the DS and the DS parametric space

DS is a strongly localized and stable structure, which develops in a non-equilibrium system and, thus, has a well-organized energy exchange with an environment. This energy exchange forms a non-trivial internal structure of

DS, which provides the energy redistribution inside it (e.g., see [1]). In this respect, DS is a primitive analogue of cell.

One may think, that a simplest and, simultaneously, sufficiently comprehensive mathematical framework for a DS modeling is provided by the so-called nonlinear Ginzburg-Landau equation (NGLE) [9]. Here, we shall explore the NGLE with the cubic-quintic nonlinearity, which is appropriate, e.g., to modeling of the nonlinear optical and laser systems [10,11]:

$$\frac{\partial a\left(z,t\right)}{\partial z}=\left[-\sigma+\left(\alpha+i\beta\right)\frac{\partial^2}{\partial t^2}+\left(\kappa-i\gamma\right)\left|a\left(z,t\right)\right|^2-\kappa\zeta\left|a\left(z,t\right)\right|^4\right]a\left(z,t\right). \tag{1}$$

Here, $a(z,t)$ is a complex "field amplitude" describing the DS profile (e.g., it is a "slowly-varying" field amplitude for an optical DS or an effective "wave function" for a Bose-Einstein (BE) condensate [12]), t is a "local time" (that is a coordinate along which a DS is localized, e.g., it is a co-moving time-frame for an optical DS or a transverse spatial coordinate for a BE DS), z is a DS "propagation coordinate" (e.g., it is a number of cavity round-trips for a laser or a time for a BE condensate). The $\beta-$coefficient is a group-delay dispersion (GDD) coefficient (or a "kinetic-energy" term for a BE condensate), α is a squared inverse bandwidth of a spectral filter (e.g., it can be a squared inverse laser gain bandwidth or a "runaway" coefficient for a BE condensate). The $\gamma-$ coefficient defines a self-phase modulation (SPM) in a nonlinear optical system (a "strength" of three-bosons interaction), κ is a dissipative correction to it (a self-amplitude modulation (SAM) coefficient or a "strength" of boson creation in three-bosons interactions), and ζ is a higher-order correction to SAM coefficient. The $\sigma-$coefficient is a saturated net-loss coefficient, which defines the energy exchange with an environment (generally speaking, this exchange depends on the DS energy).

Only a sole analytical DS solution for Eq. (1) is known [10] but there are the powerful approximate techniques, which allow exploring the solitonic properties of NGLE [2]. These techniques demonstrate that a DS "lives" in the parametric space with reduced dimensionality. For instance, the DS of Eq. (1) has a two-dimensional parametric space [11] and its representation was called as the "DS master diagram" [2,11,13]. Such a diagram demonstrates some asymptotic corresponding to an infinite DS energy growth $E \to \infty$ (e.g., E can be associated with an ultrashort pulse laser energy or a mass of BE condensate). This asymptotic was named later as the DSR [3].

The structure of the master diagram is crucial for a DS characterization. The most interesting is the so-called "zero isogain curve", where $\sigma \equiv 0$ that corresponds to a "vacuum stability" of Eq. (1) and defines the DS stability border. Such a DS stability border obtained from the adiabatic theory of DS [2] is shown by the solid curve in Fig. 1. The DS is stable below this curve.

The dimensionless coordinates in Fig. 1 represent a true parametric space of DS and demonstrate the DSR existence: $\lim_{C\to 0.666} E = \infty$. Physically, the DSR corresponds to a perfect scalability of DS energy that is the DS energy can grow without a change of system parameters (i.e. parameters of Eq. (1)). Of course, the energy inflow is required for such a scaling. This inflow is

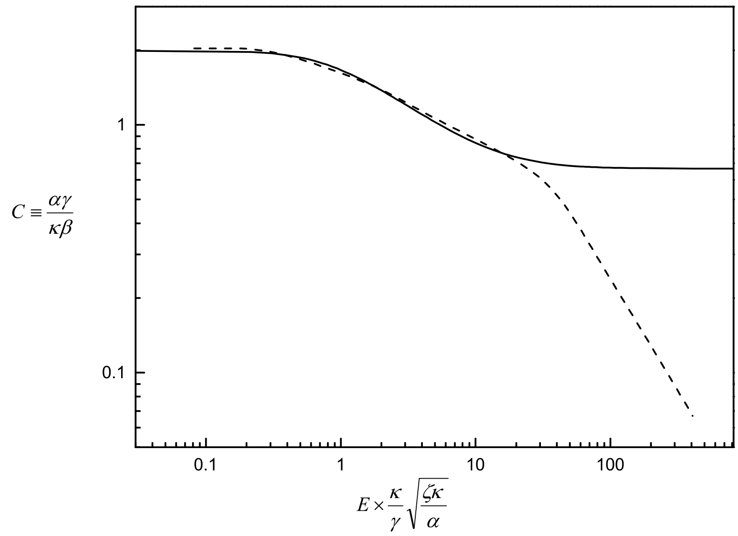

Fig. 1. Master diagram (parametric space) of DS. Solid curve corresponds to the soliton stability border obtained from the adiabatic theory. Dashed curve corresponds to the stability border with taking into account of the additive complex noise with the correlator: $\langle\psi(t)\psi(t')\rangle \equiv 10^{-5}\gamma^{-1}\delta\,(t-t')$.

provided by the energy-dependence of $\sigma-$parameter: $\sigma \equiv \xi\,(E/E' - 1)$ (here E' corresponds to the energy of a $t-$independent solution of Eq. (1); ξ is a parameter, which is irrelevant for a further consideration) [11].

3 Master diagram under the noise action

The inclusion of a quantum noise in the form of the additive complex white noise source ψ in Eq. (1) transforms the master diagram drastically. The dashed curve in Fig. 1 demonstrates the DS stability border in this case. One can see, that the DS stability conditions change after a bifurcation point $E\kappa^{3/2}\zeta^{1/2}/\gamma\alpha^{1/2} \approx 20$ so that the energy scaling needs a substantial decrease of the $C-$parameter (e.g., this corresponds to a substantial GDD-growth required for the DS stabilization). Thus, the DSR disappears under the noise action.

Moreover, the DS cannot develop from a noise after the next bifurcation point: $E\kappa^{3/2}\zeta^{1/2}/\gamma\alpha^{1/2} \approx 400$. Here, the noise amplification becomes so strong that the DS cannot rival it and a further energy scaling becomes impossible.

Another important feature of a high-energy DS in the presence of noise is that the soliton emergence is random, that is it depends on both a random sample of initial noise conditions and their evolution. Thus, the stability border for a high-energy DS becomes “fuzzy”.

4 Conclusion

The numerical analysis of NGLE has demonstrated that the DS energy scalability is affected strongly by a quantum noise. It has been found, that the noise destroys the DSR so that the soliton energy scaling requires a substantial GDD increase. Starting from some energy level, the noise prevents the DS formation at all that confines a reachable DS energy.

References

1.N.N. Akhmediev, A. Ankiewicz (Eds.). *Dissipative Solitons*, 2005. Berlin, Springer.
2.V.L. Kalashnikov. Chirped-Pulse Oscillators: Route to the Energy-Scalable Femtosecond Pulses. In H. Al-Khursan, editor, *Solid State Laser*, pages 145–184, 2012. InTech.
3.W. Chang, A. Ankiewicz, J. M. Soto-Crespo, N. Akhmediev. Dissipative soliton resonances. *Phys. Rev. A*, 78:023830, 2008.
4.T. Südmeyer, S.V. Marchese, S. Hashimoto, C.R.E. Baer, G. Gingras, B. Witzel, U. Keller. Femtosecond laser oscillators for high-field science. *Nature Photonics*, 2:599–604, 2008.
5.V.L. Kalashnikov. Dissipative Solitons: Perturbations and Chaos Formation. In C.H. Skiadas, I. Dimotikalis, C. Skiadas, editors, *Chaos Theory: Modeling, Simulations and Applications*, pages 199–206, 2011. World Scientific Publishing Co.
6.V.L. Kalashnikov. Chirped-pulse oscillators: an impact of the dynamic gain saturation. In arXiv:0807.1050 [physics.optics].
7.E. Ding, Ph. Grelu, J.N. Kutz. Dissipative soliton resonance in a passively mode-locked fiber laser. *Opt. Lett.*, 36: 1146–1148, 2011.
8.V.L. Kalashnikov. Dissipative Solitons: Structural Chaos and Chaos of Destruction. *Chaotic Modeling and Simulation*, 1:51–59, 2011.
9.I.S. Aranson, L. Kramer. The world of the complex Ginzburg-Landau equation. *Rev. Mod. Phys.*, 74:99–143, 2002.
10.N.N. Akhmediev, A. Ankiewicz. *Solitons: Nonlinear Pulses and Beams*, 1997. London, Chapman & Hall.
11.V.L.Kalashnikov, E.Podivilov, A.Chernykh, A.Apolonski. Chirped-pulse oscillators: theory and experiment. *Applied Physics B*, 83:503–510, 2006.
12.P.G. Kevrekidis, D.J. Frantzeskakis, R. Carretero-Gonzlez (Eds.). *Emergent Nonlinear Phenomena in Bose-Einstein Condensates*, 2008. Berlin, Springer.
13.V.L. Kalashnikov, Chirped dissipative solitons. In L.F. Babichev, V.I. Kuvshinov, editors, *Nonlinear Dynamics and Applications*, pages 58–67, 2010. Minsk.

Nonlinear reply of radon and deterministic chaos

Miraç Kamışlıoğlu[a], Fatih Külahcı[a], Fatih Özkaynak[b]

[a]Fırat University, Faculty of Science, Department of Physics, Nuclear Physics Division, Elazig, TR-23119, Turkey.
[b] Fırat University, Department of Software Engineering, TR-23119 Elazig, Turkey.
E-mails: m.kamislioglu@gmail.com ; fatihkulahci@firat.edu.tr

Abstract: Many studies have been achieved in applied sciences on the earthquake prediction by researchers. The chaotic non-linear structural behaviour of earthquakes is well known. In order to understand the formation of seismic activity it is extremely important to record the continuous measurements of the soil radon gas (^{222}Rn). In this study, 2976 data of ^{222}Rn are used and the chaotic time series analysis is applied to ^{222}Rn data from the soil. Chaos theory provides a structured explanation for irregular behavior of ^{222}Rn and gas anomalies in systems that are not stochastic. Lyapunov exponents and correlation dimension method are used to show the existence of chaos time series. Chaotic behavior of ^{222}Rn has been showed. Application of methodologies is achieved for Gölcük Region, İzmit, Turkey, where it is seismically very active.

Keywords: Chaotic time series analysis; Chaotic modeling; Radon measurement; Chaos analysis.

1. Introduction

^{222}Rn exists from the layers of Earth and is created by the uranium deposits source in nature. Certain soils and rocks especially contain high levels of uranium, which is natural deposit of radon. The uranium is rich in structures like granite, phosphate, shale and pitchblende. Relations between ^{222}Rn-earthquake and movement of ^{222}Rn in the Earth layers and in the atmosphere have been searched serious [1, 2, 3, 4 and 5]. ^{222}Rn has a half-life of 3.82 days and it is an α-emitting noble gas, which is produced in the radioactive decay series of ^{238}U. ^{222}Rn tends to migrate from Earth layers to the surface of the Earth. The migration rate of ^{222}Rn, which is non-linear, depends on many factors such as the dispersal of the uranium in the soil and bed rock, porosity of soil, humidity, micro cracks, granulation, and such [6].

Okabe [1956] has indicated radon as an earthquake precursor and radon changes in atmospheric near surface and showed a favorable correlation with seismic activities. On the other hand, anomalously high radon concentrations of ground water have been associated with fault lines [7]. Radon is easily soluble in water and it diffuses into the groundwater and spring waters.

High concentration of radon is often found in soils overlying highly fractured rocks such as fault lines. Radon emanation increases during an earthquake [8, 9]. Radon levels, which are correlated with meteorological and hydrological

data, and they are used successfully in the earthquake forecasting researches [10, 11].
In this study, 2976 data of the soil ^{222}Rn gas are used and the chaotic time series analysis by considerations of Lyapunov exponents and correlation dimension methods. The chaotic behavior of the ^{222}Rn concentration levels is determined. Finally, the results of the methodologies are achieved for Gölcük Region (Turkey).

2. Methodology and Research Area

The methodologies which are used in this study are based on the chaos theory. It is aperiodic long-term behavior in a deterministic system that exhibits sensitive dependence on initial condition and disorder behaves in an unexpected way [12]. Likewise, it depends on structure of the system as well as by certain parameters and is usually unstable, complex and non-linear systems are emerging [13].
Determination of the chaotic behavior in the natural events' behaviors is very difficult; therefore, chaos theory is a suitable tool to show the characteristic of the dynamical system.
The chaos methodologies are applied to data recorded at Gölcük Region located on the North Anatolian Fault Zone (NAFZ). ^{222}Rn data are recorded between from 01/05/2006 to 31/05/2006 dates. It is continuously measured from the soil at 15 min intervals for a month.

3. Results and Discussions

3.1. Chaotic Time Series Analysis

Chaotic time series are unpredictable systems. These systems contain large complexity. Prediction of non-linear time series is an available method to appraise characteristic of dynamical systems [14].
Chaotic time series analysis methods are most enforceable in cases where the data include nonlinearity. The first of these analysis methods is obtained as the degree of non-linear positive Lyapunov exponents [15].
If these methods display irregular or unpredictable behavior, then it is called chaotic. On the contrary, it is called non-chaotic. Fig. 1 shows the time series of chaotic behavior of ^{222}Rn data taken from Gölcük Region on NAFZ. Non-linear time series analysis starts from measured experimental time series of $x_1(t), x_2(t), \cdots, x_n(t)$, at n points. The same analysis provides various tools to determine the temporal structures embedded in the time series.

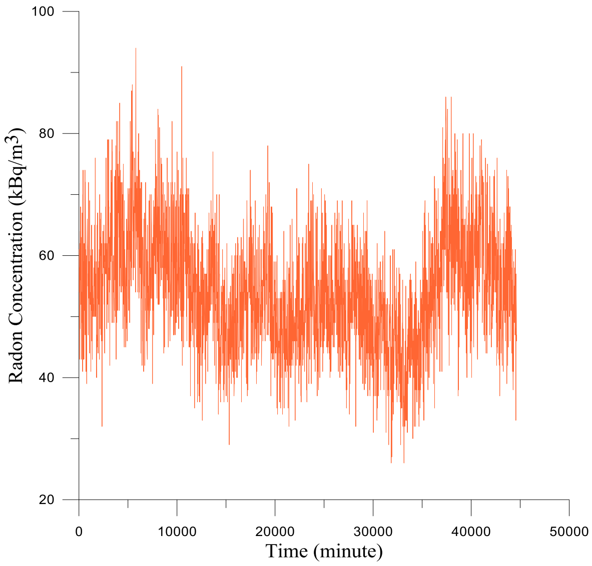

Fig. 1. Time series state variable for chaotic behavior

3.2. Lyapunov Exponent

Lyapunov exponents can be defined as the exponential increase or decrease of minor perturbations on an attractor. Largest Lyapunov exponent is one of the most practical methods to define chaotic behavior in a system [16]. The basis of Lyapunov exponent is very close to each other to monitor both the starting point, which is based on very different trajectories. Its sign gives information about the system dynamics. When exponential value is positive, system indicates chaotic behaviours. This condition, on initial conditions of the system, shows sensitive dependence [17]. The largest Lyapunov exponent can be anticipated in accordance with the algorithm Wolf et al. [18]. These applications are valid between neighboring points in the reconstructed phase space algorithm. In the following, the results have been shown concerning the maximum Lyapunov exponents (L_{max}), where $t \to \infty$, $d(0) \to \infty$ and $d(t)$, and hence, show the difference between two measurements. Largest Lyapunov exponent is calculated according to the following expression. The result is given for the ^{222}Rn data in Fig. 2.

$$L_{max} = \lim \left[\ln \left[\frac{d(t)}{d(0)} \right] \right], \tag{1}$$

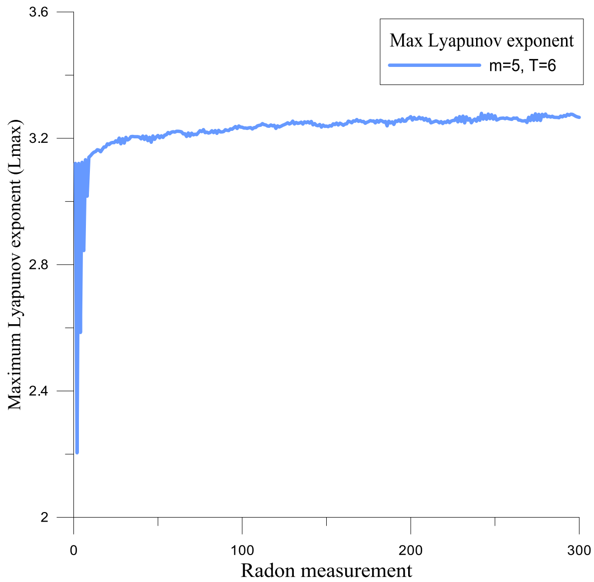

Fig. 2. Lyapunov exponent for ^{222}Rn (m: embedding dimension; τ: delay time)

3.3. Hurst Exponent

Hurst exponent is used to predict from time series [19]. Hurst exponent coefficient is an additional statistical measure necessary for the classification of time series. Hurst exponent calculation is explained also through the Rescaled range, R/S analysis, where R is the range of the accumulated data and S is the standard deviation. This exponent, H, can change between 0 and 1. Its calculation is possible from the discrete time series data set $\{x_t\}$ of dimension N by computing the mean, $\bar{x}(N)$ and standard deviation, $S(N)$ leading to,

$$\bar{x} = \frac{1}{N}\sum_{t=1}^{N} x_t \tag{2}$$

and

$$S(N) = \left[\frac{1}{N}\sum_{t=1}^{N}(x_t - \bar{x}(N))^2\right]^{1/2} \tag{3}$$

respectively. Range of cumulative departures of the data is given by $R(N) = \max\{X(n,N)\} - \min\{X(n,N)\}$

Finally, the Hurst exponent can be calculated as follows,

$$\langle R/S \rangle \cong (n)^H \tag{4}$$

If Hurst exponent is equal to 0.5, then it shows a random walk. A Hurst exponent between 0.5 and 1 proves the presence of chaos in the system. With the data at hand, it is computed as 0.56 for ^{222}Rn data from Eq. 4 and the results are given in Fig. 3.

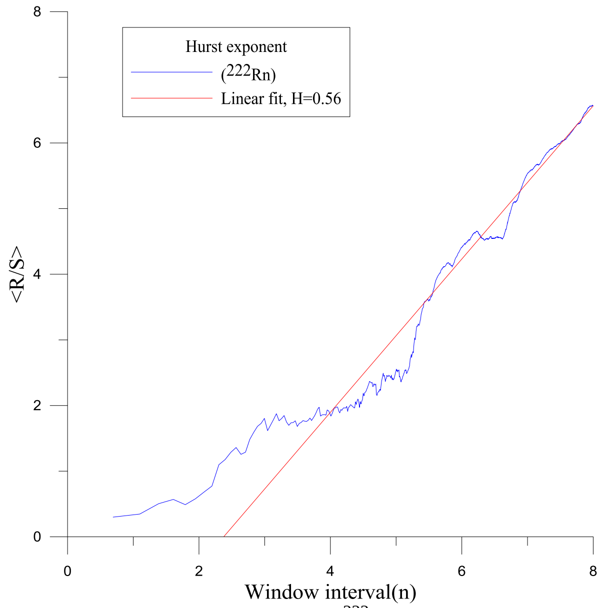

Fig.3. Plot of <R/S> for ^{222}Rn time series

3.4. Correlation Dimension

Correlation dimension is used to determine the degree of chaotic behaviour in a signal or time series. That is, correlation dimension, D_2, aids to determine whether a signal behaves like a random or chaotic distribution. The algorithm, measure of D_2 has presented by Grassberger- Procaccia [20]. These dimensions need to compute the correlation integral. Correlation integral function $C(r)$ can be defined as follows,

$$C(r) \approx \lim_{N\to\infty} \frac{1}{N^2}\left\{\left|x_i - x_j\right| \le r \textit{ the number of pairs } (i, j) \textit{ which statement}\right\} \tag{5}$$

$$C(r) = \lim_{N\to\infty} \frac{1}{N^2} \times \sum_{i=1}^{N} \sum_{j=i+1}^{N} H(\left|x_i - x_j\right| \le r\,) \tag{6}$$

The distance between two units with (such as, x_i and x_j) Euclidean definition can be computed as,

$$\left|x_i - x_j\right| = \sqrt{\sum_{k=1}^{m} (x_i(k) - x_j(k))^2} \tag{7}$$

H is the Heaviside step function, which can be expressed as follows.

$$H(x) = \begin{cases} 1, & x \geq 0, \\ 0, & x \leq 0, \end{cases} \tag{8}$$

If the system is chaotic, then D_2 will be the largest value. Kaplan and Yorke study showed correlation of Lyapunov exponents of information dimension [21]. D_2 can also be calculated as follows.

$$D_2 = \lim_{r \to 0} \frac{\log C(r)}{\log(r)} \tag{9}$$

In this study, one can draw $\log C(r)$ as a function of $\log(r)$ and compute D_2 from the slope of a linear fit. Embedding dimensions corresponding to the correlation dimensions for a period of chaotic deterministic process are shown in Figure 4. Also, for ^{222}Rn correlation dimension, D_2, is given in Fig. 4. Time scale of dynamical system is similar to the D_2 values' mutual predictions. Values of the embedding dimension are given resource about the change of $C(r)$.

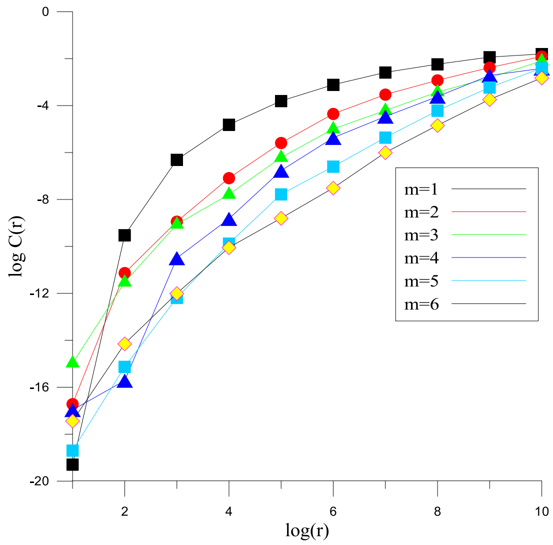

Fig. 4. The estimate of correlation dimension for ^{222}Rn time series

4. Conclusions

Natural and geophysical observations are not regular usually. Chaotic analyses are useful tools to describe the natural irregularity. In this study, they are used as chaotic methods. The non-linear behaviour of ^{222}Rn in the Earth layers is showed. The chaos methodologies in order to show non-linear behaviour of

^{222}Rn are applied to ^{222}Rn data taken from the Gölcük Region on the North Anatolian Fault Line. The soil ^{222}Rn gas, which propagates from the fault lines, has a nonlinear characteristic.

Acknowledgements

This research is supported by Republic of Turkey Prime Ministry Disaster & Emergency Management Presidency (AFAD). We especially would like to thank Dr. Murat Nurlu and Bengi Eravcı from AFAD and Prof.Dr. Zekâi Şen from İstanbul Technical University for support and encouragement.

References

1. A.B. Tanner. Physical and chemical control on distribution of radium-226 and radon-222 in ground water near Great Salt Lake, Utah, in The Natural Radiation Environment, edited by J: A. S. Adams and W. M. Lowder, pp. 253-276, University of Chicago Pres, Chicago,1964.
2. S. Uyeda, T. Nagao, M. Kamogawa. Short-term earthquake prediction: Current status of seismo-electromagnetics. Tectonophysics vol. 470, pp. 205-213, 2009.
3. H.S. Virk, B. Singh. Radon anomalies in soil gas and groundwater as earthquake precursor phenomena. Tectonophysics vol. 227, pp. 215–224, 1993.
4. M. Trique, P. Richon, F. Perrier, et al. Radon emanation and electric potential variations associated with transient deformation near reservoir lakes. Nature vol. 399, pp. 137-141, 1999.
5. J. Planinić, V. Radolić, B. Vuković. Radon as an earthquake precursor. Nucl Instrum Methods vol. 530, pp. 568-574, 2004.
6. M.H. Al-Tamimi and K.M. Abumurad. Radon anomalies along faults in North of Jordan. Radiat. Measur., vol. 34, pp. 397-400, 2001.
7. M.M. Moussa, A. –G.M. El Arabi. Soil radon survey for tracing active fault: a case study along Qena-Safaga roadCC Eastern Desert, Egypt. Radiat. Meas. vol. 37, pp.211-216, 2003.
8. V.I. Ulumov, B.Z. Mavashev. Forerunners of the Tashkent earthquake. Izv. Akad. Nauk Uzb. SSR, pp 188-200, 1971.
9. G. Igarashi, S. Saeki, N. Takahata, K. Sumikawa, S. Tasaka, Y. Sasaki, M. Takahashi, Y. Sano. Ground-water radon anomaly before the Kobe earthquake in Japan, Science, vol. 269, pp. 60–61,1995.
10. F. Külahcı, M. İnceöz, M. Doğru, E. Aksoy, and O. Baykara. Artifical neural network model for earthquake prediction with radon monitoring. Appl. Radiat. Isot., vol. 67, pp. 212-219, 2009.
11. C.Y. King. Radon monitoring for earthquake prediction in China. Earthquake Pred. Res. vol. 3, pp. 47-68, 1985.
12. G.L. Baker, J.P. Gollub. Chaotic Dynamics an Introduction, Cambridge University Press, 1990.
13. K. Giannakopoulos, T. Deliyannis, J. Hadjidemetriou. Means for Detecting Chaos and Hyperchaos in Nonlinear Electronic Circuits,. DSP vol.2, pp. 951-954, 2002.

14. J. Zhang, K.F. Man. Time series prediction using recurrent neural network in multi-dimension embedding phase space. IEEE International Conference on System, Man, and Cybernetics vol. 2, pp. 11-14, 1998.
15. I. Matsuba. Nonlinear time series analysis, Asakura, 2000.
16. C. Frazier, K.M. Kockelman. Chaos Theory & Transportation Systems: an Instructive, Transportation Research Record vol. 1897, pp. 9-17, 2004.
17. A.B. Özer, E. Akın, Tools for Detecting Chaos, SAÜ Inst. Science Magazine, vol. 9, pp. 60-66, 2005.
18. A. Wolf, et al. Determining Lyapunov exponents from a time series. Phys D, vol. 16, pp.285-317, 1985.
19. C.M. Harris, R.W. Todd, S.J. Bungard, R.W. Lovitt, J.G. Morris, D.B. Kell. The dielectric permittivity of microbial suspensions at radio- frequencies: a novel method for estimation of microbial biomass, Enzyme Microbial Technology. vol. 9, pp. 181-186, 1987.
20. P. Grassberger, I. Procaccia. Characterization of strange attractors. Phys. Rev. Lett. vol. 50, pp. 346-349, 1983.
21. J. Kaplan, J. Yorke. Fuctional Differential Equations and the Approximation of Fixed Points. Lecture Notes in Mathematics, No 730, Berlin: Springer Verlag, 1979.

Influence of geomagnetic activity on recurrence quantification indicators of human electroencephalogram

I.E. Kanunikov, B.V. Kiselev

Saint-Petersburg State University, Russia
E-mail: igorkan@mail.ru

Abstract: The investigation deals with the revealing of influence of a geomagnetic field on human electroencephalogram by means of recurrence quantification analysis (RQA). The EEG base of 10 subjects was processed. The database included electroencephalogram records carried out from 16 points under three background conditions. Each subject took part in 15–50 experiments. EEG was registered from frontal, temporal, central, parietal and occipital areas of the left and right hemispheres. For every subject for each of 16 points of EEG registration 9 recurrent measures of EEG were calculated (RR, DET, L, DIV, ENTR, RATIO, LAM, TT, CLEAN). Then the factor of correlation of these measures with a planetary index of geomagnetic activity of Ap and local daily K-index in a day of carrying out experiment was calculated. As a result of this research the following conclusions were received.
1. Significant influence of intensity of a geomagnetic field on recurrent EEG dynamics indicators is shown. Thus the relationship between recurrent EEG measures and indexes of local intensity of a geomagnetic field appeared higher than with planetary indexes.
2. Existence of significantly bigger number of relations between geomagnetic activity and recurrent measures of the left hemisphere EEG is shown.
3. The conclusion suggests that the geomagnetic field makes the main impact on a chaotic component of EEG.
Keywords: Nonlinear methods, Recurrance quntification analysis, Electroencephalogram, Geomagnetic field, Magnitobiology.

1. Introduction

The investigation deals with the revealing of influence of a geomagnetic field on human electroencephalogram by means of recurrence quantification analysis (RQA). In contrast with chaos method, an important advantage of RQA is that it can deal with a noisy and short time series.

2. Methods and experiments

Recurrence Plots are introduced by Eckmann et. al. (1987) as a tool for visualization of recurrence of states Xi in phase space. This approach enables us to investigate the m-dimensional phase space through a two-dimensional representation of its recurrences.

Zbilut and Webber (1992, 1994) developed RQA for definition of numerical indicators. They offered the measures using density of recurrent points and diagonal structures of the diagram: indicator of similarity (RR), determinism (DET), maximum length of diagonal lines (L), the maximal length of diagonal structures or its inversion — the divergence (DIV), entropy (ENTR), the ratio between DET and RR (RATIO). Slightly after Marwan et.al. (2004, 2007) offered the measures based on horizontal (vertical) structures of recurrent diagrams: laminarity (LAM) and indicator of a delay (TT). V.B.Kiselev (20007) suggests the indicator CLEAN which shows influence of a stochastic component of process, thus prevalence of the stochastic component leads to increase of CLEAN value.

Expressions for RQA measures are shown below.

The simplest measure of the RQA is the recurrence rate (RR) or percent recurrences which is a measure of the density of recurrence points in the recurrent points. Note that it corresponds to the definition of the correlation sum.

The ratio of recurrence points that form diagonal structures (of at least length lmin) to all recurrence points is introduced as a measure for determinism (DET*)* (or predictability) of the system. The threshold lmin excludes the diagonal lines which are formed by the tangential motion of the phase space trajectory.

L is the average time that two segments of the trajectory are close to each other. This measure can be interpreted as the mean prediction time.

Another RQA measure considers the length Lmax of the longest diagonal line found in the recurrent points, or its inverse, the divergence, DIV=1/Lmax. These measures are related to the exponential divergence of the phase space trajectory. The faster the trajectory segments diverge, the shorter are the diagonal lines and the higher is the measure DIV.

ENTR refers to the Shannon entropy of the frequency distribution of the diagonal lines lengths. This measure reflects the complexity of the deterministic structure in the system.

RATIO is the ratio between DET and RR. This measure is useful to discover transitions when RR decrease and DET does not change at the same time.

LAM is analogous to the definition of determinism. This measure is the ratio between the recurrence points forming the horizontal structures and the entire set of recurrence points. The computation of LAM is realized for horizontal line length that exceeds a minimal length v_{min}.

TT shows average length of laminar states in the system.

In periodical systems fluctuations and noise influence leads in separate points and very short diagonals. The measure *cleanness* (CLEAN) is the ratio between recurrence points in diagonals with lengths less than l_{min} and recurrence points in diagonal lines with lengths equal or more than l_{min}. The measure quantifies influence of noise and fluctuations on system trajectory and should be used if studied system shows periodic behavior.

In this work the EEG base of ten clinically normal subjects (six males and four females in the age range 20– 65 years) was processed. The database included records of electroenchephalogram, carried out from 16 sites under three background conditions: two with open eyes and one with close eyes. During background condition with open eyes subject has to look passively at a picture or thumb through the book. During close eyes subject has to consider drops which were modelled by phonostimulator. In our opinion such simple activity more will balance subjects with each other in comparison with a standard background condition at which it is impossible to check internal state of the subject.

Each subject took part in 20-50 experiments which are carried out to the period of time from half a year till two years. Registration of EEG was carried out in the international system 10/20 in frontal (Fp1, Fp2, F3, F4, F7, F8), temporal (T3, T4, T5, T6), central (C3,C4), parietal (P3, P4) and occipital (O1, O2) sites of the left and right hemispheres. The length of record EEG was about 1 minutes for each of three backgrounds, EEG was quantized with frequency of 250 times a second. The constant of time was 0.3 seconds, and the top frequency of a cut equaled 30 Hz.

3. Results

Before data processing all records were filtrated to escape EEG from different artifacts. For every subject for each of 16 sites and the 3rd background conditions 9 recurrent measures of EEG were calculated (RR, DET, L, DIV, ENTR, RATIO, LAM, TT, CLEAN). Then the coefficient of correlation of these measures with an index of geomagnetic activity was calculated. The coefficient of correlation was calculated on two rows: one row corresponded to defined EEG indicator, and the second – represented values of an index of geomagnetic activity in day of carrying out experience.

As a result of carrying out one experiment about 500 values of recurrent measures (9x16x3) turned out. Two geomagnetic indexes were thus used: planetary Ap and local daily K-index which undertook from a site of the Finnish observatory (Sudancula). At calculation of coefficients of correlation with an index of geomagnetic activity value of correlation were averaged on three background conditions. Tests were significant at $P < 0.05$.

At the first analysis stage significant correlations of 9 recurrent measures of EEG were compared with indexes of planetary and local geomagnetic activity. It appeared that all measures significantly correlated with geomagnetic activity. Total number of significant interrelations for all 10 subjects made in relation to a planetary index was 271, and in relation to a local indicator - 347. Considering that fact that the local index of geomagnetic activity was more sensitive to recurrent EEG measures in comparison with a planetary index, in further calculations it was used only. Thus the maximum quantity of correlations made 44 (for an indicator of DIV), and the minimum number equaled 32 (for a TT indicator). Statistically significant distinctions between quantity of correlations for each of measures it was revealed not. On this basis in the subsequent analysis data on all measures were averaged.

In table 1 are submitted data by number of statistically significant coefficients of correlation between recurrent measures of EEG and local K-indexes of geomagnetic activity. First, the fact of individual differences in number of correlations which are in range from 14 to 57 attracts attention.

Table 1. Quantity of significant correlations of recurrent measures of EEG with local K-index

Subjects	RR	DET	L	DIV	ENTR	RATIO	LAM	TT	CLEAN	Summa
1	5	4	5	7	5	7	4	5	4	46
2	2	1	4	4	3	1	1	3	0	19
3	11	4	2	8	7	7	9	1	8	57
4	2	2	1	2	1	1	3	0	2	14
5	1	4	3	3	3	4	2	4	4	28
6	4	5	7	9	8	3	3	5	3	47
7	1	5	2	5	3	4	8	3	5	36
8	4	8	5	1	5	2	6	5	7	43
9	1	5	5	4	6	7	4	5	5	42
10	3	1	1	1	1	3	1	1	2	14
Summa	34	39	35	44	42	39	41	32	40	346

The second interesting result consisted that all recurrent measures were characterized by a large amount of correlations for EEG of the left hemisphere in comparison with right. However statistically significant differences took place only for DET measure (P <0.02). As a whole, when averaging all 9 recurrent EEG measures differences between the left and right hemisphere were statistically high-significant (P <0.001).

At the following analysis stage interhemisphere differences of coefficients of correlation for each pair of sites (tab. 2) were considered. Except for pair of sites of C3 and C4 where in the right hemisphere the quantity of correlations was higher, than in left, and in T5, T6 sites where it was equal, in all other pairs of EEG sites the number of correlations at the left was higher than in right. However statistically significant difference was observed only between temporal sites T3 and T4.

Table 2. Quantity of significant correlations of 9 recurrent measures of EEG in different sites with local K-index of geomagnetic activity (data were avaraged on 10 subjects)

C3	C4	F3	F4	F7	F8	Fp1	Fp2
24	34	16	14	22	12	37	19

O1	O2	P3	P4	T3	T4	T5	T6
32	21	10	6	35	12	26	26

Research of changes of classical rhythms EEG (α, β, θ) in reply to changes of a geomagnetic field hasn't revealed significant interrelations with K index. On the other hand primary not filtered signal EEG has revealed such relationship.

4. Discussion

The fact of existence of a large number of correlations between various recurrent EEG measures and index of geomagnetic activity appeared the most important. It testifies that the nonlinear component of EEG for which analysis the RQA method was used, is very sensitive to changes of a geomagnetic field. Carruba et.al. (2007) show that magnetosensory evoked potentials weren't detected when the EEGs were analyzed by time averaging, indicating that the evoked potentials were nonlinear in origin. Obviously, the geomagnetic field influences electric activity of a brain in a nonlinear way. This fact can cause failures in search of reflections in EEG of influences from a geomagnetic field.

That fact that a local index was more closely connected with recurrent EEG measures in comparison with a planetary index is explained by that a local index more precisely, in comparison with planetary, reflects a condition of a geomagnetic field in St. Petersburg being on close longitude.

The fact of very high individual differences found in work concerning quantity of correlations of various recurrent EEG measures with geomagnetic activity, was explained obviously, existence of individual differences concerning sensitivity of subjects to influence on the central nervous system of changes of a geomagnetic field. It should be noted that subjects differed concerning that what by sites EEG significantly correlated with indicators of geomagnetic activity. At the 4th of 10 subjects correlated mainly frontal and temporal sites, at 4 subjects significant correlations were observed practically for all sites, at 2 subjects correlated either frontal, or temporal sites. Similar individual differences were observed in the work of Carruba et.al. (2007). They show that magnetosensory evoked potentials so strongly differ at various subjects that when the results obtained within subjects were averaged across subjects, evoked potentials couldn't be detected.

The most interesting fact concerns high-significant differences concerning number of correlations with recurrent EEG measures of the left and right hemispheres. This result based on a tendency to excess of number of correlations with every recurrent measures of the left hemisphere in comparison with right, and on the high-significant difference received at averaging of all recurrent measures of EEG. The question of why the bigger number of EEG sites of the left hemisphere correlates with changes of a geomagnetic field, remains open. We know that the right hemisphere is closely connected with adaptation processes. So, for example, V.P. Leutin and E.I.Nikolayeva (1988) on the basis of numerous experimental studies drew a conclusion that right brain hemisphere activation is decisive factor, providing adaptation to extreme climate conditions. In our experiments devoted to studying of influence of a geomagnetic field on an indicator of spatial synchronization of EEG, it was shown that in reply to changes of a geomagnetic field activation of the right hemisphere authentically increases. We connected this result with the stress reaction caused by changes of a geomagnetic field.

In the real experiments more sensitive in relation to variations of a geomagnetic field there was a nonlinear component of EEG of the left hemisphere. The understanding of this result will require further researches.

5. Conclusions

As a result of this research the following conclusions were received.

1. Significant influence of intensity of a geomagnetic field on recurrent EEG dynamics indicators is shown. Thus the relationship between recurrent EEG measures and indexes of local intensity of a geomagnetic field appeared higher than with planetary indexes.
2. Existence of significantly bigger number of relations between geomagnetic activity and recurrence measures of the left hemisphere EEG is shown.
3. The conclusion suggests that the geomagnetic field makes the main impact on a chaotic component of EEG.

References

1. Carrubba S., Frilot C., Chesson A.L., MarinoA.A. Evidence of a nonlinear human magnetic sense //Neuroscience 144, 2007, 356–367.
2. Eckmann J.P., Kamphorst S. O., Ruelle D. Recurrence Plots of Dynamical Systems // Europhysics Letters 5, 1987, pp. 973–977.
3. Kanunikov I.E. et.al. Vlijanie geomagnitnoi aktivnosti na electroencephalogrammu cheloveka (Влияние геомагнитной активности на электроэнцефалограмму человека) // Ekologia cheloveka. 2010. №6. P.6-11.
4. Kiselev V.B. Opredelenie stabilnosti traectorii prozessa v phazovom prostransntve pri pomochi recurrentnogo analisa (Определение стабильности траектории процесса в фазовом пространстве при помощи рекуррентного анализа)// Nauchno-tecnicheski vestnik SPbUITMO. SPb.: SPbUITMO, 2007, vip.20. P.121-130.
5. Leutin V.P., Nikolaeva E.I. Psychofisiologicheskie mechanismi adaptazii i funkzionalnaja asimmetria mozga (Психофизиологические механизмы адаптации и функциональная асимметрия мозга) Novosibirsk, Nauka SO. - 1988. - 192 p.
6. Marwan N., Romano M.C., Thiel M., Kurths J. Recurrence plots for the analysis of complex systems// Physics Reports 438, 2007, 237–329.
7. Marwan N., Meinke A. Extended Recurrence Plot Analysis and its Application to ERP Data // International Journal of Bifurcation and Chaos “Cognition and Complex Brain Dynamics” 14 (2), 2004.
8. Webber Jr. C. L., Zbilut J. P. Dynamical assessment of physiological systems and states using recurrence plot strategies // Journal of Applied Physiology 76 (2), 1994, pp. 965–973.
9. Zbilut J.P., Webber Jr.C.L. Embeddings and delays as derived from quantification of recurrence plots // Physics Letters A 171 (3–4). 1992. pp. 199–203.

Proceedings, 6th Chaotic Modeling and Simulation International Conference
11 - 14 June 2013 Istanbul, Turkey

On a Topological Problem of Strange Attractors

Ibrahim Kirat[1] and Ayhan Yurdaer[2]

[1] Department of Mathematics, Istanbul Technical University, 34469 Maslak, Istanbul, Turkey
(E-mail: ibkst@yahoo.com)

[2] Department of Mathematics, Istanbul Technical University, 34469 Maslak, Istanbul, Turkey
(E-mail: yurdaerayhan@itu.edu.tr)

Abstract. In this note, we consider self-affine attractors that are generated by an expanding $n \times n$ matrix (i.e. all of its eigenvalues have moduli > 1). Here we concentrate on the problem of connectedness. Although, there has been intensive study on the topic recently, this problem is not settled even in the one-dimensional case. We focus on some basic attractors, which have not been studied fully, and characterize connectedness.

Keywords: Self-affine attractors, Self-affine tiles, Connectedness.

1 Introduction

Let $S_1, ..., S_q$, $q > 1$, be contractions on $\mathbb{R}^n$, i.e., $||S_j(x) - S_j(y)|| \leq c_j||x - y||$ for all $x, y \in \mathbb{R}^n$ with $0 < c_j < 1$. Here $|| \cdot ||$ stands for the usual Euclidean norm, but this norm may be replaced by any other norm on $\mathbb{R}^n$. It is well known [4] that there exists a unique non-empty compact set $F \subset \mathbb{R}^n$ such that

$$F = \bigcup_{j=1}^{q} S_j(F).$$

Let $M_n(\mathbb{R})$ denote the set of $n \times n$ matrices with real entries. We will assume that

$$S_j(x) = T^{-1}(x + d_j), \quad x \in \mathbb{R}^n,$$

where $d_j \in \mathbb{R}^n$, called *digits*, and $T \in M_n(\mathbb{R})$. Then F is called a *self-affine set* or a *self-affine fractal*, and can be viewed as the invariant set or the attractor of the (affine) *iterated function system* (IFS) $\{S_j(x)\}$ (in the terminology of dynamical systems). Let $M_n(\mathbb{Z})$ be the set of $n \times n$ integer matrices. Further, if $D := \{d_1, ..., d_q\} \subset \mathbb{Z}^n$ and $T \in M_n(\mathbb{Z})$, it is called an *integral self-affine set* and we will primarily consider such sets in this paper. If, additionally, $|\det(T)| = q$ and the integral self-affine set F has positive Lebesgue measure, then F is called an *integral self-affine tile*. We sometimes write $F(T, D)$ for F to stress the dependence on T and D. For such tiles, the positivity of the Lebesgue measure is equivalent to having nonempty interior [2].

There is a demand to develop analysis on fractal spaces, in order to deal with physical phenomena like heat and electricity flow in disordered media, vibrations of fractal materials and turbulence in fluids. Without a better understanding of the topology of fractals, this seems to be a difficult task. There is a growing literature on the formalization and representation of topological questions; see [3] for a survey of the field.

One of the interesting aspects of the self-affine sets is the *connectedness*, which roughly means the attractor cannot be written as a disjoint union of two pieces. This property is important in computer vision and remote sensing [8,20]. We mention that connected self-affine fractals are curves; thus, they are sometimes referred to as self-affine curves [10]. There is some motivation for studying connected self-affine tiles because they are related to number systems, wavelets, torus maps. Recently, there have been intensive investigations on the topic by Kirat and Lau [12,10], Akiyama and Thuswaldner [1,16], Ngai and Tang [18,19] and Luo et al. [16,15].

In this note, we consider planar integral self-affine fractals obtained from 2×2 integer matrices with reducible characteristic polynomials, and report our findings on their connectedness. However, our considerations can be generalized to higher dimensions. As for the organization of the paper, in Section 2, we deal with special cases and state some simple, but non-conventional techniques to check the connectedness. In literature, most of the papers on the connectedness have some restrictions on the digit set. Here our aim is to remove such restrictions in Section 3.

2 Some Non-Conventional Techniques

Usually, connectedness criteria were given by using a "graph" with vertices in D [6,12]. In this section, we present graph-independent techniques to check the connectedness or disconnectedness. Throughout the paper, T^{-1} is a contraction. Let $\#D$ denote the number of elements in D. We first recall a known result.

Proposition 1. *[12] Suppose $T = [\pm q]$ with $q \in \mathbb{N}$, and $D \subseteq \mathbb{R}$ with $\#D = q$. Then $F(T, D)$ is a connected tile if and only if, up to a translation, $D = \{0, a, 2a, ..., (q-1)a\}$ for some $a > 0$.*

As one may notice q and D are not arbitrary in Proposition 1 since $q \in \mathbb{N}$ and $\#D = q$. By using the approach in [9,11], we can remove such restrictions. For that purpose, we consider the convex hull of F and denote it by K. Also let $K_1 = \bigcup_{j=1}^{q} S_j(K)$. Then we have the following.

Proposition 2. *Let $D = \{0, d_2 v, \cdots, d_q v\} \subset \mathbb{R}^n$ with $v \in \mathbb{R}^n \setminus \{0\}$ and $T = pI$, where $p \in \mathbb{R}$ and I is the identity matrix. Then $F(T, D)$ is connected if and only if $K = K_1$.*

Remark 1. A digit set D as in Proposition 2 is called a *collinear* digit set. It is easy to check the condition $K = K_1$ in the proposition because K is a closed interval. If $T = \pm 2I$, then $F(T, D)$ is connected for any digit set. A famous example of this type is the Sierpiński tile (see Figure 1), for which $T = 2I$ and $D = \{d_1 = \left[\begin{smallmatrix}0\\0\end{smallmatrix}\right], d_2 = \left[\begin{smallmatrix}1\\0\end{smallmatrix}\right], d_3 = \left[\begin{smallmatrix}0\\1\end{smallmatrix}\right], d_4 = \left[\begin{smallmatrix}-1\\-1\end{smallmatrix}\right]\}$.

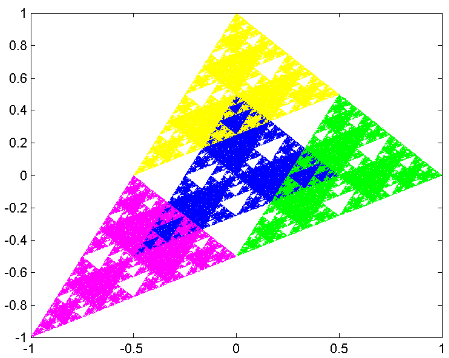

Fig. 1. The Sierpiński tile

The disconnectedness of $F(T, D)$ was studied in [13]. Here we want to mention another non-conventional sufficient condition for disconnectedness. In the rest of the paper, we study attractors $F(T, D)$ in the plane such that $T \in M_2(\mathbb{Z})$ has a reducible characteristic polynomial. From [10], we know that such matrices are conjugate to one of the following lower triangular matrices

$$\begin{bmatrix} n & 0 \\ t & m \end{bmatrix}, \qquad \text{where } |n| \geq |m|, \text{ and } t = 0 \text{ or } t = 1. \tag{1}$$

We also let

$$S = \{\left[\begin{smallmatrix} i \\ j \end{smallmatrix}\right] : 0 \leq i \leq |n| - 1,\ 0 \leq j \leq |m| - 1\}.$$

The attractors of the next proposition can be considered as a generalization of Sierpiński carpets [17]. Let $dim_S(F)$ be the *singular value dimension* of F (see [5]). We call a collinear digit set D with v is an eigenvector of T *eigen-collinear*. In that case, F is a subset of a line segment. By using Corollary 5 in [5], we obtain the following.

Proposition 3. *Assume that T is as in (1), $D \subset S$, and D is not eigen-collinear. Then $F(T, D)$ is disconnected if $\log_{|m|} r + \log_{|n|}(\frac{q}{r}) \neq dim_S(F)$, where $q = \#D$ and r is the number of j so that $\left[\begin{smallmatrix} i \\ j \end{smallmatrix}\right]$ for some i.*

Remark 2. It is easy to check the sufficient condition for the attractors $F(T, D)$ in Proposition 3 because, in that case,

$$dim_S(F) = \begin{cases} 1 + \log_{|n|}(\frac{q}{|m|}) & \text{if } |m| < q \leq |mn|, \\ \log_{|m|} q & \text{if } q \leq |m| \end{cases}$$

3 General Digit Sets

In this section, we will present a practical way of checking the connectedness of $F(T, D)$ with T as in (1) and $D \subset \mathbb{Z}^2$. Note that it is enough to consider the case $n, m > 0$, since $F(T, D) = F(T^2, D + TD)$. By translating D, we will assume that D has nonnegative entries. Let $\mathcal{N} = (F - F) \cap \mathbb{Z}^2$. Set

$$\Delta D = D - D, \quad a_1 = \left[\begin{smallmatrix} n-1 \\ 1 \end{smallmatrix}\right], \quad a_2 = \left[\begin{smallmatrix} 0 \\ m-1 \end{smallmatrix}\right], \quad a_3 = \left[\begin{smallmatrix} n-1 \\ m-1 \end{smallmatrix}\right], \quad b_1 = \left[\begin{smallmatrix} n-1 \\ 0 \end{smallmatrix}\right],$$

$$e_1 = \left[\begin{smallmatrix} 1 \\ 0 \end{smallmatrix}\right], \ e_2 = \left[\begin{smallmatrix} 0 \\ 1 \end{smallmatrix}\right], \ e_3 = \left[\begin{smallmatrix} 1 \\ 1 \end{smallmatrix}\right], \ e_4 = \left[\begin{smallmatrix} 1 \\ -1 \end{smallmatrix}\right].$$

First, we begin with the special class of fractals F in Proposition 3, where $D \subset S$.

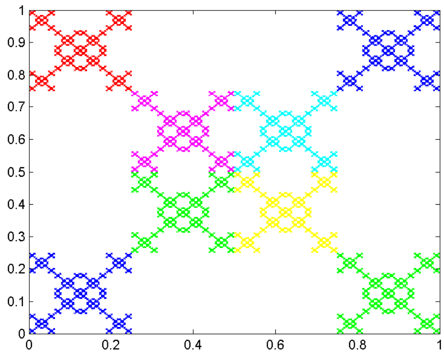

Fig. 2.

Proposition 4. *Assume that F is as in Proposition 3, $t = 1$ and $n, m > 0$. Then*

(i) if $a_1, a_2 \notin \Delta D$, then F is disconnected,

(ii) otherwise,

(I) $\mathcal{N} = \{\pm e_i \mid i \in \{1, 2\} \text{ and } a_i \in \Delta D\}$ when only one of a_1, a_2 is in ΔD,

(II) $\mathcal{N} = \{\pm e_1, \pm e_2\}$ when $a_1, a_2 \in \Delta D$ and $0 \notin D$,

(III) $\mathcal{N} = \{\pm e_1, \pm e_2, \pm e_4\}$ when $a_1, a_2 \in \Delta D$ and $0 \in D$.

Proposition 5. *Assume that F is as in Proposition 3, $t = 0$ and $n, m > 0$. Let $b_2 = a_2$, $b_3 = a_3$. Then*

(i) if $b_1, b_2, b_3 \notin \Delta D$, then F is disconnected,

(ii) otherwise,

(I) $\mathcal{N} = \{\pm e_i \mid i \in \{1, 2, 3\} \text{ and } b_i \in \Delta D\}$ when only one of b_1, b_2, b_3 is in ΔD,

(II) $\mathcal{N} = \{\pm e_i \mid \ i \in \{1, 2, 3\} \text{ and } b_i \in \Delta D\}$ when $b_1, b_2 \in \Delta D$ and $0 \notin D$,

(III) $\mathcal{N} = \{\pm e_i \mid \ i \in \{1, 2, 3\} \text{ and } \mathrm{b_i} \in \Delta \mathrm{D}\} \cup \{\pm e_4\}$ when $b_1, b_2 \in \Delta D$ and $0 \in D$.

For a digit set D, an *s-chain* (in D) is a finite sequence $\{d_1, ..., d_s\}$ of s distinct vectors in D such that $d_i - d_{i+1} \in \mathcal{N}$ for $i = 1, ..., s - 1$. Then we can put the connectedness criterion in [12] into the following form.

Proposition 6. *F is connected if and only if, by re-indexing D (if necessary), D forms a q-chain.*

Remark 3. In view of Proposition 4 and Proposition 5, Proposition 6 is quite feasible. That is, the connectedness can be decided by a simple inspection of D using $\mathcal{N}$ in Propositions 4-5. That is, we get a graph-independent way of checking the connectedness. An example is given in Figure 2, for which $T = 4I$ and $D = \{d_1 = \left[\begin{smallmatrix}0\\0\end{smallmatrix}\right], d_2 = \left[\begin{smallmatrix}1\\1\end{smallmatrix}\right], d_3 = \left[\begin{smallmatrix}2\\2\end{smallmatrix}\right], d_4 = \left[\begin{smallmatrix}3\\3\end{smallmatrix}\right], d_5 = \left[\begin{smallmatrix}2\\1\end{smallmatrix}\right], d_6 = \left[\begin{smallmatrix}1\\2\end{smallmatrix}\right], d_7 = \left[\begin{smallmatrix}0\\3\end{smallmatrix}\right], d_8 = \left[\begin{smallmatrix}3\\0\end{smallmatrix}\right]\}$.

We now consider the general case $D \subset \mathbb{Z}^2$. Let

$$\mathcal{M}_1 = \{\pm(ke_1 - le_2) \mid d \in \mathbb{Z}^2,\ k, l \in \mathbb{N} \text{ and } ka_1 + d, la_2 + d \in D\},$$

$$\mathcal{M}_0 = \{\pm(ke_1 - le_2) \mid d \in \mathbb{Z}^2,\ k, l \in \mathbb{N} \text{ and } kb_1 + d, lb_2 + d \in D\}.$$

Note that it is possible that $\mathcal{M}_1 = \emptyset$ or $\mathcal{M}_0 = \emptyset$.

Proposition 7. *Assume that T is as in (1) with $t = 1$, $n, m > 0$ and $D \subset \mathbb{Z}^2$. Then*
(i) if $ka_1, ka_2 \notin \Delta D$ for all $k \in \mathbb{N}$, then F is disconnected,
(ii) otherwise, then $\mathcal{N} = \{\pm ke_i \mid k \in \mathbb{N},\ i \in \{1, 2\} \text{ and } ka_i \in \Delta D\} \cup \mathcal{M}_1$.

Proposition 8. *Assume that T is as in (1) with $t = 0$, $n, m > 0$ and $D \subset \mathbb{Z}^2$. Let $b_2 = a_2$, $b_3 = a_3$. Then*
(i) if $kb_1, kb_2, kb_3 \notin \Delta D$ for all $k \in \mathbb{N}$, then F is disconnected,
(ii) otherwise, then $\mathcal{N} = \{\pm ke_i \mid k \in \mathbb{N},\ i \in \{1, 2, 3\} \text{ and } kb_i \in \Delta D\} \cup \mathcal{M}_0$.

References

1.S. Akiyama and J. M. Thuswaldner, *Topological properties of two-dimensional number systems*, J. Theor. Nombres Bordeaux, **12** (2000), 69-79.
2.C. Bandt, Self-similar sets 5. Integer matrices and fractal tilings of $\mathbb{R}^n$, Proc. Amer. Math. Soc. 112 (1991) 549-562.
3.T. K. Dey, H. Edelsbrunner, and S. Guha, *Computational topology* in Advances In Discrete and Computational Geometry, B. Chazelle, J. E. Goodman and R. Pollack, eds., Contemp. Math., Vol 223, American Mathematical Society, Providence, RI, 1999, pp. 109-143.
4.K.J. Falconer, Fractal geometry: Mathematical Foundations and Applications, John Wiley & Sons, Chichester, 1990.
5.K. J. Falconer, The dimension of self-affine fractals II, Math. Proc. Cambridge Philos. Soc. 111 (1992) 169-179.
6.M. Hata, *On the structure of self-similar sets*, Japan J. Appl. Math., **2** (1985), no. 2, pp. 381-414.
7.X.-G. He, K.-S. Lau, and H. Rao, Self-affine sets and graph-directed systems, Constr. Approx., 19 No.3, (2003) 373-397.
8.G.T. Herman, and E. Zhao, *Jordan surfaces in simply connected digital spaces*, J. Math. Imaging Visison, **6** (2003), 121-138.
9.I. Kirat, Boundary Points of Self-Affine Sets in R, Turk. J. Math., 27 (2003), no 2, 273-281.

10.I. Kirat, Disk-like tiles and self-affine curves with non-collinear digits, Math. Comp., 79 no.6 (2010) 1019-1045.
11.I. Kirat and I. Kocyigit, Remarks on self-affine fractals with polytope convex hulls, Fractals **18** no.4 (2010) 483-498.
12.I. Kirat and K.S. Lau, On the connectedness of self-affine tiles, J. London Math. Soc. 2, 62 (2000), 291-304.
13.I. Kocyigit, "Disconnectedness of self-affine sets and a method for finding the convex hulls of self-affine sets", M. Sc. Thesis, Istanbul Technical University, (2007).
14.J. Luo, *Boundary local connectivity of tiles in* $\mathbb{R}^2$., Topology Appl., **154** (2007), no. 3, 614-618.
15.J. Luo, H. Rao and B. Tan, *Topological structure of self-similar sets*, Fractals, **10** (2002), 223-227.
16.J. Luo and S. Akiyama and J. M. Thuswaldner, *On the boundary connectedness of connected tiles*, Math. Proc. Cambridge Philos. Soc., **137** (2004), no. 2, 397-410.
17.C. McMullen, The Hausdorff dimension of general Sierpiński carpets, Nagoya Math. J. 96 (1984) 1-9.
18.S. M. Ngai and T. M. Tang. *A technique in the topology of connected self-similar tiles*, Fractals, **12** (2004), no.4, 389-403.
19.S. M. Ngai and T. M. Tang. *Topology of connected self-similar tiles in the plane with disconnected interiors.* , Topology Appl., **150** (2005), no.1-3, 139-155.
20.A. Rosenfeld, *Connectivity in digital pictures*, J. ACM, **17** (1970), 146-160.

Proceedings, 6th Chaotic Modeling and Simulation International Conference
11 - 14 June 2013 Istanbul, Turkey

Some features in measurements of chaos

Valeriy A. Kolombet

Institute of Theoretical and Experimental Biophysics of Russian Academy of Sciences; Pushchino, Moscow region, Russia.
E-mail: v.kolombet@rambler.ru

Abstract: In frame of the transition to quaternion physics, we explored the expressions of special relativity for energy and time. This leads to a prediction of an especial role of the cube root of dimensionless masses and times for simplest objects. Our own experimentation with chaotic scatter of the different rates and analysis of literature data show that the mysterious cube roots are well-known probability amplitudes. One can spread this result from the simplest objects on every ones. Squares of the real probability amplitudes are probabilities. They appear to be quite congenerous with the fine-structure constant. The last finding leads to a unified theory of four fundamental forces and to an observation of a dynamic chaos in basis of the universe.

Keywords: Chaotic modeling, Chaos in chemical reaction rates, Chaos in radioactive decay rates, Quaternions, Special relativity, Quaternion quantum mechanics, Fine-structure constant, Unified theory, Dynamic chaos.

1. Introduction

This investigation was carried out in the lab where many years ago A.M. Zhabotinsky performed his well-known theoretical and experimental investigations of the nature of a chemical reaction discovered by B.P Belousov [1]. That work was induced by S.E. Shnoll, who investigated a strange scatter of results in measurements of biochemical reactions [2, 3]. Now, 50 year later, S.E. Shnoll still prolongs his investigation of the scatter of radioactive decay rates [4, 5, 6]. Like A.M. Zhabotinsky, the author (V.K.) is a former student of Prof. S.E. Shnoll but the subject is not any oscillatory reaction this time. Together with Shnoll, we investigate the same unusual scatter of measurement results. Shnoll uses his method of comparison of almost random shapes for two uncertain histograms taken from long set of repetitive measurements of radioactivity. In particular, he found a presence of 1436 min period, which means that the sidereal period of the Earth rotation is seen in the radioactive reactions rates. The author uses quite another method and gathers quite other results. Hope, these investigations will collide sometimes to show somewhat similar to a new picture of the universe.

2. The Theoretical and Experimental Bases of Model and Simulations

J.C. Maxwell's equations were written in quaternions but O. Heaviside rewrote the equations into the vector form [7, 8]. At present, the shift to hypercomplex physics seems to starts again [9]. In particular, an equation of special relativity that determines the square of energy (E) as a sum of the square of rest mass (m) and the square of momentum $\overline{p}$

$$E^2 = m^2 + p_x^2 + p_y^2 + p_z^2$$

may be scrutinized as a norm of the quaternion of energy E_q

$$E^2 = (m - ip_x - jp_y - kp_z)(m + ip_x + jp_y + kp_z) \equiv E_q^* \cdot E_q$$

Speed of light is omitted (i.e. c=1) in both cases for simplicity; sign * means the hypercomplex conjugation.

Let us limit for a while the consideration only by objects described by a quaternion that is the simplest and additionally symmetrical with respect to all imaginary units. For this purpose, let us express the quaternion E_q as a next step of complication of idea of number. The history of the number conception development shows that to do this, one has to use the numbers of the previous level. For E_q, this is a symmetric product of three complex numbers with orthogonal imaginary units

$$E_q = (a + ib)(c + jd)(e + kf)$$

This procedure needs six parameters instead four ones usual for a quaternion, and two of them must be expelled by the most symmetric way for the simplest object chosen. The most symmetric are case

$$E_{q1} = (a + ib)(a + jd)(a + kf)$$

and case

$$E_{q2} = (a + ib)(c + jb)(e + kb)$$

The rewriting of the resulting quaternion of energy E_{q1} into the coordinate system of the object (i.e. $\overline{p} = 0$) shows that its mass has to be the cube of some value:

$$E_{q1} = (a + i0)(a + j0)(a + k0) = a^3$$

This is a case of a usual massive particle like, for example, electron, proton, etc. We checked this prediction on light subatomic particles by comparison the cube roots of their masses preliminary divided by the mass of electron. The obtained cube roots appear to be not random; they surprisingly tend to integers or half-integers.

Because $ijk = -1$ the quaternion E_{q2} is simplest (and real too) in pure vector limit:

$$E_{q2} = (0 + ib)(0 + jb)(0 + kb) = (-b)^3$$

This is a case of a massless carriers of a field like, for example, photon.

A similar consideration for a quaternion of the time interval leads, in particular, to a task to investigate the cube root of the time for the immovable object, i.e. of our well-known time. To do this, we performed multiple (many millions) measurements of rates - so of chemical and biochemical reactions so of radioactive decays. We defined a fixed interval of time and measured the variable chaotic effect accumulated for this time. This is equivalent to measuring a chaotic time for which an experimentally defined constant effect is gained; this is a kind of clock. As a result, these clocks lead to identification of a non-dimensional «quantum of fluctuation». The quantum coincides numerical with the cube of the square root of 1/137 [10]. Thus, its cube root looks like the fundamental constant – a probability amplitude in an electromagnetic process.

We then synthesized the results of the study of both quaternions. Transition from the electromagnetic probability amplitude to respective probability and then the inversion gave the constant 137,036... Squares of the defined above dimensionless cube roots of masses (150,085... for nucleon, etc.) appear to be structural copies of the electromagnetic constant. (To improve the proximity to the integer numbers, we averaged masses in isotopic multiplets of elementary particles). This effect of quantization was confirmed on masses of atomic nuclei and even on the weights of the proteins [11, 12]. In the latter case, dimensionless masses were determined by means of dividing by the empirical constant 28,000 amu corresponding to the mass of a light protein.

Thus, the physical meanings of the squares of the cube roots of the dimensionless masses are that their reverse values (1/150,085..., etc.) are some unknown probabilities, and these probabilities are related to the well-known fundamental probability 1/137,036... Although we have studied only a simplest symmetric case, this physical meaning unlikely will change after the transition to the general case.

The observed resemblance of probabilities found in the investigation of quaternion of energy and quaternion of time looks very important. The importance was confirmed later by the success of the construction of the simple low-energy version of the unified theory on the set of these probabilities enriched by the set of their definitions [13, 14].

This theory successfully predicts the new particles and fields, as well as a presence of a kind of fundamental chaos in the universe. The most important achievement is, of course, the appearance of a wide area for new research. For example, one may find that the experimentally observed fundamental masses and times, particles and fields represent some special characteristics of measurements in the "fundamental chaos".

3. Conclusions

We live on background of chaotic processes developed in the universe but they do not attract our attention because we like investigate first of all repetitive processes, for example, oscillatory ones. Noise is somewhat bad. Even modeling of chaos has to be repetitive. Thus, the real chaos tends to stay invisible. According my own results the chaos in our chemical and biochemical reactions and in radioactive decay was found only because it expresses itself in the “quantum of fluctuation” which is by enough simple way linked with the fine-structure constant. According Shnoll’s results, only the Earth’s rotation with respect to the sphere of immovable stars helps to reveal the effect in the chaos in measurements of radioactive substances. The Unified theory based on this progress promises to solve the whole puzzle.

References

1. A.N. Zaikin and A.M. Zhabotinsky. Concentration wave propagation in two-dimensional liquid-phase self-oscillating system, *Nature*, vol. 225, 535-537, 1970.
2. S.E. Shnoll. On spontaneous synchronous transitions of soluted actomyosin molecules from one state to another, *Voprosy meditsinskoy khimii*, vol.4, No.6, 443-454, 1957.
3. S.E. Shnoll and E.P. Chetverikova. Synchronous reversible alterations in enzymatic activity ("conformational fluctuations") in actomyosin and creatine kinase preparations. *Biochimica et Biophysica Acta*, vol. 403, 89-97, 1975.
4. S.E. Shnoll et al. Experiments with radioactive decay of Pu-239 evidence sharp anisotropy of space, *Progress in physics*, No.1, 81-84, 2005.
5. S.E. Shnoll. Changes in the Fine Structure of Stochastic Distributions as a Consequence of Space-Time Fluctuations, *Progress in physics*, No.2, 39-45, 2006.
6. S.E. Shnoll. The "Scattering of the results of measurements" of processes of diverse nature is determined by the Earth's motion in the inhomogeneous space-time continuum. The effect of "half-year palindromes", *Progress in physics*, No. 1, 3-7, 2009.
7. J.C. Maxwell. *A Treatise on Electricity and Magnetism*. Clarendon Press, Oxford. 1873.
8. O. Heaviside. On the Forces, Stresses, and Fluxes of Energy in the Electromagnetic Field, *Philosophical Transaction of the Royal Society A*, vol. 183, 423–480, 1892.
9. A.P. Yefremov. Solutions of Dynamic Equations in Quaternion Model of Relativity, *Advanced science letters*, vol. 3, No. 2, 236-240, 2010.
10. V.A. Kolombet. Regular measurement – a new method of biophysical experiment, *Biophysics*. vol. 51, No.3, 504- 509, 2006.
11. V.A. Kolombet. On way to represent masses of elementary particles and atomic nuclei by unified system of integer numbers. *Preprint*. Pushchino: ONTI NCBI SSSR, 1981.
12. V.A. Kolombet. About possible existence of system of special values of protein masses, *Biophisics*, vol. 31, No. 3, 426-429, 1986.
13. V.A. Kolombet. About anomalous values of "masses" μ_x of elementary particles, *Preprint*, Pushchino, ONTI NCBI AN SSSR, 1981.
14. V.A. Kolombet. A phenomenological construction of a recursive version of the unified theory. - *VINITI*, 13.07.1984, N5074-84. Dep.

Chaos in high-energy physics

Valeriy A. Kolombet

Institute of Theoretical and Experimental Biophysics of Russian Academy of Sciences; Pushchino, Moscow region, Russia.
E-mail: v.kolombet@rambler.ru

Abstract: Imagine a funny mirrors room. The "mirrors" represent electromagnetic, strong, weak and gravitational maps corresponding to the low energy interactions. The maps work under an extended set of dimensionless constants like the low-energy electromagnetic coupling constant α = 1/137.036... The maps of the three last listed interactions are especially similar to each other; they differ only by an index 3, 2 and 1. The "mirrors" are smooth but the electromagnetic one has a tiny "chip" (the constant α/π). Multiple reflections of the "chip" in the "mirrors" correspond to the spectrum of fundamental masses of the universe. Close vicinities of the photon and muon masses, of the near 130 Gev/c2 "higgs" mass and of the Planck mass correspond to the "chip's" first reflections in the four "mirrors" in directions of fixed points. Due to a cap-like shape of the electromagnetic map, a period-doubling bifurcations lead to the fixed points multiplication. Because the particles are observed to concentrate near the fixed points in the case of low energies (in particular, the low energy carriers are located here), the spectrum of particle masses is supposed to resemble the spectrum of fixed points appeared in course of the multiple bifurcations. Really, the similarity is found between the calculation result and experimental data. Thus, there is a dynamic chaos in the core of high-energy physics.
Keywords: Maps, Fundamental forces, Masses of subatomic particles, Z-prime boson, Higgs, Bifurcation, Low-energy fields, LHC, Planck mass, Fine-structure constant, Unified theory, Dynamic chaos, Chaotic simulation.

1. Introduction

A dimensionless world constant $\alpha = 1/137.036\ldots$ is known as the fine-structure constant; this characterizes intensity of electromagnetic interaction, and this is often considered as a combination made from elementary electrical charge $\boldsymbol{e_o}$, speed of light c and Planck constant h: $\alpha = e_0^2/\hbar c$, here $\hbar = h/2\pi$. Number α^{-1} is linked with an old question of fundamental physics: "*Why it is 137?*" (Because all other numbers look also not too bad ones) [1, 2].
An approach found is based on the inclusion of $\alpha^{\mathbf{-1}}$ into a set of its analogues. It has been proposed that, in particular, these analogues are values $\alpha_x^{-1} = (m_x/m_e)^{\mathbf{2/3}}$, where m_x is mass m of elementary particle x. For example**,** m_e is mass of electron. Value α_e^{-1} is 1, for muon α_μ^{-1} is 34.967…, for proton $\alpha_p^{-1} = 149.945\ldots$, etc. Nontrivial numerical properties of set $\{(m_x/m_e)^{2/3}\}$ have been revealed by independent investigators [3-6].
Formula $\alpha_x^{-1} = (m_x/m_e)^{2/3}$ looks like a definition of new values α_x^{-1} made on basis of measured physical values m_x and m_e. In order to attach a meaningful physical sense to this formula one should show a self-dependency of the elements of the set $\{\alpha_x^{-1}\}$. In other words, one should find an independent

method of the values α_x^{-1} measurement or calculation. In case of a success, the equation $\alpha_x^{-1} = (m_x/m_e)^{2/3}$ will be enthroned as a new physical law, because any physical law is determined as a stable link between different physical values.
This task has been solved in frame of so called *low-energetic unified theory in representation of interaction constants* that is one of potentials on true way to the future full-blown version of the unified theory [7]. Main part of this theoretical model has a shape of the links' system; these links correspond to fundamental interactions; (see Table 1).

Table 1. Fundamental interactions and respective links on set $\{\alpha_x^{-1}\}$

k	Interaction	Map, corresponding to low-energy form of the interaction	Mass (Gev), particle and spin respective to the fixed points		
0?	Electromagnetic	$\alpha_x^{-1}{}_{new} = \alpha_x^{-1}{}_{old} \times \{ln[(\pi/\alpha)/\alpha_x^{-1}{}_{old}]\}^{2/3}$	0, 1.02, 20.5	γ, φ, ?	1 1 ?
1	Gravitational	$\alpha_x^{-1}{}_{new} = (\alpha_{Pl}^{-1})^{1/(k\times k)}/(\alpha_x^{-1}{}_{old})^{1/(3\times k)}$	10^{15}	g	2
2	Weak		81	$W^{\pm}$, Z^{o}	1
3	Strong		0.137	$\pi^{\pm}$, π^{o}	0

Existence of these links, i.e. ability to calculate the values α_x^{-1} on a base of other α_x^{-1} gives to set $\{\alpha_x^{-1}\}$ its own self-dependency and rises the formula $\alpha_x^{-1} = (m_x/m_e)^{2/3}$ to the rank of a new fundamental physical law.
For illustration of the ways of the links revealing, it is opportune to consider firstly value α_g^{-1} that is a gravitational counterpart of the electromagnetic constant α^{-1}. In this case, the square of elementary electrical charge e_0^2 in the numerator of α definition (that coincides with the numerator of Coulomb law) is substituted traditionally for expression $G_N m_x^2$ that is a numerator of the Newton gravitational law in case of equal interacting masses. This substitution leads to a known definition $\alpha_g = G_N m_x^2/\hbar c$ or $\alpha_g = m_x^2/m_{Pl}^2$; where $m_{Pl} = (\hbar c/G_N)^{1/2}$ is a definition of the Planck mass.
The definition of α_g is usually used to illustrate an immense difference between the strengths of gravitational and electromagnetic forces: the ratio α/α_g for two electrons is slightly more than 10^{40}. This remarkably huge number is known as Dirac number. Other particles lead to different huge numbers; for example, the ratio is more than million times less in case of two protons.
This slightly camouflaged comparison of m_x with e_0 – i.e. variable value with constant one – looks almost senseless. Nevertheless, one could use definition of α_g for revelation of a fundamental link between elements of set $\{\alpha_x^{-1}\}$. With that end in view one should firstly include α_g^{-1} into the set $\{\alpha_x^{-1}\}$ that looks enough

natural. The next step is to substitute masses m_x and m_{Pl} in definition $\alpha_g = m_x^2/m_{Pl}^2$ for equivalent representations $m_e\alpha_x^{-3/2}$ and $m_e\alpha_{Pl}^{-3/2}$ taken from the basic formula $\alpha_x^{-1} = (m_x/m_e)^{2/3}$ and from its particular shape $\alpha_{Pl}^{-1} = (m_{Pl}/m_e)^{2/3}$. Left and right parts of the appeared final equation (see Tables 1 and 2) contain α_g^{-1} and α_x^{-1} and both values belong to the set $\{\alpha_x^{-1}\}$. Subsequent substitutions of α_e^{-1}, α_μ^{-1}, α_π^{-1}, etc into the appeared equation lead to respective values α_g^{-1}, which also belong to $\{\alpha_x^{-1}\}$. This is a map determined on set $\{\alpha_x^{-1}\}$.
In particular, any α_x^{-1} creates another α_x^{-1}, the appeared one creates the second, then the third, forth, etc. These elements are arranged along a sequence, which is invariant with respect to the map because the transformation leads only to renumbering, to shift element position at the sequence. This sequence is a sub-set of the set $\{\alpha_x^{-1}\}$. This sub-set is invariant with respect to the map: map does not change it. Important particular case of such sub-set contains only identical elements. This specific situation is marked as a fixed point. Map does not influence its own fixed points at all: even renumbering is not seen. It is not trivial fact that fixed point of the considered map is situated near 10^{15} Gev, which is in close vicinity of famous Grand Unification mass appeared it is in unified theories.

Table 2. A way to the gravitation map

1. Newtonian law for gravitational force	$F = G_N mM/r^2$
2. Definition of dimensionless form of G_N	$\alpha_g^{-1} = G_N m_x^2 /\hbar c$
3. Definition of Planck mass	$(\hbar c/G_N)^{1/2} \equiv m_{Pl}$
4. α_g^{-1} as a mass-depended function	$\alpha_g^{-1} = (m_{Pl}/m_x)^2$
5. α_x^{-1} definition	$m_x = m_e \times (\alpha_x^{-1})^{3/2}$
6. α_g^{-1} as function depended from α_x^{-1}	$\alpha_g^{-1} = (\alpha_{Pl}^{-1}/\alpha_x^{-1})^3$
7. Map for gravitational interaction	$\alpha_x^{-1}{}_{old} =(\alpha_{Pl}^{-1})^{3/1}/(\alpha_x^{-1}{}_{new})^{3\times 1}$

Thus, a link based on the α_g definition represents a "gravitational map" ("gravitational transformation" of set $\{\alpha_x^{-1}\}$ into set $\{\alpha_x^{-1}\}$). A brief description of the gravitational map finding is given at Table 2. (The map direction chosen produces a stable fixed point).
A map for the low-energy weak interaction has been derived by analogous way from an equation that expresses a primary form of the dimensionless constant of low-energy (four-fermions) weak interaction α_w (see Tables 1 and 3). Substitutions have been made here quite similar to the gravity case and

additionally an appeared combination of constants (that is enough famous because it surprisingly almost coincides numerically with the Planck mass) was substituted by the Planck mass. The last substitution deletes a combination with Fermi constant of weak interaction and inserts a combination with Newton constant instead. The final equation is also a map, and this map is quite similar to the gravitational one. A brief description of the way to the weak map is given at Table 3.

Table 3. A way to the weak map

1. Four-fermions definition of α_w^{-1}	$\alpha_w^{-1} = G_F^2\,(m_x c^2)^4/(\hbar c)^6$
2. Numerical link between G_F and G_N [8]	$\hbar^6/c^2G_F^2 \approx (\hbar c/G_N)^{1/2} m_e^3$
3. New ("gravitational") expression for α_w^{-1}	$\alpha_w^{-1} \approx (\hbar c/G_N)^{1/2}\, m_e^3/m_x^4$
4. α_w^{-1} as a mass-depended function	$\alpha_w^{-1} \approx m_{Pl}\, m_e^3 / m_x^4$
5. α_w^{-1} as a function depended from α_x^{-1}	$\alpha_w^{-1} \approx \alpha_{Pl}^{-3/2}/\alpha_x^{-6}$
6. Map for weak interaction:	$\alpha_x^{-1}{}_{old} = (\alpha_{Pl}^{-1})^{3/2}/(\alpha_x^{-1}{}_{new})^{3\times 2}$

To underline the similarity of the maps, an integer parameter k has been determined (see Table 1). Cases $k = 1$ and $k = 2$ correspond to the gravitational and weak maps respectively. This is a way of gravitational and weak interaction unification in low-energy sector of the unified theory.

There are still degrees of freedom in both maps because definitions of dimensionless gravitational and weak constants are estimations. The Planck mass is also an enough free combination of fundamental constants. Small shift of α_{Pl}^{-1} to final value 1.51×10^{16} deletes some degrees of freedom and adjusts fixed points of both maps to some new meaningful values given in Table 1. A fixed point of the weak map hits this way into a close vicinity of the masses of the weak interaction carriers.

A low-energy equation for the case $k = 3$ (see Table 1) has been obtained simply by extrapolation of the cases $k = 1$ and $k = 2$. The case $k = 3$ corresponds to the strong nuclear interaction because the fixed point coincides with the mean mass of pions in this case. The pions determine the radius of the strong nuclear force because of their smallest hadron masses; they are known as the lowest-energy carriers of this interaction in frame of the low-energy description.

The fixed points in the cases $k = 3$ and $k = 2$ correspond to the carriers of respective interactions, and conformity with the case $k = 1$ leads to an expectation that the mass scale for the gravity carriers is the Grand Unification mass. This prediction (similar to erroneous one) can be excused because the Grand Unification scale is evidently out of the region of low energies, and the low-energy approach has the limited strength here. More good prediction is given by the extrapolation of the carrier spin. The sequence $k = 3$, $k = 2$ and $k = 1$ corresponds to the true carrier spin sequence: $s = 0$ for pions, $s = 1$ for W, Z-bosons and expected $s = 2$ for the gravity carrier. Thus, the empiric parameter k has a good chance on substitution by the physically plain parameter $3 - s$, i.e. the difference between the three forces could be significantly caused by the difference of spin of their carriers.

Because any map does not influence its own fixed points, the carriers of respective low-energy fields are free from a self-influence and this way they can play their roles without restrictions.

The rest force is electromagnetic one. Easy way of the respective map search (that is extrapolation to case $k = 0$; cases $k > 3$ are forbidden by absence of negative spins) leads to the division by zero and one should search for the electromagnetic map only on base of the fine-structure constant definition.

Value $\alpha = 1/137.036\ldots$ is low-energy limit of veritable electromagnetic "constant" that increases with growth of energy scale. Transformation of definition $\alpha = e_o^2/(hc/2\pi)$ into the shape of a map is facilitated by a circumstance that fundamental constants e_0, h and $\boldsymbol{c}$ have more stable reputation than number 2π which corresponds here to angle of full turn. Examples of this correspondence violation are widely known, and, thus, a way to qualitative search for α variation might be tested by substitutions of value 2π. In order to construct any map from the α definition, the unknown expression for the variable full turn angle must contain another element of set $\{\alpha_x^{-1}\}$: finally $\alpha_x^{-1}{}_{new}$ and $\alpha_x^{-1}{}_{old}$ are needed for map. Because of great role of fine-structure constant the second element is anticipated to be famous too - like for example $\alpha_p = (m_e/m_p)^{2/3}$. Note, that in extremely cold world, only electrons and protons survive. Substitutions of π on the trial expression $exp\ (\alpha/\alpha_p)^{3/2}$ leads to a successful trial "cold" iteration between α^{-1} and α_p^{-1}, and after verification it leads to the accepted link between members of respective pairs of α_x^{-1}, i.e. to the electromagnetic map presented in the first line of Table 1.

Strict quantitative validity of the electromagnetic map obtained by inexact reasoning about α variation is shown at Figures 1a and 1b. Experimental values α_x^{-1} of elementary particles tend to array along invariant sequences (that additionally confluent).

The especial electromagnetic point π/α seems to initiate spectrum of masses existence in the universe. Multiple reflections of π/α by the maps correspond to the spectrum of fundamental masses. Close vicinities of photon and muon masses, of 130 Gev/c2 "higgs" mass and of Planck mass correspond to the π/α first reflections by the four maps in directions of fixed points.

Existence of majority particles shown by Figures 1a and 1b is probably caused by the derived reflections of the fixed point of strong map ($k = 3$) (situated in close vicinity of α_π^{-1}; see Figure 1 and respective line in Table 1). Electromagnetic map reflects this self-determined point several times. In its turn, strong map reflects fixed point of electromagnetic map ($\alpha_x^{-1} \approx 158.5$) and also its broad vicinity presented by Figures 1a and 1b into vicinity ($\alpha_x^{-1} \approx 30$ –

40) of muon ($\alpha_x^{-1} \approx 35$) supporting its existence. Next two strong iterations reflect muon into neutral pion ($\alpha_x^{-1} \approx 42$) and then neutral pion into charged pion ($\alpha_x^{-1} \approx 41$); strong fixed point is situated near $\alpha_x^{-1} \approx 41{,}5$. Remarkable precision of electromagnetic map is illustrated also by long set of iterations of *Υ(3S)*- and *Υ(2S)*-mesons (see Figures 1a, 1b). On the contrary, *Υ(1S)*-meson sequence is shifted; probable reason of the sequence existence and the *Υ(1S)*-meson shift is peculiarity of point $\pi/\alpha \approx 430.5$ (see Figure 1b and respective map in Table 1). Dashed lines correspond to images of that particles whose link with the particle net is not too evident (Figure 1a). Essential growth of iterations density in η-meson vicinity (Figure 1a) could be considered as a hint on existence of an additional fixed point that corresponds to case k = -3 appeared in extended version of the theory [7]. This version considers all cases $|k| \leq 3$; each interaction gets here a weaker companion that could be slightly masked because pairs that corresponded to the same $|k|$ could be enough compact with respect to distances between these pairs. In particular, the massless graviton appears in the case k = -1.

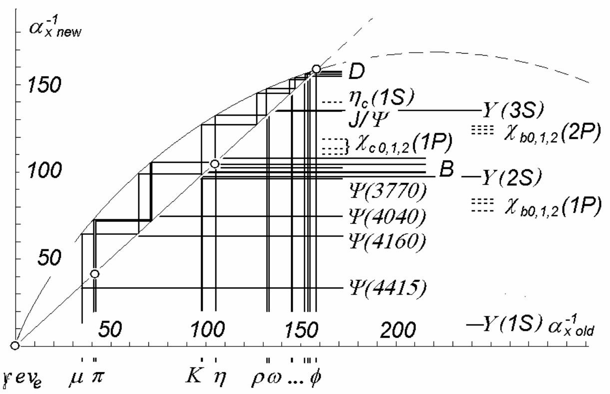

Fig.1a. This is a graphic representation of the meson net of electromagnetic iterations in vicinity of attractive fixed points of electromagnetic *($\alpha_x^{-1} \approx 158.5$)* and strong *($\alpha_x^{-1} \approx 41.5$)* maps. (Any iteration corresponds to a step of respective "ladder"). Four small circles show the positions of fixed points; particles tend to survive in vicinities of fixed points.

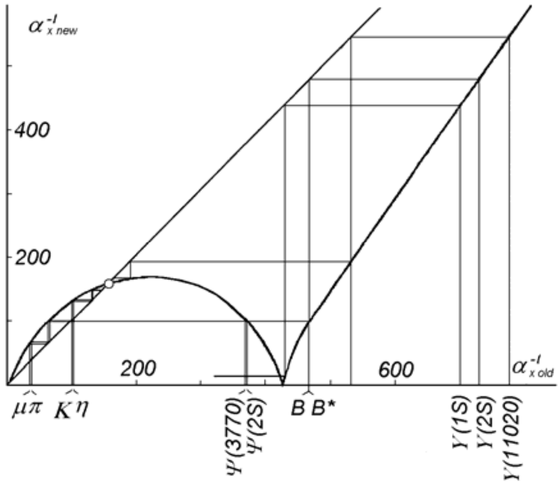

Fig. 1b. The same as at Figure 1a but in the scale representing also heavy particles.

It was mentioned above that the set of interactions numbered k = 3, 2 and 1 corresponds to the set of carrier spins $\boldsymbol{s}$ = 0, 1 and 2; here gravitational case (k = 1, s = 2) is posited out of range of low-energy scale and this violation excuses appearance of massless gravitational carrier. Fixed point of the case k = -2 produces the Z-prime boson – the approximately 10 Tev carrier of an announced "fifth force" and one of the LHC nearest goal.

Further extrapolation leads to electromagnetic case (probably k = 0, s = 3). Here a massless carrier exists (photon); the second roughness of the low-energy approach is appearance of three fixed points instead a single one. The three respective carriers of electromagnetism (only one of them is massless!) have probably spin 1 (see Table 1) instead a single carrier with spin 3 predicted by the extrapolation.

The coincidence of γ- and W,Z-spins reports on additional similarity of electromagnetic and weak forces (because of the high role of carrier spin for the interaction identification presented above). Thus, from the point of the low-energy particularly unified theory, it is this spin coincidence has ensured the success of Weinberg-Salam particularly unified theory that unifies electromagnetic and weak interactions.

Perfect version of the unified theory has to reveal a "genetic" link between mathematical shape of electromagnetic and gravitational maps and by this way, it has to finish synthesis of electromagnetic force with unified gravitation.

2. The Model and Simulation

Expansion into region of higher energies can be considered as natural intermediate stage of transition to final version of the unified theory. Characteristic bell-like shape of electromagnetic map (Figure 1b) leads to an assumption that a transition to more high-energetic description can be tested by means of a parameter λ:

$$\alpha_x^{-1}{}_{new} = \lambda\times\alpha_x^{-1}{}_{old} \times [ln(\pi\times\alpha^{-1}/\alpha_x^{-1}{}_{old})]^{2/3}$$

which increases the bell steepness and by this way leads to standard scenario of deterministic chaos development through cascade of bifurcations.

Did the nature lose this opportunity? To all appearances, not: the parameter λ characterizes scale of energy indeed, and former case $\lambda = 1$ corresponds it is to the low-energy limit.

Increase of λ is accompanied with usual shift of fixed point position. The loss of stability happens at $\lambda = 2.08$, and then a standard cascade of bifurcations and chaos appear [9]. Iterations start to diverge into infinity after $\lambda = 3.0728$ because of escaping through a gap that appears at this very moment and then widens enough fast. Comparison of calculation results with experimental spectra of particle α_x^{-1} is given at Figure 2. Intensive smooth of graphs (i.e. revealing the comparison in the lowest frequency range) is necessary for insurance of ability to compare too rare experimental data with gross result of the calculation.

This way, mass spectrum of elementary particles is enough similar to spectrum constructed from fixed points of all maps (see Figure 2 and last columns in Table 1), and also from reactions of each map on fixed points of other maps (Figures 1a, 1b).

In frame of this picture, a unique role of proton in the universe is caused by link of value α_p^{-1} with the first bifurcation of electromagnetic stable fixed point. View of this bifurcation is presented at Figure 3; image of key moment of stability loss (at intermediate energies, $\lambda = 2.08$; horizontal axis) is illustrated here by means of low-energy ($\lambda = 1$; vertical axis) form of electromagnetic map: the first bifurcation point is seen as proton when observer is positioned in our low-energetic world.

In the case of proton, one should probably underline mainly not stability loss in course of energy growth but conversely – back bifurcations and the fixed point stabilization in some final moment of the universe quenching after Big Bang. Protons are "snowflakes" of the frozen universe in this view.

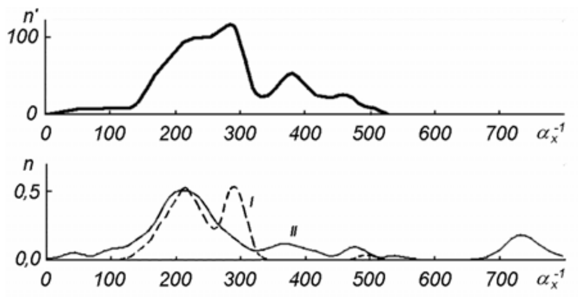

Fig. 2. Comparison of smooth distribution of fixed points of adjusted electromagnetic map with smooth experimental distributions of values α_x^{-1} of elementary particles. Top graph illustrates result of calculation and subsequent

smoothing of fixed point distribution; range of λ variation is 1 – 3,0728. Bottom graphs represent smoothed experimental α_x^{-1} values for barions (I) and mesons (II).

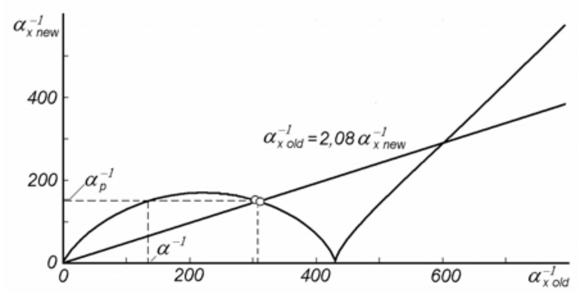

Fig. 3. The first bifurcation of stable fixed point of electromagnetic map takes place near λ = 2.08. This point is linked with α^{-1} and α_p^{-1}, i.e. with electric charge and mass of proton. In scale of m_x^{-1} (not of α_x^{-1}), the usual parameter 3 appears for the first bifurcation point instead of $\lambda = 2.08 = 3^{2/3}$ in full analogy with logistic map class.

Answer to the old question: "*Why it is 137?*" – could sound now as followed: "*Because it is this α_x^{-1} characterizes final border of matter stabilization in cold universe*".

The new results could be considered as additional supports of the approach proposed in direction of unified theory construction. It is shown that a set of experimental particle types accumulated to present moment appears to be enough big for revelation of features of well-known process of deterministic chaos development.

Analogous generators of noise are found in various natural and artificial systems. Complex regimes appear in the systems it is in cases of high energies. As a result, a new unity appears: data of high-energy physics more deep conjoin with data of many other branches of science. Simultaneously a well-developed mathematical apparatus is recruited into core of elementary particle physics. Moreover, the apparatus brings also respective scientific philosophies (see examples in [9, 10]).

Discussing physical sense of *the low-energy unified theory in representation of interaction constants* one might mention a perspective of probable junction of this theoretical model with present unified theories exploiting representation on multi-dimensionality of physical space. Really, a comparison of mathematical structure of weak and strong maps with gravitational map working in 3+1-dimensional space-time leads to suggestion about probable conformity of cases k = 2 and k = 3 with 6+1 and 9+1 spatial-temporal dimensions respectively. In this plane, absence of interactions with k = 4, 5, …, corresponding to 12+1, 15+1, … dimensions correlates with known limitation of dimension number near 10+1 dimensions found in high energy string theory. In frame of this picture the most appropriate case for electromagnetic map is $k = 0$. It intrigues by complete disappearance of spatial dimensions that could excuse sharp change of map shape (in case $k = 0$, map of gravitational types leads to division by zero). Gravitational (i.e. $k = 1$) distortion of 3+1-dimensional space-time in general relativity and homology of different maps in Table 1 lead to assumption that electromagnetism as case $k = 0$ is also kind of distortion. It could be distortion only of single temporal coordinate. In the pure temporal case the distortion could be caused only by an object, which has no spatial dimensions; in the low energy approach this an electromagnetic active dotty particle looks like electron.

Mean electromagnetic force between atoms in solid and liquid substances is enough intensive for experimentation to search for the probable fundamental link between time and electromagnetism. Universal system of dimensionless macroscopic states described by meaningful in this context value $\alpha^{3/2}$ has been found in broad spectrum of such experiments [11]. Thus, the discussed approach promises to accelerate process of the unified theory creation not only in traditional theoretical plane but also in experimental one.

In other publications, we are going to present broader theoretic and experimental synthetic picture where all described above is only a fragment; the roots of the whole picture appear to be embedded into both quaternion quantum mechanics and special relativity.

3. Conclusions

The low energy unified theory is constructed on base of fundamental constant numerical values known from experimentation. For this program realization, an advanced set of the dimensionless interaction constants has been found and then a system of maps corresponding to the system of fundamental physical forces was determined on this set. In particular, the map corresponding to electromagnetic force is described by a function whose important part has a bell-like shape. Opportunity of the bell proportions variation is analyzed because this promises bifurcation cascade and deterministic chaos in core of high-energy physics. Really, the first bifurcation appears to be in close connection with both proton and fine-structure constant existence and distribution of fixed points corresponds to spectrum of masses of subatomic particles.

References

1. M. Born. Reciprocity and the number 137, *Proc. of the Royal Society of Edinburgh*, vol. 59, 219-223, 1939.
2. A.S. Eddington. *Fundamental Theory*, Cambridge: Cambridge Univ. Press, 1946.
3. S. Petrescu and V. Petrescu. O formula universala pentru cuantificarea spectrului de masa al particulelor elementare si al resonantelor, *Revista de chimie*, vol. 31, 935-946, 1980.

4. V.A. Kolombet. On way to represent masses of elementary particles and atomic nuclei by unified system of integer numbers. *Preprint*. Pushchino: ONTI NCBI SSSR, 1981.

5. V.A. Kolombet. About anomalous masses μ_x of elementary particles. *Preprint*. Pushchino: ONTI NCBI SSSR, 1981.

6. V.A. Kolombet. Elementary particles, macroscopic fluctuations and discrete space-time, *Biofizika*, vol. 37, 492-499, 1992.

7. Kolombet, V.A. About isomorphism of fundamental and mental fields. *Gravitation & Cosmology*, vol. 8, Supplement, 223-224, 2002.

8. P. C. W. Davies. *The accidental universe*, Cambridge University Press, 1982.

9. H. Schuster. *Deterministic Chaos*. *An Introduction*, Veinheim: Physik-Verlag, 1984.

10. I. Prigogine. *From Being to Becoming: Time and Complexity in the Physical Sciences*, San Francisco: W.H.Freeman and company, 1980.

11. V.A. Kolombet. Regular measurement – a new method of biophysical experiment, *Biophysics*. vol. 51, No.3, 504- 509, 2006.

Proceedings, 6th Chaotic Modeling and Simulation International Conference
11 - 14 June 2013 Istanbul, Turkey

Mixing and Coherent Structures in Two and Three Dimensional Containers

Tatyana S. Krasnopolskaya[1], Volodymyr S. Malyuga[1] and Oleksandr L. Golichenko[2]

[1] Institute of Hydromechanics NASU, 03680 Kiev, Ukraine
(E-mail: t.krasnopolskaya@tue.nl; vsmalyuga@ukr.net)
[2] Kiev National Taras Shevchenko University, Kiev, Ukraine
(E-mail: GolichenkoOL@mail.ru)

Abstract. This study addresses problems: what determines coherent structures in mixing patterns and what are main elements of the coherent structures. We restrict our consideration to finite times and are mainly interested in how to organize steady or periodic flow and where to put the blob (or blobs) in order to achieve the best result in that finite time. Knowing types and positions of periodic points coherent structures in distributive mixing patterns could be classified. These structures are connected with hyperbolic and elliptic periodic points and lines for three-dimensional mixing flows.
Keywords: Distributive mixing, Periodic points and lines, Coherent structures.

1 Introduction

We consider the laminar mixing process in a two-dimensional annular wedge-shaped cavity and in a three-dimensional creeping flow of a viscous incompressible fluid contained in a finite circular cylinder, induced by a prescribed periodic motion of the end walls. Here we apply a method to locate periodic structures and manifolds. In contrast to two-dimensional flow of an incompressible fluid, for which the equations of motion of an individual passive particle can always be written in Hamiltonian form and for which well-developed methods of Hamiltonian mechanics can be applied, the study of three-dimensional mixing flows encounters considerable difficulties. An important characteristic of both two-dimensional and three-dimensional flows, that is closely related to the problem of determination of the regions of regular behaviour being barriers for the mixing process (Aref[1]), is the location of periodic points (or fixed points in the hyperplane of the Poincaré map). The determination and classification of periodic points in three-dimensional flows is a complicated problem. Furthermore, in three-dimensional flows these points can form one-dimensional periodic lines. A complete classification of the periodic points can be performed in accordance with three eigenvalues of the linearized matrix of the Poincaré map, and specific behaviour of the map near such a point can be associated with its type [4]. Generally, the periodic points of three-dimensional flows could be characterized by a much richer variety, compared to the points of two-dimensional flows, in which only three possible types exist. However, if in a three-dimensional flow the point lies on a periodic line it is not significantly different from periodic points in two-dimensional flows. In the three-dimensional case, the flow near a periodic line is topologically similar to the flow near a periodic point in two-dimensional case.

2 Stirring of a viscous incompressible fluid

2.1 Mixing in a two-dimensional annular wedge-shaped cavity

As a first example of mixing, we consider a two-dimensional creeping flow of an incompressible viscous fluid in an annular wedge cavity, $a \leq r \leq b$, $|\theta| \leq \theta_0$, driven by periodically time-dependent tangential velocities $V_{bot}(t)$ and $V_{top}(t)$ at the curved bottom and top boundaries, when a radius r is $r = a$ and $r = b$, respectively. The side walls, $a \leq r \leq b$, $|\theta| = \theta_0$ are fixed. We consider a discontinuous mixing protocol with the bottom and top walls alternatingly rotating over an angle Θ in clockwise and counterclockwise directions, respectively. More specifically, we consider the case

$$V_{bot}(t) = \frac{2a\Theta}{T}, V_{top}(t) = 0, \quad \text{for} \quad kT < t \leq \left(k + \frac{1}{2}\right) T,$$

$$V_{bot}(t) = 0, \quad V_{top}(t) = -\frac{2b\Theta}{T},$$

$$\text{for} \quad \left(k + \frac{1}{2}\right) T < t \leq (k+1)T, \tag{1}$$

where $k = 0, 1, 2, ...$ Θ is the angle of wall rotation and T is the period of the walls motion. The radial and azimuthal velocity components u_r and u_θ can be expressed by means of the stream function $\Psi(r, \theta, t)$ as

$$u_r = \frac{1}{r}\frac{\partial \Psi}{\partial \theta}, \qquad u_\theta = -\frac{\partial \Psi}{\partial r}. \tag{2}$$

For a quasi-stationary creeping flow in the Stokes approximation the stream function Ψ satisfies the biharmonic equation

$$\nabla^2\nabla^2\Psi = 0, \tag{3}$$

with the Laplace operator ∇^2 and the boundary conditions

$$\Psi = 0, \ \frac{\partial \Psi}{\partial r} = -V_{bot}, \ \text{at} \ r = a, \ |\theta| \leq \theta_0, \tag{4}$$

$$\Psi = 0, \ \frac{\partial \Psi}{\partial r} = -V_{top}, \ \text{at} \ r = b, \ \ |\theta| \leq \theta_0, \tag{5}$$

$$\Psi = 0, \ \frac{\partial \Psi}{\partial \theta} = 0, \ \text{at} \ a \leq r \leq b, \ |\theta| = \theta_0. \tag{6}$$

Therefore, we have the classical biharmonic problem for the stream function Ψ with prescribed values of this function and its outward normal derivative at the boundary.

The system of ordinary differential equations

$$\frac{dr}{dt} = \frac{1}{r}\,\frac{\partial\Psi}{\partial\theta}, \qquad r\frac{d\theta}{dt} = -\frac{\partial\Psi}{\partial r} \tag{7}$$

with the initial conditions $r = r_{in},\ \theta = \theta_{in}$ at $t = 0$ describes the motion of an individual (Lagrangian) particle occupying the position (r, θ) at time t. In fact, we have steady motion of the particle within time intervals $(kT, kT + T/2)$, $(kT + T/2, kT + T)$, with velocities that instantaneously change at $t_k = kT/2,\ (k = 0, 1, 2, ...)$.

It is easy to check that, within these intervals, when the stream function does not explicitly depend on time, system (11) has the first integral $\Psi(r, \theta) = const$. Therefore, this system is integrable and a particle initially at (r_{in}, θ_{in}) moves along a steady streamline during the first half period $(0, T/2)$. At the instant $t = T/2$ when the forcing is switched, the topology of streamlines is changed, and the particle instantaneously moves along a new streamline during the second half of period $(T/2, T)$, and so on. The spatial position of the particle is continuous, but its velocity experiences a discontinuity at each half period.

It is because of these abrupt periodical changes in the velocity field that the question of stability and instability of the solution of system (11) and possibility of chaotic advection (Aref[1]) naturally arises.

The problem of mixing of a certain amount of dyed passive material (the blob), as considered here, consists of tracking in time the positions of particles initially occupying the contour of the blob, say, the circle of radius R with the center at (r_c, θ_c). We assume that the flow provides only a continuous transformation of the initially simply connected blob. Therefore, the deformed contour of the blob gives the whole picture of the mixing.

This wedge-cavity flow problem has been solved analytically by Krasnopolskaya *et al.*[2]. Their analytical solution was used for the numerical evolution of the interface line between the marker fluid and the ambient fluid, which was carried out by the dynamical contour tracking algorithm.

2.2 Statement of mixing problem in a cylinder

Consider the three-dimensional Stokes flow in a finite cylinder that occupies the domain $0 \le r \le a,\ 0 \le \theta \le 2\pi,\ 0 \le z \le H$ in the cylindrical coordinates (r, θ, z). In terms of the velocity vector $\mathbf{u}$ and the pressure p, the Stokes flow of an incompressible viscous fluid (inertia terms being negligible) is governed by

$$\mu\nabla^2\mathbf{u} = \nabla p, \qquad \nabla\cdot\mathbf{u} = 0, \tag{8}$$

where ∇, $\nabla\cdot$, and ∇^2 stand for standard differential operations of gradient, divergence, and the Laplacian operator, respectively, and μ is the coefficient of shear viscosity of the fluid. The flow is generated by periodic motion of the cylinder end wall at $z = H$, while the cylinder wall $r = a$ remains fixed. In terms of Cartesian components, with the positive x-axis coinciding with the direction $\theta = 0$, the velocity vector $\mathbf{u} = u\,\mathbf{e}_x + v\,\mathbf{e}_y + w\,\mathbf{e}_z$ takes the following form at the domain boundaries:

$$\mathbf{u} = u_{top}(t)\,\mathbf{e}_x + v_{top}(t)\,\mathbf{e}_y, \quad z = H, \quad 0 \le r \le a, \quad 0 \le \theta \le 2\pi\,, \tag{9}$$

In what follows we consider one typical protocol of the wall motions with a constant velocity V and with period T (only the non-zero velocities are presented below). Protocol consists of two 'zigzag' steps of the top wall only:

$$u_{top} = V, \quad 0 \le t \le \frac{1}{2}T, \qquad\qquad v_{top} = V, \quad \frac{1}{2}T \le t \le T. \tag{10}$$

Note that the protocol is discontinuous, although the motion of the fluid inside the cylinder is steady at any time within the whole period. Since the inertia forces are neglected in the governing equations (8), these steady motions are established instantaneously. Because of the linearity of system (8) and the absence of time dependent terms, the velocity field in the cylinder is periodic with period T.

Important for further analysis is the dimensionless kinematic parameter $D = VT/a$, which represents the ratio of two typical time scales of any given protocol: the forcing period T and the advection time a/V (for a wall travelling over a typical distance a with a velocity V).

The mixing process taking place is due to advection of passive material tracers by the velocity field $\mathbf{u}$ and is hence governed by the three-dimensional system of ordinary differential equations

$$\frac{dx}{dt} = u\,(x,y,z,t), \quad \frac{dy}{dt} = v\,(x,y,z,t), \quad \frac{dz}{dt} = w\,(x,y,z,t), \tag{11}$$

with initial conditions $x = x_0$, $y = y_0$, $z = z_0$ at $t = 0$.

A full analytical solution for the linear vector boundary problem for the velocity field has been constructed by Meleshko *et al.*[5]. by the method of superposition. The principal idea of the method consists in representing the velocity field in the finite cylinder as the sum of two velocity fields: one for an infinite layer with thickness equal to the finite cylinder height, and another for an infinite cylinder with a radius equal to that of the original cylinder. Velocities in these simple domains are represented in the form of ordinary Fourier series with sets of arbitrary coefficients on the complete systems of Bessel and trigonometric functions, respectively. These series both identically satisfy the governing equation inside the domain and have sufficient functional arbitrariness for fulfilling any boundary conditions on the top and bottom walls and on the lateral surface of the cylinder, respectively. Because of the interdependency, the expression for a coefficient of a term in one series will depend on all the coefficients of the other series and vice versa. The final solution involves solving an infinite system of linear algebraic equations, providing the relations between applied velocities and the coefficients in two ordinary Fourier series on the complete systems of Bessel and trigonometric functions in radial and axial directions, respectively. The general theory of such infinite systems provides leading terms in the asymptotic behaviour of coefficients. An established technique was used to considerably improve the convergence of the series on the whole boundary, including the rims. The numerical results presented in Meleshko *et al.*[5] reveal that the boundary conditions for the case of a lid-driven cavity are satisfied within the accuracy $\mathcal{O}(10^{-3})$ in comparison with the prescribed velocity, even at the corner point.

The problem of accurate determination of the interface is obviously very complicated, as it moves and deforms with the flow. There exist many techniques to deal with flows containing sharp fronts, which can be divided into two basic strategies – front-capturing and front-tracking. Detailed reviews of the front-tracking methods are provided by Krasnopolskaya *et al.*[3] and Malyuga *et al.*[4].

2.3 Periodic points and lines

A periodic point $\mathbf{P}$ of period n can be classified as an elliptic, hyperbolic, or parabolic point depending upon the structure of the surrounding flow field. This classification is based on the behaviour (in the course of time) of an infinitesimally close neighbouring point $\mathbf{P} + d\mathbf{x}_0$. After n periods, the latter arrives at $\mathbf{P}+d\mathbf{x}_n = \mathbf{\Phi}_T^n(\mathbf{P}+d\mathbf{x}_0)$, upon linearization about the periodic point $\mathbf{P} = \mathbf{\Phi}_T^n(\mathbf{P})$, adding up to

$$d\mathbf{x}_n = F \cdot d\mathbf{x}_0 \tag{12}$$

with $F = \partial\mathbf{\Phi}_T^n/\partial\mathbf{x}|_{\mathbf{P}}$ the real Jacobian matrix. According to (12), stable and unstable structures may emerge, depending on the properties of the matrix F. In order to analyse the nature of the map near $\mathbf{P}$, the relation (12) is rewritten in the canonical (or Jordan) form

$$\boldsymbol{\eta}_n = S \cdot \boldsymbol{\eta}_0 \qquad S = R^{-1} \cdot F \cdot R \qquad \boldsymbol{\eta} = R^{-1} \cdot d\mathbf{x} \tag{13}$$

with R the transformation matrix relating the local Cartesian (dx, dy, dz) to the canonical ($\eta^{(1)}$, $\eta^{(2)}$, $\eta^{(3)}$) frame of reference.

In two-dimensional systems, elliptic points are surrounded by islands, sealing off the elliptic region from the remainder of the flow domain and in consequence acting as transport barriers. The hyperbolic points $\mathbf{x}_h$ are accompanied by stable manifolds $W^s(\mathbf{x}_h)$ and unstable manifolds $W^u(\mathbf{x}_h)$ that merge either into closed orbits or display transversal intersection. The former phenomenon is reminiscent of the aforementioned elliptic islands by obstructing communication between flow regions, whereas the latter brings about excessive stretching and folding of material elements, indicative of chaotic advection [1]. In the three-dimensional domain of interest the islands and manifolds, associated with periodic points on the elliptic and hyperbolic segments of the periodic line, readily merge into tubular objects and intricate surfaces, although possessing essentially two-dimensional characteristics. The periodic lines of period-2 of the flow generated in a cylinder are shown in figure 1

Such lines were found to exist only for $D > 2$. It is worth noting that each of the two lines returns into itself after two periods. Although any periodic point of second order exists always in combination with another one, they can belong to the same periodic line of the second order.

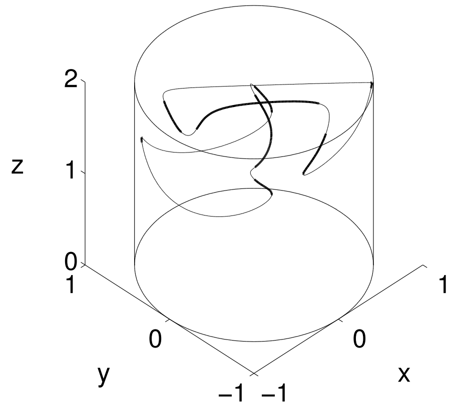

Fig. 1. The periodic lines of period-2 in the flow in the cylinder for $D = 5$. Thick and thin lines represent the elliptic and hyperbolic segments, respectively [4].

3 Coherent structures

The results presented correspond to one typical wedge cavity with $\theta_0 = \pi/4$ and $b/a = 2$. Using the dimensionless parameter $H = \Theta/\theta_0$ and a fixed value for the period T, the discontinuous mixing protocol (1) is completely defined. We restrict our consideration to the case $H = 4$. The accurate Lagrangian description of the contour line provides the possibility to construct an Eulerian representation of the mixture. Figure 2(a) shows the mixed state with the positions of the initially circular blob (green area) after six periods (red) and after twelve periods (blue). There are two main components of the coherent structure in the mixed state: one component formed by the thin filaments with their striation decreasing in time and the other one by the small 'rubbery' region, representing the unmixed part of the blob. What creates this structure? First of all, the invariant unstable manifold corresponding to the hyperbolic point of period-1 which is located in the centre of the original green blob (indicated by a black square in the middle in figure 2b). This manifold, presented in the figure 3(a), serves as a skeleton which forms the first main coherent structures of the deforming blob. The origin of the 'rubbery' coherent structure can be explained in terms of the existence of elliptic periodic points of period-6, period-2 and period-6, respectively, which are shown as white boxes in figure 2(b). In the upper part of the green circular blob (figure 2b), a small black box indicates the position of the hyperbolic fixed point of period-6 and therefore, the 'rubbery' region nearby this point will be destroyed completely in course of time.

The resulting deformation after twelve periods of small circular domains surrounding these higher order periodic points are shown in figure 3(b). The small circular blob surrounding the hyperbolic point transforms after twelve periods into a thin red line, while the three circular bolbs surrounding the elliptic points only slightly deform (the so-called 'rubbery' regions).

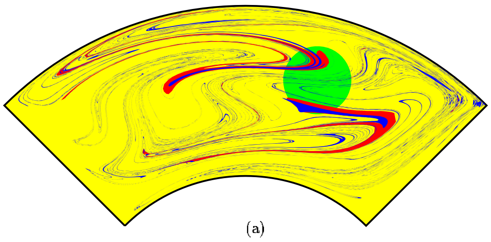

(a)

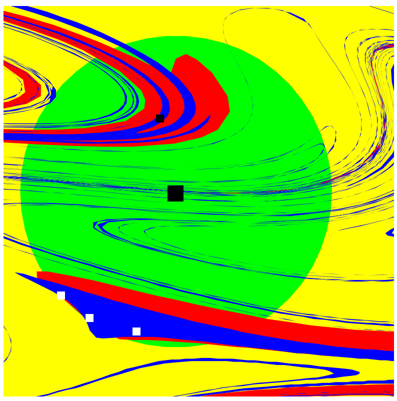

(b)

Fig. 2. Mixing patterns: (a) in the whole cavity; (b) in the region of the initial blob position.

4 Conclusions

Coherent structures in distributive mixing patterns are classified. These structures are connected with hyperbolic and elliptic periodic points (and lines) of order-1 or higher.

References

1.H. Aref. Stirring by chaotic advection. *J. Fluid Mech.* 143: 1–24, 1984.
2.T. S. Krasnopolskaya, V. V. Meleshko, G. W. M. Peters and H. E. H. Meijer. Steady Stokes flow in an annular cavity. *Q. J. Mech. Appl. Math.*, 49: 593–619, 1996.

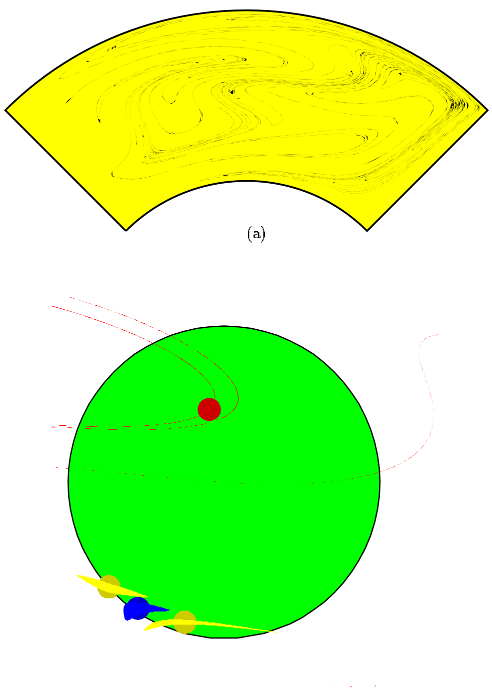

(a)

(b)

Fig. 3. The elements of coherent structures: (a) part of unstable manifold of the hyperbolic point of period-1 in the centre of the initial blob; (b) deformation patterns of small circular blobs surrounding periodic points of higher order.

3.T. S. Krasnopolskaya, V. V. Meleshko, G. W. M. Peters and H. E. H. Meijer. Mixing in Stokes flow in an annular wedge cavity. *Eur.J. Mech.B/Fluids*, 18:793–822, 1999.

4.V. S. Malyuga, V. V. Meleshko, M. F. M. Speetjens, H. J. H. Clercx and G. J. F. van Heijst. Mixing in the Stokes flow in a cylindrical container. *Proc. R. Soc. London*, A 458: 1867-1885, 2002.

5.V. V. Meleshko, V. S. Malyuga and A. M. Gomilko. Steady Stokes flow in a finite cylinder. *Proc. R. Soc. London*, A 456: 1741–1758, 2000.

Chaos In a Modified Cardiorespiratory Model

Tatyana S. Krasnopolskaya [1]
Evgeniy D. Pechuk [2]

[1] Institute of Hydromechanics NASU, Kyiv, Ukraine
E-mail: t.krasnopolskaya@tue.nl
[2] Institute of Hydromechanics NASU, Kyiv, Ukraine
E-mail: uzuzun@i.ua

Abstract: A new modified cardiorespiratory model based on the famous DeBoer beat-to-beat model and Zaslavsky map (which describes dynamics of the respiratory system as a generator of central type) was studied in details. In this case the respiratory tract was firstly modeled by the self-oscillating system under the impulsive influence of heartbeat. The steady-state regimes of the modified model are investigated by methods of the dynamical system theory. The regular (periodic and quasi-periodic) and chaotic regimes typical for functioning of the cardiosystem are found and studied.
Keywords: A beat-to-beat model, Cardiorespiratory system, DeBoer model, Zaslavsky map, Nonlinear dynamics, Chaotic regimes.

1. Introduction

The human cardiovascular system closly interacts with different organs and systems of organism. Realized self-oscillations in a cardiovascular system are under an activity of practically entire organism (see [2-5, 9-11]). Physiological rhythms are not isolated processes. There are numerous interactions of rhythms between itself and with an internal and external environment. Cardiac and respiratory rhythms form up during embryo development, and even the brief break of these rhythms after a birth results in death.

Existence of breathing and heart rhythm synchronization effect, found experimentally in the cardiovascular system both for healthy people and with pathologies, is well-proven in work Toledo [10] in 2002. It is well known, the dynamic process of mutual synchronization can be realized only in a case of presence of a subsystem mechanical interaction. Therefore, the indicated effect display testifies the presence of both direct and feedback interactions between the cardiovascular and respiratory systems.

A heart system and organism of man in general have one of major descriptions of activity, such as a blood pressure dynamics. His time-history, along with electrocardiogram (ECG), is an important information generator for research and diagnostics of laws and pathologies of the cardiovascular system. The task of mathematical model construction, describing the dynamics of arterial blood pressure, is far from completion. Complications of such design are related to the necessity of taking into account of influence on the cardiac rhythms not only the cardiovascular system but also other organs and systems of organism, in particular a respiratory system.

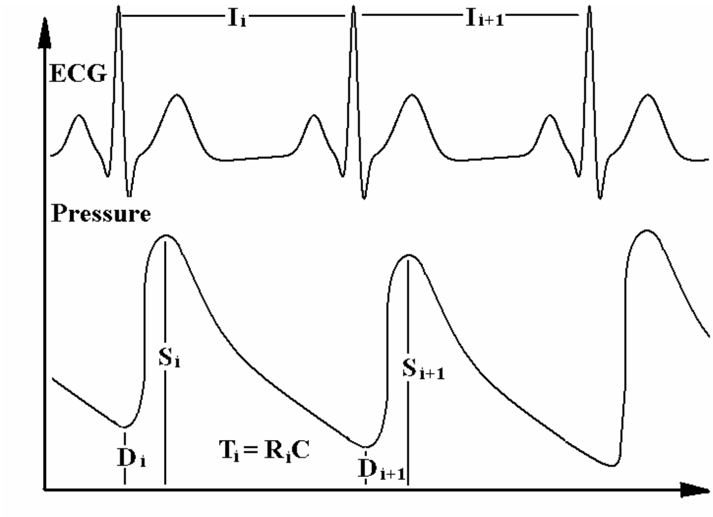

Fig. 1. Characteristics of the heartbeat in DeBoer model.

2. The mathematical model of a direct and reverse interactions

The DeBoer model of a cardiovascular system is under direct action of a respiratory systems (what corresponds to experimental data) [3]. This model was substantially developed in future. The sinus node responsiveness (and other detailed factors) is taking into account in the work of Seidel and Herzel [9] (the so-called SH-model). In this model chaotic dynamics was found in dynamics of a cardiosystem.

The models of both DeBoer and SH only considered direct respiratory influence on heartbeats. The SH-model got further development [5], where an effect of heartbeat and the resultant changes in the baroreceptor afferent activitiy to the SH-model are added and the cardiorespiratory sinchronization found due to this modification. Interaction of blood pressure and amplitudes of breathing oscillations revealed in accordance with principles of optimum control in the DeBoer model is investigated in the Grinchenko-Rudnitsky model [2]. This model allowed, in particular, to explain appearance of a peak on the Meyer frequency in the spectrums of pressure oscillations and synchronization of cardiac and respirator rhythms.

However, this model does not consider the reverse mechanical influence effect of the heartbeat changes on a breathing phase (frequency). In the present study, we add to the DeBoer model a self-oscillating system (which describes dynamics of the respiratory system as a generator of central type [4]) which is under impulsive influence of heartbeat.

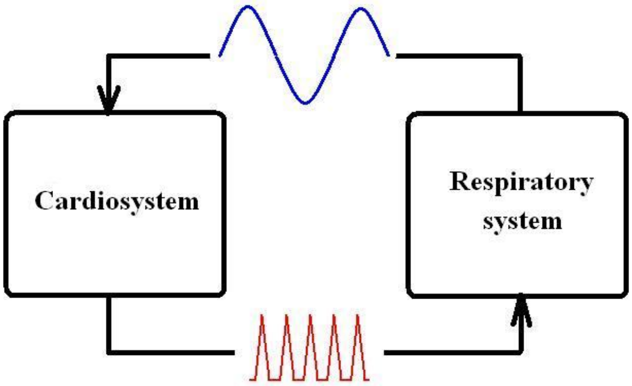

Fig. 2. Interaction of the cardiovascular and respiratory system

The DeBoer model describes the followings main characteristics of the heartbeat (see Figure 1) system: systolic pressure S , diastolic pressure D, R-R interval I and arterial time constant T (in a state of rest for a healthy man S=120 mmHg, D=80 mmHg, I=800 ms, T=1500 ms). This mathematical model is a system of five discrete nonlinear maps. This model contains only a direct mechanical influence of the respirator system on the cardiosystem and can be written in the form:

$$D_i' = S_{i-1}' \exp\left(-\frac{2}{3}\frac{I_{i-1}'}{T_{i-1}'}\right),$$

$$S_i' = D_i' + \gamma \frac{T_0}{S_0} I_{i-1}' + \frac{A}{S_0}\sin\left(2\pi f T_0 t_i\right) + \frac{c_2}{S_0},$$

$$I_i' = G_v \frac{S_0}{T_0}\hat{S}_{i-\tau_v}' + G_\beta \frac{S_0}{T_0} F(\hat{S}', \tau_\beta) + \frac{c_3}{T_0},$$

$$T_i' = 1 + G_\alpha \frac{S_0}{T_0} - G_\alpha \frac{S_0}{T_0} F(\hat{S}', \tau_\alpha),$$

$$\hat{S}_i' = 1 + \frac{18}{S_0}\arctan\frac{S_0(S_i'-1)}{18},$$

where $i \ge 1$, $D' = D / S_0$, $S' = S / S_0$, $\hat{S}' = \hat{S} / S_0$, $I' = I / T_0$, $T' = T / T_0$, $F(\hat{S}, \tau) = 1/9(\hat{S}_{i-\tau-2} + 2\hat{S}_{i-\tau-1} + 3\hat{S}_{i-\tau} + 2\hat{S}_{i-\tau+1} + \hat{S}_{i-\tau+2})$, $t_i = \sum_{k=0}^{i-1} I_k'$ is a real time, A=3 mmHg is a breathing amplitude, f=0.25 Hz is a breathing frequency, $c_2 = S_0 - D_0 - \gamma I_0$, $c_3 = I_0 - S_0(G_v + G_\beta)$, $\gamma = 0.016$ mmHg, $G_\alpha = 18$

ms/mmHg, $G_\beta = 9$ ms/mmHg, $G_v = 9$ ms/mmHg, $\tau_\alpha = \tau_\beta = 4$, $\tau_v = 0$, is equal to 0 if frequency of heartbeat is less then 75 beat/min, and τ_v is equal to 1, if frequency is more then 75 beat/min.

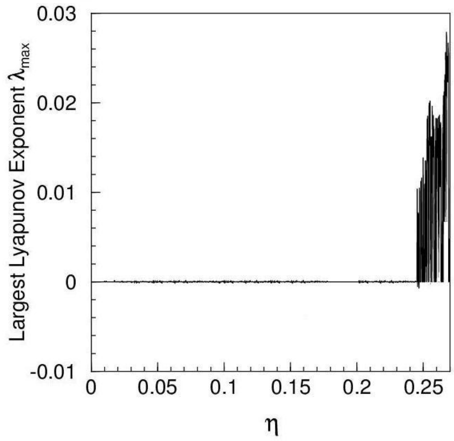

Fig. 3.Largest Lyapunov exponent of the modified system

We suppose that a healthy man at rest breathes periodically with a permanent frequency and an amplitude of motions of thorax. In that case a breathing process can be described as the self-oscillating system [4], which has a steady limit cicle. Thus for the mathematical modeling of a such system equations of the Zaslavskiy map could be used. Famous Zaslavsky map is the system of equations [8, 12] which describes the dynamics of an amplitude r_n and a phase φ_n of the system (in which periodic self-oscillations with a frequency ω are realized) which is under T-periodic impulsive action of constant intensity η . Te system has the following form:

$$r_{n+1} = \left(r_n + \eta \sin \varphi_n\right) \exp\{-\kappa T\},$$
$$\varphi_{n+1} = \varphi_n + \omega T + \nu \left(r_n + \eta \sin \varphi_n\right) \frac{1 - \exp\{-\kappa T\}}{\kappa},$$

where κ, ν are constant parameters.

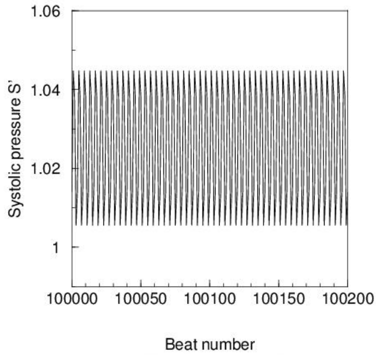

a) $\eta = 0.22$

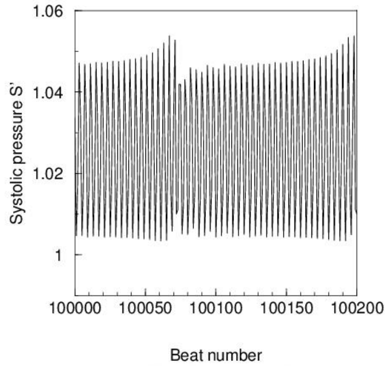

b) $\eta = 0.23$

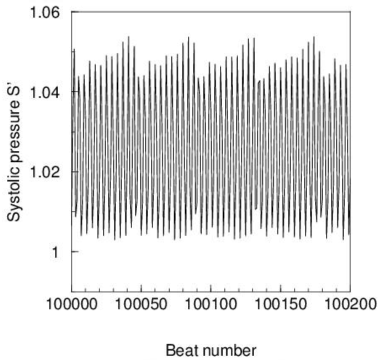

c) $\eta = 0.24$

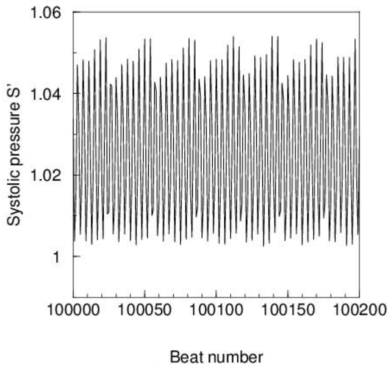

d) $\eta = 0.25$

Fig. 4. Simulated systolic pressure data (cases a, b, c and d)

In our approach these equations are used to describe changes of an amplitude and phase of a respiratory system effect for every R-R interval with an intensity proportional to systolic pressure: $\tilde{\eta} = -\eta(S_n - S_0)$:

$$r_{n+1} = \left(r_n - \eta(S_n - S_0)\sin\varphi_n\right)\exp\{-\kappa I_n\},$$
$$\varphi_{n+1} = \varphi_n + 2\pi f I_n + \nu\left(r_n - \eta(S_n - S_0)\sin\varphi_n\right)\frac{1-\exp\{-\kappa I_n\}}{\kappa},$$

where I is R-R interval, $\eta > 0,\ \kappa,\ \nu$ are constant parameters of interaction.

Thus, we study the dynamics of the modified model of cardiorespiratory system, which consists of the DeBoer model with direct respiratory influence $(A + r_i)\sin\varphi_i$, and with reverse influence modeled by the Zaslavskiy map system (see Figure 2).

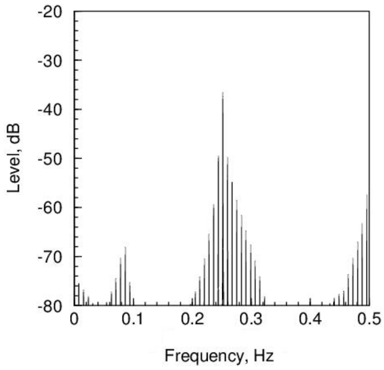

a) $\eta = 0.23$

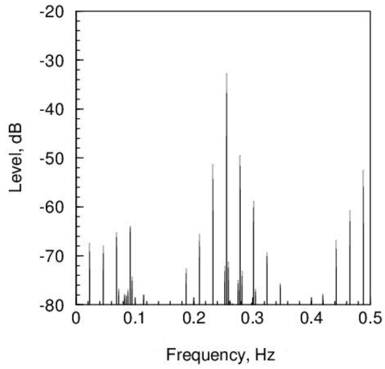

b) $\eta = 0.24$

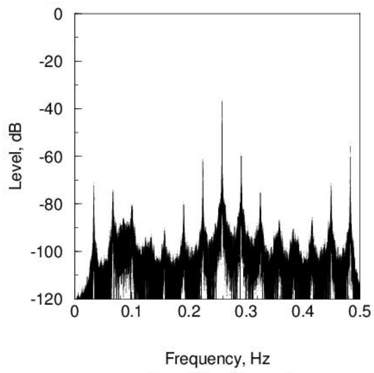

c) $\eta = 0.25$

Fig. 5. Power spectra computed from systolic pressure data (cases a, b and c)

3. Numerical simulations results

In accordance with physiology of healthy man, the followings values of variables and constants are used in our numerical simulations: $I'[0] = 0.53$, $S'[-j] = 1.08$, $j = 0,...,6$, $r'[0] = 0$, $\varphi'[0] = 0$, $\kappa = 0.001$ 1/ms, $\nu = 0.001$ 1/msmmHg. In order to study steady-state regimes first of all the largest Lyapunov exponent [1, 6, 7] was found. The dependence of the largest Lyapunov exponent of the modified system on values of the bifurcation parameter η is shown in Figure 3. The dynamics of the system changes with increasing of this parameter. There is the region where Lyapunov exponent positive ($\eta > 0.245$) that means transition to chaos occurs. We emphasize that η describes intensity of heart influence on a respiratory system. The next Figure 4 illustrates a behaviour of systolic pressure data in the modified model. Power spectra computed from these data are shown in Figure 5. The spectrum in Figure 5.a and in Figure 5.b have discrete peaks which are situated equidistantly with a frequency difference. So that, graphs indicate that there are regular regimes in the modified system.

Finally, for the steady-state regimes, when the largest Lyapunov exponent is positive and the chaotic regime is realized, the power spectrum is continuous (Figure 5.c).
Phase portrait projections on the plane of the simulated systolic pressure and R-R interval data are presented in Figure 6. The phase portrait in the Figure 6.a represents a singular solid curve and corresponds to quasiperiodic regime. There are only several points in the phase portrait in Figure 6.b which means that at $\eta = 0.24$ the modified system has regular periodic regime. And in Figure 6.c when $\eta = 0.25$ the phase portrait has numerous lines (the number of which increases in time) and corresponds to chaotic steady-state regime. So we have found such steady-state basic regimes as:

1. at $\eta = 0.22$, periodic regime (Figure 4.a);
2. at $\eta = 0.23$, quasiperiodic regime (Figure 4.b, Figure 5.a, Figure 6.a);
3. at $\eta = 0.24$, periodic regime (Figure 4.c, Figure 5.b, Figure 6.b);
4. at $\eta = 0.25$, chaotic regime (Figure 4.d, Figure 5.c, Figure 6.c).

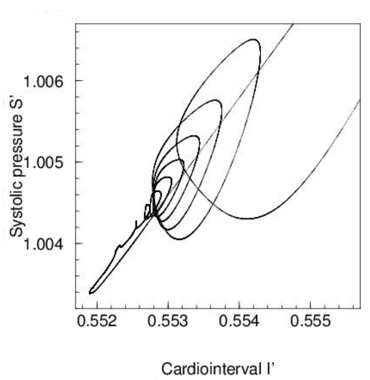

a) $\eta = 0.23$

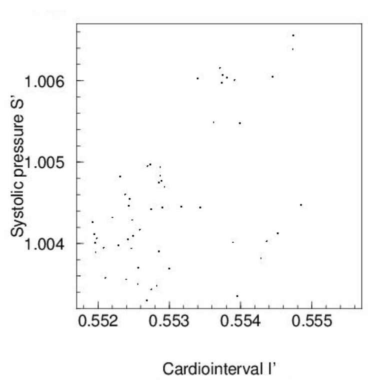

b) $\eta = 0.24$

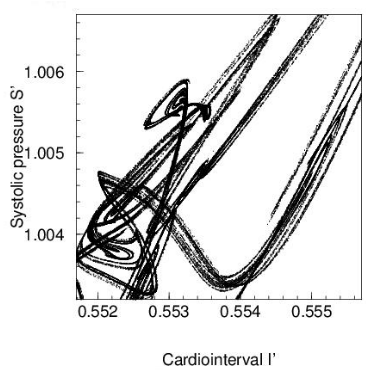

c) $\eta = 0.25$

Fig. 6. The parts of phase portraits simulated systolic pressure and R-R interval data (cases a, b and c)

4. Conclusions

On the basis of the DeBoer model an interaction of the heartbeat and the respiratory system as dissipative Zaslavskiy map is studied and the modified model of cardiosystem is built out. This model takes into account both direct and reverse influence of subsystems – cardiovascular and respiratory.

The methods of modern theory of the dynamical systems are used to study laws of the steady-state regimes of the modified model. Firstly the chaotic regimes were found out. Analysis of bifurcational curves of the largest Lyapunov exponent, projections of phase portraits, temporal realizations and power spectrums allowed to investigate the basic laws of dynamics of the model. The dynamics of heartbeat and respiratory systems are in good correspondence with experimental information of healthy man. Found irregularities of phase trajectories of the modified model depend on intensity of heart rhythm influence on breathing, what is well known characteristic for the dynamics of the cardiovascular system of healthy man.

References

1. V. S. Anishshenko. *Acquaintance with nonlinear dynamic,* Institute of Computer Science, Moscow-Izhevsk, 2002.
2. V. T. Grinchenko and A. G. Rudnitskiy. A model of interection of the cardiovascular and respiratory systems, *Acoustic Journal*, vol. 9, no. 3, 16-26, 2006.
3. R. W. DeBoer, J. M. Karemaker, J. Strakee. Hemodynamic fluctuations and baroreflex sensitivity in humans: A beat-to-beat model, *Amer. J. Physiol*., vol. 253, H680-H689, 1987.
4. L. Glass, M. C. Mackey. *From Clocks to Chaos. The rhythms of life,* Princeton University Press, Princeton, 1988.
5. K. Kotani [et al.]. Model for cardiorespiratory synchronization in humans, *Physical Review E.*, vol. 65, 051923-051932, 2002.
6. S. P. Kouznetsov. *Dynamic chaos*, Physmatlit, Moscow, 2001.
7. T. S. Krasnopolskaya, A. Yu. Shvets. *Regular and chaotic dynamics of the systems with limited excitation,* Institute of Computer Science, Moscow-Izhevsk, 2008.
8. R. Z. Sagdeev, D. A. Usikov and G. M. Zaslavsky. *Nonlinear Physics: From the Pendulum to Turbulence and Chaos*, Harwood Academic Publishers, New-York, 1988.
9. H. Seidel and H. Herzel. Bifurcations in a nonlinear model of the baroreceptor-cardiac reflex, *Acoustic Journal*, vol. 115D, 145-160, 1998.
10. E. Toledo [et al.]. Does synchronisation reflect a true interaction in the cardiorespiratory system, *Med. Engng Phys.*, vol. 24, 45-52, 2002.
11. T. Yang, M. D. Jacobstein, M. N. Levy. Synchronization of automatic cells in S-A node during vagal stimulation in dogs, *Am. J. Physiol.*, n. 246, H585-H591, 1984.
12. G. M. Zaslavsky. The simplest case of a strange attractor, *Phys. Lett. A*, vol. 69, 145-147, 1978.

Proceedings, 6th Chaotic Modeling and Simulation International Conference
11 - 14 June 2013 Istanbul, Turkey

The Presence of Chaos in the GDP Growth Rate Time Series

Radko Kříž, Radka Kněžáčková

University of Pardubice, Czech Republic
E-mail: Radko.Kriz@upce.cz, Radka.Knezackova@upce.cz

Abstract: The goal of this paper is to find chaos in the Gross domestic product (GDP) growth rate of selected European countries. We chose only those European countries where data is available since 1980, because we needed the longest time series possible. These are the following states: Belgium, Finland, France, Norway, Spain, Switzerland and United Kingdom. At first we will estimate the time delay and the embedding dimension, which is needed for the largest Lyapunov exponent estimation. The largest Lyapunov exponent is one of the important indicators of chaos and is generally well-known. Subsequently we will calculate the 0-1 test for chaos. Finally we will compute the Hurst exponent by using the Rescaled Range analysis. The Hurst exponent is a numerical estimate of the predictability of a time series. The results indicated that chaotic behaviors obviously exist in GDP growth rate.
Keywords: Chaos theory, GDP, GDP growth rate, Time series analysis, Phase Space Reconstruction, Hurst exponent, largest Lyapunov exponent.

1. Introduction

Humanity has always been concerned with the question of whether the processes in the real world are deterministic in nature. Determinism can be understood variously. In this paper we assume a mathematical sense of determinism, which is given by equations and initial conditions. Mathematical models that are not deterministic because they involve randomness are called stochastic. Are the processes in the real world deterministic or stochastic in nature? Real processes in nature, according to the expectation of Mandelbrot [15], lie somewhere between pure deterministic process and white noise. This is why we can describe reality either by a stochastic or deterministic model. The Hurst coefficient can give us an answer to this.
An interesting case of determinism is deterministic chaos. The only purely stochastic process is a mathematical model described by mathematical statistics. The statistical model often works and is one of many possible descriptions if we do not know the system. This also applies to economic quantities, including forecasts for GDP. The basic question is therefore the existence of chaotic behavior. If the system behaves chaotically, we are forced to accept only limited predictions. In this paper we will try to show the chaotic behavior of GDP growth rate.

2. Methods of analyzing

In short, we will describe the basic definitions and the basic methods for examining the input data.

2.1 Phase space reconstruction

According to Henry [9], the main goal in nonlinear time series analysis is to determine whether or not a given time series is of a deterministic nature. If it is, then further questions of interest are: What is the dimension of the phase space supporting the data set? Is the data set chaotic?

The key to answering these questions is embodied in the method of phase space reconstruction, which has been rigorously proven by the embedding theorems of Takens [19]. Takens theorem was independently suggested for example Packard [17]. Takens' theorem transforms the prediction problem from time extrapolation to phase space interpolation.

Let there be given a time series $x_1, x_2, \ldots, x_N$ which is embedded into the m-dimensional phase space by the time delay vectors. A point in the phase space is given as:

$$Y_n = x_n, x_{n-\tau}, \ldots, x_{n-(m-1)\tau} \quad n = 1,2,\ldots,N-(m-1)\tau \tag{1}$$

where τ is the time delay and m is the embedding dimension. Different choices of τ and m yield different reconstructed trajectories. How can we determine optimal τ and m?

2.2 Optimal time delay

A one-to-one embedding can be obtained for any value of the time delay $\tau > 0$. However, very small time delays will result in near-linear reconstructions with high correlations between consecutive phase space points and very large delays might obscure the deterministic structure linking points along a single degree of freedom. If the time delay is commensurate with a characteristic time in the underlying dynamics, then this too may result in a distorted reconstruction.

In order to estimate τ, two criteria are important according to Kodba [12]. First, τ has to be large enough so that the information we get from measuring the value of x at time $n + \tau$ is significantly different from the information we already have by knowing the value of x at time n. Only then will it be possible to gather enough information about all other system variables that influence the value of x to reconstruct the whole attractor. Second, τ should not be larger than the typical time in which the system loses memory of its initial state. This is particularly important for chaotic systems, which are intrinsically unpredictable and hence lose memory of the initial state as time progresses.

Following this reasoning, Fraser and Swinney [3] introduced the mutual information between x_n and $x_{n+\tau}$ as a suitable quantity for determining τ. The mutual information between x_n and $x_{n+\tau}$ quantifies the amount of information we have about the state $x_{n+\tau}$ presuming we know the state x_n. Now we can define mutual information function:

$$I(\tau) = -\sum_{h=1}^{j}\sum_{k=1}^{j} P_{h,k}(\tau)\ln\frac{P_{h,k}(\tau)}{P_h P_k} \tag{2}$$

where P_h and P_k denote the probabilities that the variable assumes a value inside the h^{th} and k^{th} bins, respectively, and $P_{h,k}(\tau)$is the joint probability that x_n is in bin h and $x_{n+\tau}$ is in bin k. Hence, the first minimum of $I(\tau)$ marks the optimal choice for the time delay.

2.3 Optimal embedding dimension

The embedding dimension *m* is conventionally chosen using the "false nearest neighbors'" method. This method measures the percentage of close neighboring points in a given dimension that remain so in the next highest dimension. The minimum embedding dimension capable of containing the reconstructed attractor is that for which the percentage of false nearest neighbors drops to zero for a given tolerance level ε.

In order to calculate the fraction of false nearest neighbors the following algorithm is used according to Kennel [11]. Given a point *p(i)* in the *m*-dimensional embedding space, one first has to find a neighbour *p(j)*, so that

$$\|p(i)-p(j)\| \leq \varepsilon \tag{3}$$

We then calculate the normalized distance R_i between the *(m + 1)th* embedding coordinate of points *p(i)* and *p(j)* according to the equation:

$$R_i = \frac{|x_{i+m\tau} - x_{j+m\tau}|}{\|p(i)-p(j)\|} \tag{4}$$

If R_i is larger than a given threshold R_{tr} , then *p(i)* is marked as having a false nearest neighbor. Equation (4) has to be applied for the whole time series and for various *m = 1, 2, ...* until the fraction of points for which $R_i > R_{tr}$ is negligible [12].

2.4 The largest Lyapunov exponent

Lyapunov exponent λ of a dynamical system is a quantity that characterizes the rate of separation of infinitesimally close trajectories. Quantitatively, two trajectories in phase space with initial separation δZ_0 diverge.

$$\delta Z(t) \approx e^{\lambda t}|\delta Z_0| \tag{5}$$

The largest Lyapunov exponent (LLE) can be defined as follows:

$$\lambda = \lim_{\substack{\delta Z_0 \to 0 \\ t\to\infty}} \frac{1}{t} \ln \frac{|\delta Z(t)|}{|\delta Z_0|} \tag{6}$$

The limit *δZ0→0* ensures the validity of the linear approximation at any time. LLE determines a notion of predictability for a dynamical system. A positive LLE is usually taken as an indication that the system is chaotic (provided some other conditions are met, e.g., phase space compactness) [14].

We have used the Rosenstein algorithm, which counts the LLE as follows:

$$\lambda_1(i) = \frac{1}{i\Delta t} \cdot \frac{1}{(M-i)} \sum_{j=1}^{M-i} \ln \frac{d_j(i)}{d_j(0)} \tag{7}$$

Where $d_j(i)$ is distance from the *j* point to its nearest neighbor after *i* time steps and *M* is the number of reconstructed points. For more information see [6, 18].

2.5 The 0-1 test for chaos

New test for the presence of deterministic chaos was developed by Gottwald & Melbourne [7]. Their '0 - 1 test for chaos takes as input a time series of measurements, and returns a single scalar value usually in the range 0 - 1. In contrast the 0 - 1 test does not depend on phase space reconstruction but rather works directly with the time series given. The input is the time-series data and the output is 0 or 1, depending on whether the dynamics is non-chaotic or chaotic.

Briefly, the 0-1 test takes as input a scalar time series of observations $\varphi_1, \ldots, \varphi_N$. We have used the algorithm according to Dawes & Freeland [1]. First, we must fix a real parameter c and construct the Fourier transformed series:

$$z_n = \sum_{j=1}^{n} \phi_j e^{ijc}, \quad n = 1,\ldots,N \tag{8}$$

Then we have computed the smoothed mean square displacement:

$$M_c(n) = \frac{1}{N-p} \sum_{j=1}^{N-p} \left| z_{j+n} - z_j \right|^2 - \left(\sum_{k=1}^{N} \frac{\phi_k}{N} \right)^2 \frac{1-\cos nc}{1-\cos c} \tag{9}$$

Finally we have estimated correlation coefficient to evaluate the strength of the linear growth

$$r_c = \frac{\operatorname{cov}(n, M_c(n))}{\sqrt{\operatorname{cov}(n,n)\operatorname{cov}(M_c(n), M_c(n))}} \tag{10}$$

2.6 Long memory in time series

Hurst exponent *(H)* is widely used to characterize some processes. Hurst exponent is used to evaluate the presence or absence of long-range dependence and its degree in a time-series. For more information see [8, 10]. The Hurst exponent is a measure that has been widely used to evaluate the self-similarity and correlation properties of fractional Brownian noise, the time series produced by a fractional Gaussian process [16]. We can describe self-similarity process following equation:

$$X(at) = a^H X(t) \tag{11}$$

where a is a positive constant, and H is the self-similarity parameter, for $0 < H < 1$.

We have used a methodology known as Rescaled Range analysis or R/S analysis. To calculate the Hurst exponent, one must estimate the dependence of the rescaled range on the time span n of observation. The Hurst exponent is defined in terms of the asymptotic behavior of the rescaled range as a function of the time span of a time series as follows:

$$E\left[\frac{R(n)}{S(n)}\right] = Cn^H \text{ as } n \to \infty \tag{12}$$

Where $[R(n)/S(n)]$ is the rescaled range; $E[y]$ is expected value; n is number of data points in a time series, C is a constant. For more information see [13].

3. Analysis of GDP growth rate time series

3.1 Input data

The GDP in current prices in millions of national currency (including 'euro fixed' series for euro area countries) is used in this paper. We have used data (quarterly, seasonally adjusted and adjusted data by working days) from the Eurostat between the years 1980 - 2012. According to Eurostat [2], seasonal adjustment is a treatment of infra-annual time series to remove the spurious effect of seasonal patterns from the series' trend and cycle. These patterns can be caused by weather, public holidays such as Christmas, the timing of school vacations or of dividend payments and a number of other reasons.

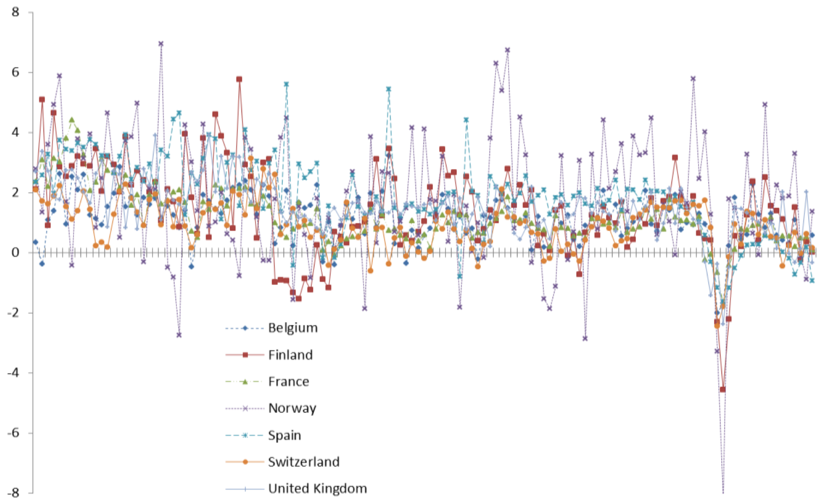

Fig. 1. GDP growth rate time series.

Generally, the main problem in analyzing the GDP time series is the lack of data. That is why we chose only those European countries where data is available since 1980. These are the following states: Belgium, Finland, France, Norway, Spain, Switzerland and United Kingdom. So, we have 132 values from these countries. The analysis of such short time series in the context of nonlinear dynamics or in the presence of chaos can be questionable. We know, according to Horák [4] or Galka [5], that for this kind of method results are provable for at least 10^3 data-points. Analysis of short time series (order of 10^1) may lead to a spurious estimation of the invariants e.g. LLE. Despite the above, we have no choice but to analyze GDP time series in the context of nonlinear dynamics and try to find chaotic behavior of GDP growth rate time series. Therefore, all results are only estimates. The second problem can be the presence of trends in time series. Trended data are not suitable for future analysis to study chaos dynamics. There is no universal way to remove the trend from the data set. The results often depend strongly on how the data are detrended. This is solved using the GDP growth rate (cf. Figure 1).

3.2 Calculation of the largest Lyapunov exponents

At first we will estimate the time delay and the embedding dimension, which is needed for the largest Lyapunov exponent estimation. We will use the mutual information approach to determine the time delay. The first minimum of the mutual information function I(τ) (2) marks the optimal choice for the time delay. The embedding dimension m is chosen using the "false nearest neighbors'" method. The minimum embedding dimension capable of containing the reconstructed attractor is that for which the percentage of false nearest neighbors drops to zero for a given tolerance level ε. Then, we calculated the LLE using the Rosenstein algorithm. All computed values are positive (cf. Figure 2). A positive LLE is usually taken as an indication that the system is chaotic.

	Tau	ED	LLE	H	test 0- 1
Belgium	2	3	0,032	0,76	0,99
Finland	3	3	0,840	0,88	0,99
France	3	3	0,084	0,96	0,82
Norway	1	3	0,011	0,54	0,99
Spain	2	3	0,078	0,99	0,95
Switzerland	3	3	0,585	0,82	0,99
United Kingdom	4	3	0,071	0,96	0,98
Average	2,571	3,000	0,243	0,844	0,959
SD	0,904	0,000	0,306	0,146	0,058

Fig. 2. The optimal time delay, The optimal embedding dimension, The Largest Lyapunov exponent, The Hurst exponent, Value of chaos test 0-1 for selected countries, average and standard deviation

3.3 Results of the 0-1 Test for Chaos

In this chapter we calculate the correlation coefficient as was shown above. The correlation coefficient is near to 0 for non-chaotic data and near 1 for chaotic data. All computed values are very close to 1 (cf. Figure 2). Hence, we can convincingly assume there to be chaotic behavior in the GDP growth rate time series.

3.4 Calculation of the Hurst exponent

The Rescaled Range analysis gave us values of the Hurst exponent between 0,54 (Norway) and 0,99 (Spain) (cf. Figure 2). Most values indicate the presence of long memory in GDP growth rate time series except the value of the Hurst exponent for the Norway GDP growth rate, which indicates random walk. Those values are in accordance with our expectations. We know that the value of H is between 0 and 1, whilst real time series are usually higher than 0,5. If the exponent value is close to 0 or 1, it means that the time-series has long-range dependence. We can assume that the true value lies somewhere between those values. We think that those values are sufficient for a credible prediction. Now we also know that the fractal dimension DF =2-H. We have estimated the values of the fractal dimension selected time series between 1,01 and 1,46.

4. Conclusions

Chaos theory has changed the thinking of scientists and the methodology of science. Making a theoretical prediction and then matching it to the experiment is not possible in chaotic processes. Long term forecasts are, in principle, also impossible according to chaos theory. The main problem is in the quantity and quality of data. Some improvement of measurement cannot help us adequately, because it is a fight against power of exponential rate. Nonlinear dynamics and chaos theory have also corrected the old reductionist tendency in science. Now it is known that real processes are nonlinear and a linear view can be wrong. The basic question is therefore - the existence of chaotic behavior. If the system behaves chaotically, we are forced to accept only limited predictions. But it is much better than random processes.

Although we analyzed various GDP growth rate time series, the results came out very similar. We have shown in this paper that the GDP growth rate time series are chaotic and contain long memory. First, we computed the values of the time delays and the embedding dimensions. The average value of computed time delays is 2,6. In all 7 cases we chose the value 3 as the optimal embedding dimension. Subsequently, we calculated the LLE and all computed values were positive. A positive LLE is usually taken as an indication that the system is chaotic. If the fractal dimension is low, the LLE is positive and the Kolmogorov entropy has a finite positive value, chaos is probably present. Then we conducted the 0-1 test for chaos according to which chaos was present. All computed values were very close to 1. Hence, we can convincingly assume there to be chaotic behavior in the GDP growth rate time series. From these estimations it can be concluded that the GDP growth rate time series is chaotic. Finally we have computed the Hurst exponent by Rescaled Range analysis. Most values indicate the presence of long memory in GDP growth rate time series, except the value for the Norway GDP growth rate.

We know that the main problem when analyzing GDP time series is the lack of data. As mentioned above, we chose only those European countries where data is available since 1980. Although these time series are not ideal in length, they are acceptable for analysis. The results came out mostly very similar. The presence of chaos in selected GDP growth time series is not only a coincidence.

In the future we would like to focus on the proper statistical significance for nonlinearity and on predicting the GDP. In particular, the surrogate data approach (e.g. Theiler et al. [20]) is a powerful tool for detecting actual nonlinear behavior, and distinguishing it from other phenomena.

References

[1] DAWES, J., H., P., FREELAND, M., C.: The ‘0–1 test for chaos’ and strange nonchaotic attractors, people.bath.ac.uk/jhpd20/publications, 2008.

[2] ESS Handbook for Quality Reports, Luxembourg: Office for Official Publications of the European Communities, 2009

[3] FRASER, A., M., SWINNEY, H., L.: Independent coordinates for strange attractors from mutual information Phys. Rev. A 33 1134–40, 1986.

[4] HORÁK, J., KRLÍN, L., RAIDL, A.,: Deterministický chaos a jeho fyzikální aplikace, Academia, Praha, 437, 2003.

[5] GALKA, A.,: Topics in Nonlinear Time Series Analysis, World Scientific, (2000)

[6] GOTTHANS, T.,: Advanced algorithms for the analysis of data sequences in Matlab, Master’s Thesis, University of technology Brno, 2010.

[7] GOTTWALD, G., A., MELBOURNE, I.,: A new test for chaos in deterministic systems. Proc. Roy. Soc. A 460 603–611, 2004.

[8] GRASSBERG, P, PROCACCIA, I, Characterization of strange attractors, Phys. Rev. Lett. 50, 346, 1983.

[9] HENRY, B., LOVELL, N., CAMACHO, F.,: Nonlinear dynamics time series analysis, in Akay,M. (ed.), Nonlinear Biomedical Signal Processing, Insititue of Electrical and Electronics Engineers, Inc., pp. 1 – 39, 2001.

[10] HURST, H., E.,: "Long term storage capacity of reservoirs". Trans. Am. Soc. Eng. 116: 770–799, 1951.

[11] KENNEL, M., B., BROWN, R., ABARBANEL, H., D., I.,: Determining embedding dimension for phase space reconstruction using a geometrical construction Phys. Rev. A 45 3403–11, 1992.

[12] KODBA, S., PERC, M., MARHL, M.,: Detecting chaos from a time series. European Journal of Physics 26, 205–215, 2005.

[13] KŘÍŽ, R,: Chaos in GDP, Acta Polytechnica Vol. 51 No. 5, 2011.

[14] LORENZ, H-W.,: Nonlinear Dynamical Economics and Chaotic Motion, Springer-Verlag, 1989.

[15] MANDELBROT, B., B.,: The Fractal Geometry of Nature, W.H. Freeman and Co., 1983.

[16] MANDELBROT, B., B., NESS VAN, J., W.,: Fractional Brownian motions, fractional noises and applications. SIAM Rev. 10, pp. 422, 1968.

[17] PACKARD, N., H., CRUTCHFIELD, J., P., FARMER, J., D., SHAW, R., S.,: Geometry from a time series. Phys Rev Lett 1980; 45:712–6.

[18] ROSENSTEIN, M., T., COLLINS J., J., LUCA, C., J.,: A practical method for calculating largest Lyapunov exponents from small data sets. Physica D 65:117-134, 1993.

[19] TAKENS, F.,: Detecting Strange Attractor in Turbulence (Lecture Notes in Mathematics vol 898) ed D A Rand and L S Young (Berlin: Springer) p 366, 1981.

[20] THEILER, J., EUBANK, J., LONGTIN, A., GALDRIKIAN, B., FARMER J., D.,: Testing for nonlinearity in time series: The method of surrogate data, Physica D 58, 77 (1992)

Proceedings, 6th Chaotic Modeling and Simulation International Conference
11 - 14 June 2013 Istanbul, Turkey

Stability and bifurcation in a two species predator-prey model with quintic interactions

I. Kusbeyzi Aybar[1] and I. Hacinliyan[2]

[1] Department of Computer Education and Instructional Technology, Yeditepe University, 26 August Campus, Kayisdagi Street, Istanbul, 34755, Turkey
(E-mail: ikusbeyzi@yeditepe.edu.tr)

[2] Department of Mathematics, Istanbul Technical University, Maslak, Istanbul, 34469, Turkey
(E-mail: hacinliy@itu.edu.tr)

Abstract. In this work, the generalization of Lotka-Volterra model including the addition of symmetrically coupled quintic polynomial interaction is analyzed. Stability and bifurcation properties of this model are studied. It is also shown that the model has a family of limit cycles bifurcating from the Hopf points by using a numerical method.

Keywords: Predator-Prey Models, Stability, Bifurcation Analysis.

1 Introduction

Predator-prey problem attempts to model the relationship between the populations of two or more species in interaction. The simplest model of predator-prey interactions, called the classical Lotka-Volterra (LV) model, is given by the following system of differential equations [1]:

$$\dot{x} = x(a - by), \qquad \dot{y} = -y(c - dx), \tag{1}$$

where the parameters a, b, c and d characterize the predator-prey environment, dots denote the time derivatives, $x(t)$ and $y(t)$ are the prey and predator populations, respectively. Due to its unrealistic stability characteristics, the LV model serves as a starting point of many generalized models which should predict a single closed orbit, or perhaps finitely many, but not a continuous family of neutrally stable cycles. Among many ways to improve stability in the LV model, a simple approach is to add polynomial interactions. One of the generalizations considered by Nutku has been to suggest a cubic self-interaction term, instead of a quadratic self-interaction [2]. The Nutku generalization introduces additional stability in a simple way; beside a further generalization involving coupling of the form $x^k y$, where k is a positive integer and $k \leq 2$, provides a rich spectrum of equilibrium points leading to Hopf, pitchfork, saddle node and cusp bifurcations [3]. Moreover, the limit cycles of the Hopf bifurcation point tend to a specific solution of an equation in [3]. Meanwhile, it is shown that the Gause type predator-prey model with holling type III functional response and allee effect on prey, which is another type generalization of the LV model, topologically equivalent to the differential equations, are given by a fifth order polynomial system in [4,5]. On the other hand, Giné and Romanovski have obtained necessary and sufficient integrability conditions at the origin for a complex generalization of the LV model where a quintic nonlinearity is introduced [6]. By the help of this motivation, we will examine stability and bifurcation properties of this model with the symmetrically coupled interaction by using approximate techniques near equilibrium points.

2 The Model, Stability and Bifurcation Scenarios

The quintic Lotka-Volterra model with symmetrically coupled interaction is given as,

$$\begin{aligned} \dot{x} &= x(1 - Ax^4 - Bx^3y - Cx^2y^2 - Dxy^3 - Ey^4) \\ \dot{y} &= -y(1 - Ay^4 - Bxy^3 - Cx^2y^2 - Dx^3y - Ex^4), \end{aligned} \tag{2}$$

where parameters A, B, C, D and E are positive. System (2) with $A(-B + 3D) = E(3B-D)$ has an integrating factor of the form $V = (xy)^{(-4B+2D)/(B-D)}$ which allows us to find the algebraic integral

$$(xy)^{\frac{r_1}{r_2}} \left(\frac{r_2}{r_1} + \frac{r_2}{2} xy(x^2 + y^2) + \frac{Cr_2}{r_3} x^2y^2 - \frac{Ar_2}{r_1}(x^4 + y^4) \right) = \text{constant}, \tag{3}$$

where $r_1 = -3B + D$, $r_2 = B - D$ and $r_3 = B + D$.

System (2) has 13 trivial equilibrium points, which are (0,0), $(A^{-1/4}, 0)$, $(-A^{-1/4}, 0)$, $(iA^{-1/4}, 0)$, $(-iA^{-1/4}, 0)$, $(0, A^{-1/4})$, $(0, -A^{-1/4})$, $(0, iA^{-1/4})$, $(0, -iA^{-1/4})$, $(T_1^{-1/4}, T_1^{-1/4})$, $(-T_1^{-1/4}, -T_1^{-1/4})$, $(iT_1^{-1/4}, iT_1^{-1/4})$ and $(-iT_1^{-1/4}, -iT_1^{-1/4})$ with $T_1 = A+B+C+D+E$; and nontrivial ones depending on the values of the coefficients, which are summarized below.

(i) If $T_2 = A - B + C - D + E > 0$ then $(T_2^{-1/4}, -T_2^{-1/4})$, $(-T_2^{-1/4}, T_2^{-1/4})$, $(iT_2^{-1/4}, -iT_2^{-1/4})$ and $(-iT_2^{-1/4}, iT_2^{-1/4})$ are also equilibrium points.
(ii) If $T_2 = A - B + C - D + E < 0$ then there are four complex equilibrium points: $(\sqrt{2}\,(1 + i)\,(-T_2)^{-1/4}/2, -\sqrt{2}\,(1 + i)\,(-T_2)^{-1/4}/2)$, $(\sqrt{2}\,(-1 + i)\,(-T_2)^{-1/4}/2, \sqrt{2}\,(1 - i)\,(-T_2)^{-1/4}/2)$ and their complex conjugates.
(iii) If $A = E$ and $B = D$ then there are infinitely many equilibrium points.
(iv) If $A \neq E$, $B = D$ and $T_3 = A - C + E > 0$ then $(T_3^{-1/4}, iT_3^{-1/4})$, $(-T_3^{-1/4}, -iT_3^{-1/4})$, $(iT_3^{-1/4}, -T_3^{-1/4})$, $(-iT_3^{-1/4}, T_3^{-1/4})$ and their complex conjugates are also equilibrium points.
(v) If $A \neq E$, $B = D$ and $T_3 = A - C + E < 0$ then there are eight complex equilibrium points: $(\sqrt{2}\,(1 + i)\,(-T_3)^{-1/4}/2, \sqrt{2}\,(-1 + i)\,(-T_3)^{-1/4}/2)$, $(\sqrt{2}\,(1+i)\,(-T_3)^{-1/4}/2, \sqrt{2}\,(1-i)\,(-T_3)^{-1/4}/2)$, $(\sqrt{2}\,(-1+i)\,(-T_3)^{-1/4}/2, \sqrt{2}\,(-1-i)\,(-T_3)^{-1/4}/2)$, $(\sqrt{2}\,(-1+i)\,(-T_3)^{-1/4}/2, \sqrt{2}\,(1+i)\,(-T_3)^{-1/4}/2)$ and their complex conjugates.
(vi) If $A \neq E$, $B \neq D$ and $|B - D| > 2\,|A - E|$ then there are 4 real and 4 complex, or 2 real and 6 complex equilibrium points. One can find these points by solving the system of the equations $x = (-\alpha \pm \sqrt{\alpha^2 - 1})y$, $2\alpha = (B - D)/(A - E)$, and $Ax^4 + Bx^3y + Cx^2y^2 + Dxy^3 + Ey^4 = 1$.

(vii) If $A \neq E$, $B \neq D$ and $|B - D| < 2\,|A - E|$ then one can find equilibrium points by solving the system of the equations $x = (-\alpha \pm i\sqrt{1-\alpha^2})y$ and $Ax^4 + Bx^3y + Cx^2y^2 + Dxy^3 + Ey^4 = 1$.

On the other hand, system (2) is Lyapunov unstable for the chosen values of the parameters, which can be very easily demonstrated using the Lyapunov function $V = (E - A)(x^2 + y^2) + 2Bxy$ which is positive definite if and only if $E > A$ and $E - A > B$. Therefore, we obtain

$$\dot{V} = 2(x^2 - y^2)\left[\beta A(x^4 + y^4) + ((A + E)^2 + B(D - B) + \beta C)x^2y^2 - \beta\right], \quad (4)$$

where $\beta = A - E < 0$. Although the second factor has negative definite dominant term, the first factor changes sign as $|x| = |y|$. Hence there is a regime where the system is Lyapunov unstable so that we can limit our discussion to local stability. At this stage, we focus on trivial equilibrium points to examine stability. Nontrivial ones will be taken into account for a spacial case.

Linearized eigenvalues about the first real trivial equilibrium point $(0, 0)$ are $\{\pm 1\}$; thus the origin is a saddle point. Eigenvalues for the points $(A^{-1/4}, 0)$ and $(-A^{-1/4}, 0)$ are $\{-4,\ -1 + E/A\}$, so these points are saddle when $A < E$, and stable nodes when $A > E$. Eigenvalues associated with points $(0, A^{-1/4})$ and $(0, -A^{-1/4})$ are $\{4,\ 1 - E/A\}$. If $A < E$, these equilibrium points are saddle, otherwise they are unstable nodes. On the other hand the eigenvalues for both of equilibrium points $(T_1^{-1/4}, T_1^{-1/4})$ and $(-T_1^{-1/4}, -T_1^{-1/4})$ are $\{\pm i\sqrt{8[2(E - A) + (D - B)]/T_1}\}$, a pair of purely imaginary eigenvalues, if $2(E - A) + (D - B) > 0$ and $\{\pm\sqrt{8[2(A - E) + (B - D)]/T_1}\}$ if $2(E - A) + (D - B) < 0$. Thus the first purely imaginary values satisfy the resonance conditions and the system can be expanded into a resonant normal form, which gives Hopf bifurcation under the condition $2(E - A) + (D - B) > 0$. For the other condition, these points are also saddle.

Let $A = 1$ and $B = C = D = E = 2$. In this special case, the real equilibrium points of the system are (0,0), (1,0), (-1,0), (0,1), (0,-1), $A_1(1/\sqrt{3}, 1/\sqrt{3})$, $A_2(-1/\sqrt{3}, -1/\sqrt{3})$, $A_3(1, -1)$, $A_4(-1, 1)$; and there are 16 complex equilibrium points. Trivial equilibrium point at the origin is a saddle point with the eigenvalues $\{\pm 1\}$. (1,0) and (-1,0) are also saddle points with the eigenvalues $\{-4,\ 1\}$. Similarly (0,1) and (0,-1) are saddle points with the eigenvalues $\{4,\ -1\}$. On the other hand, the points A_1 and A_2 with the eigenvalues $\{\pm i4/3\}$; and also the points A_3 and A_4 with the eigenvalues $\{\pm i4\}$ are also Hopf points. The third order normal form about the point A_1 is

$$\dot{u} = 4iu(1 - 14uv)/3, \qquad \dot{v} = -4iv(1 - 14uv)/3, \quad (5)$$

where u and v refer to the variables in the near identity transformation. This normal form indicates Hopf bifurcation. From the linearized eigenvalues of system (5), it is clear that the normal form will be $\dot{u} = i\alpha u f(uv)$, $\dot{v} = -i\alpha v f(uv)$ which admits the solution uv =constant. Hence the inclusion of higher order terms in the normal form will only change the purely imaginary eigenvalues, since the only change will be the constant value of $f(uv)$ to the normal form approximation. This implies that the character of the local bifurcation will not change by including further terms. Normal form analysis for the other equilibrium points is omitted for brevity.

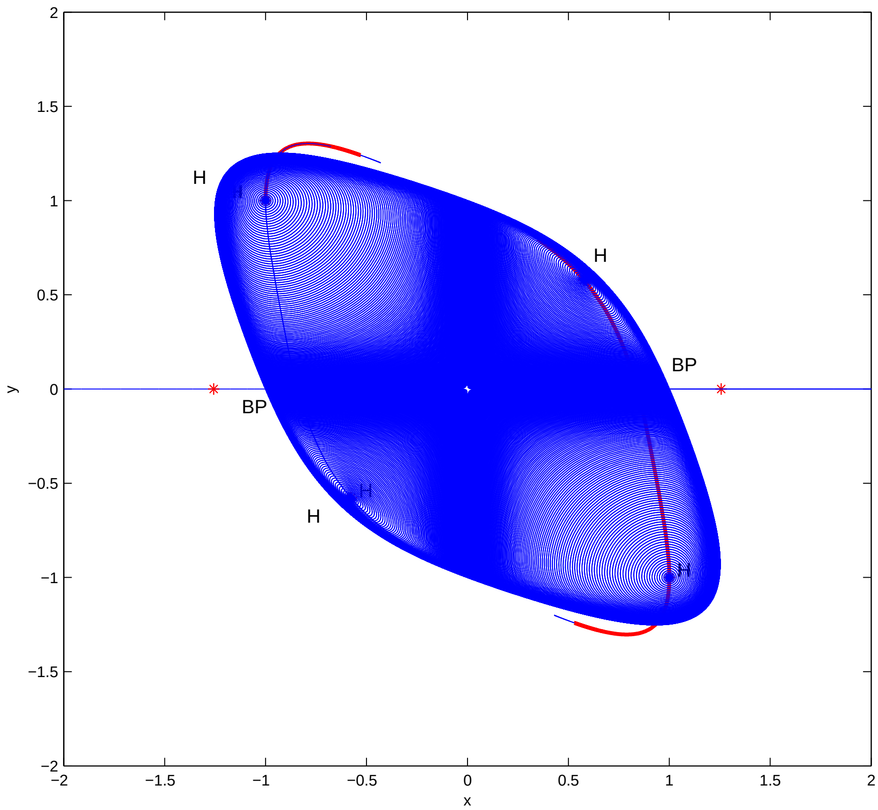

Fig. 1. Family of limit cycles of the system (2) when A is varied

The bifurcation analysis when A is varied is given in Figure 1. In this special case, two supercritical Hopf bifurcation points, A_1 and A_2, and two subcritical Hopf bifurcation points, A_3 and A_4, are observed. All of the limit cycles lie between the coordinate axes and the curve in one of quadrants. They also form a double throw-and-catch mechanism around a pitchfork bifurcation point in the middle.

3 Conclusion

In this work, a special case of the quintic generalization of the LV model has been studied. The model is globally Lyapunov unstable, however local stability indicates several instances of Hopf bifurcation to a family of bounded orbits.

It is also numerically observed that there is a discontinuous family of stable cycles in the same way as in the cubic nonlinear intersection.

References

1.A. Lotka. *Elements of Physical Biology*, 1st edition, Williams and Wilkins Company, Baltimore, 1925.
2.Y. Nutku. Hamiltonian structure of the Lotka-Volterra equation. *Phys. Lett. A*, 145: 27-28, 1990.
3.I. Kusbeyzi, O. O. Aybar, and A. Hacinliyan. Stability and bifurcation in two species predotor-prey models. *Nonlinear Anal. RWA*, 12: 377-387, 2011.
4.F. Dumortier, J. Llibre and J. C. Artés. *Qualitative theory of planar differential systems*, Spring, Berlin, 2006.
5.E. González-Olivares and A. Rojas-Palma. Multiple limit cycles in a Gause Type Predator-Prey Model with Holling Type III Functional Response and Allee Effect on Prey. *Bull. Math. Biol*, 73: 1378-1397, 2011.
6.J. Giné and V. G. Romanovski. Integrability conditions for Lotka-Volterra planar complex quintic systems. *Nonlinear Anal. RWA*, 11: 21002105, 2010.